

DESIGN AND DEVELOPMENT OF A VACUUM DEHUMIDIFICATION TEST
FACILITY

A Thesis

by

FRANCESCO NIMA SCHAFF

Submitted to the Office of Graduate and Professional Studies of
Texas A&M University
in partial fulfillment of the requirements for the degree of

MASTER OF SCIENCE

Chair of Committee,	Michael Pate
Co-Chair of Committee,	David Claridge
Committee Members,	Wolfgang Bangerth
Head of Department,	Andreas Polycarpou

August 2014

Major Subject: Mechanical Engineering

Copyright 2014 Francesco Schaff

ABSTRACT

A test facility was designed and constructed with the capability of isolating critical variables for controlling the novel membrane dehumidification-enabled cooling system's operation parameters as well as for acquiring preliminary membrane and cooling system performance measurements. The completed test facility consisted of two systems: 1) the feed-air system, which simulated the inlet-air conditions and performed the feed-air dehumidification and sensible cooling and 2) the vacuum system, which enabled the feed-air dehumidification by evacuating the membrane permeate side. The feed-air system as constructed was able to supply membrane-inlet flow rates up to 10 scfm over a range of temperature and relative humidity conditions, including 90°F and 90%RH, which was specified by the project sponsor. In addition, the feed-air system components included a membrane module installation site for dehumidification as well as a sensible cooling system to cool the membrane-outlet air to the 55°F and 50%RH conditions again specified by the sponsor. Measurement stations were placed at the membrane-inlet, membrane-outlet, and the sensible cooler outlet to measure the temperature and relative humidity at these critical locations. The vacuum system as built used a Pfeiffer DUO 10 Vacuum Pump with a 7 cfm pumping capacity, which was preceded by a 60 plate heat exchanger with an effective area of 2.05m² and an Oerlikon-Leybold WA 250 roots blower. The air leakage in the vacuum system was calculated to be less than 1% of the theoretical air permeation through the membrane module. Finally, the apparatus was constructed with the capability of measuring the power consumption of the equipment used for the dehumidification and sensible cooling process.

The functionality of the test facility was demonstrated through preliminary testing of the membrane module and the operation of the complete cooling system. The results suggested that the membrane material exhibited an increase in water vapor permeance from temperatures of 70 to 100°F, with calculated permeance values ranging from $3.93 \cdot 10^{-6}$ to $5.88 \cdot 10^{-6}$ kmol/kPa-m²-s. In addition, the results indicated that the novel membrane dehumidification-enabled cooling system was capable of achieving the specified operating conditions at a feed-air flow rate of 0.16 scfm by using a membrane module area of 0.024m².

DEDICATION

To my family and friends

ACKNOWLEDGEMENTS

I would like to thank Dr. Michael Pate, Dr. David Claridge, and Dr. Wolfgang Bangerth for their continuous support and kindness throughout the thesis development process. In addition, I would like to emphasize my gratitude to Dr. Pate for creating a lab culture that has contributed to some of my fondest memories while studying at Texas A&M University; I am truly grateful to have been a part of the Riverside Energy Efficiency Laboratory (REEL) team that has developed under Dr. Pate's leadership.

I also would like to express my appreciation to all of the individuals at REEL that have supported me throughout this thesis development process; these individuals include Oleksandr Tanskyi, James Sweeney, Kathryn Wadle, Grant Wheeler, Jennifer Reese, Matt Daugherty, Joshua Kading, Peng "Solomon" Yin, Wongyu Choi, Antonio Gomez, Cameron Fawcett, Tiffany Hargett, Mikolaj Pate, Meinan Chen, Charles Romero, Stephen King, Kristin Vorderkunz, Daniel Fonseca, and Stephen Pham.

Finally, I would like to thank my parents for their love, support, and wisdom that have nourished both my academic career and my personal relationships over the course of my life.

NOMENCLATURE

Cfm	Cubic feet per minute
D	Diameter
e	Pipe Roughness
f	Friction Factor
g	Gravity
h_{fg}	Enthalpy of Vaporization
\bar{h}_L	Average Heat Transfer Coefficient along length L
i	Variable number
L	Length
m	Slope of Change in Absolute Humidity over Relative Humidity
M_{air}	Molar Mass of Air
\dot{M}_{air}	Mass Flow Rate of Air Mixture
MBAR	Millibar
$\dot{M}_{water\ vapor}$	Mass Flow Rate of Water Vapor
n	Total number of variables
$\dot{N}_{wv,inlet}$	Molecular Water Vapor Flow Rate at the Inlet
$\dot{N}_{wv,outlet}$	Molecular Water Vapor Flow Rate at the Outlet
$\dot{N}_{wv,x}$	Water Vapor Mass Flow Rate at Location X
Re	Reynolds Number
Scfm	Cubic feet per minute at standard atmospheric conditions

T_s	Surface Temperature
T_{sat}	Saturation Temperature
V	Velocity
\dot{V}_x	Volumetric Flow Rate at Location X
w. c.	Water Column
X_i	Variable of number i
k_l	Thermal conductivity of liquid
μ_l	Dynamic viscosity of liquid
ρ	Density
ρ_x	Density at Location X
ρ_l	Density of liquid
ρ_v	Density of vapor
δ	Uncertainty
δ_{total}	Total Uncertainty
δ_{bias}	Bias Uncertainty
$\delta_{\text{random cal}}$	Random Uncertainty of Calibrated Values
$\delta_{\text{random meas}}$	Random Uncertainty of Measured Values
$\delta_{\text{human+temperature}}$	Uncertainty due to Human Error and Temperature Uncertainty
δR	Total Uncertainty in Equation R
δT_{sensor}	Absolute Uncertainty for the Temperature Measurement
$\delta \dot{V}_{\text{sensor}}$	Absolute Uncertainty for the Volumetric Flow Rate Measurement

δP_{atm}	Absolute Uncertainty for the Atmospheric Pressure Measurement
δX_i	Uncertainty of Variable X_i
$\delta \phi_{\text{sensor}}$	Absolute Uncertainty for the Relative Humidity Measurement
ϕ_{cal}	Calibrated Relative Humidity
$\phi_{\text{meas,avg}}$	Average Measured Relative Humidity
σ	Standard Deviation
ω	Absolute Humidity Ratio
ω_x	Humidity Ratio at Location X
ΔP_{pipe}	Pressure Drop Across a Pipe
$\Delta \omega$	Change in Absolute Humidity Ratio
$\Delta \phi$	Change in Relative Humidity
$\frac{\partial R}{\partial X_i}$	Partial Differentiation of R with Respect to Variable X_i

TABLE OF CONTENTS

	Page
ABSTRACT	ii
DEDICATION	iv
ACKNOWLEDGEMENTS	v
NOMENCLATURE	vi
TABLE OF CONTENTS	ix
LIST OF FIGURES	xiii
LIST OF TABLES	xvi
1. INTRODUCTION	1
1.1 Dehumidification Techniques	1
1.2 Membrane Module Commercial System	2
1.3 Membrane Operation	3
1.3.1 Membrane Operation	4
1.3.2 Membrane Permeation	5
1.3.3 Water Vapor Permeance	5
1.3.4 Separation Factor	6
1.4 Test Apparatus Design Goals	7
2. LITERATURE REVIEW	10
2.1 Previous Membrane Vacuum-Dehumidification Technologies	10
2.1.1 Liquid-Membrane Dehumidification System	10
2.1.2 Vacuum Sweep Dehumidification	20
2.2 Water Vapor in Vacuum Systems	21
3. FEED-AIR SYSTEM DESIGN	23
3.1 Feed-Air System Overview	23
3.2 Membrane-Inlet Air Treatment	23
3.2.1 Humidifier	24
3.2.2 Air Heater	25
3.2.3 Flow Control	25
3.3 Membrane-Outlet Air Conditioning	26

3.4	Membrane Dehumidification Measurements and Calculations	27
3.5	Humidity Sensor Selection and Calibration	29
3.5.1	Calibration Test Procedure	30
3.5.2	Uncertainty Analysis	31
3.5.3	Results	32
3.5.4	Conclusions	35
3.6	Tube Selection.....	35
3.7	Heat Transfer and Insulation	37
3.8	Measurement Stations	38
3.8.1	Measurement Locations	38
3.8.2	Power Consumption	39
3.8.3	Data Acquisition Hardware	39
3.9	System Variable Controls.....	40
3.9.1	Variable Frequency Drive	40
3.9.2	Digital Controllers.....	40
3.9.3	Variable Voltage Output	41
3.10	Complete Feed-Air System	41
3.11	Feed-Air System Summary	44
4.	VACUUM SYSTEM THEORY AND DESIGN	46
4.1	Vacuum System Overview	46
4.2	Design Parameters	48
4.3	Vacuum Flow Theory and Tube Sizing	50
4.3.1	Flow Regimes	50
4.3.2	Flow Restriction Analysis	52
4.3.3	Tubing Selection.....	55
4.4	Vacuum Pump Selection	57
4.4.1	Operation Considerations	57
4.4.2	Preliminary Vacuum Pump Tests	59
4.4.3	Vacuum Pump Selection	59
4.5	Intermediate Compressor Selection	61
4.5.1	Intermediate Compressor Overview	61
4.5.2	Detailed Compressor Descriptions	63
4.5.3	Comparative Testing	66
4.5.4	Intermediate Compressor Selection.....	70
4.5.5	Preliminary Roots Blower Test	71
4.6	Condenser Selection	73
4.6.1	Heat Exchanger Evaluation	74
4.6.2	Preliminary Condenser Evaluation	79
4.6.3	Condenser Selection	80
4.7	Vacuum Rejection Measurement Subsystem	81
4.7.1	Air Permeation	81
4.7.2	Water Vapor Permeation	82

4.8 Measurement Stations and Fittings	82
4.8.1 Permeate Chamber	82
4.8.2 Fittings and Sealant	83
4.8.3 Vacuum System Insulation.....	84
4.8.4 Power Input Measurements	84
4.8.5 Temperature Measurement Considerations.....	85
4.8.6 Pressure Measurements	86
4.8.7 Data Acquisition and Sensors.....	87
4.9 System Variable Control Methods	87
4.9.1 Variable Frequency Drive	88
4.9.2 Valves	88
4.9.3 Condenser Chiller/Heater	89
4.10 Completed Vacuum System	89
4.11 Preliminary Vacuum System Tests	93
4.11.1 System Leakage Measurements	93
4.11.2 Membrane Module Simulation.....	96
4.12 Vacuum System Summary	99
5. COMPLETE SYSTEM TESTS	100
5.1 Complete Test Apparatus	100
5.2 Membrane Module Performance Characterization	103
5.2.1 Performance Test Conditions	103
5.2.2 Membrane Module Performance Results	105
5.3 Novel Membrane Dehumidification-Enabled Cooling System Test.....	111
6. CONCLUSIONS	114
REFERENCES	116
APPENDIX A	120
APPENDIX B	123
APPENDIX C	125
APPENDIX D	127
APPENDIX E.....	128
APPENDIX F	131
APPENDIX G	132
APPENDIX H	133

APPENDIX I.....	134
APPENDIX J.....	136
APPENDIX K.....	141
APPENDIX L.....	143
APPENDIX M.....	146

LIST OF FIGURES

	Page
Figure 1: Simplified Membrane Module Illustration	4
Figure 2: Liquid-Membrane Dehumidification System Diagram [5]	11
Figure 3: Membrane Dehumidification Assembly Diagram [5]	12
Figure 4: Dehumidification Results for the Liquid-Membrane [5]	13
Figure 5: Feed Air Flow Rate Effect on the Liquid-membrane Dehumidification [5]	14
Figure 6: Permeate Pressure Effect on the Liquid-membrane Dehumidification [5]	15
Figure 7: Permeability Comparison [5]	16
Figure 8: Liquid-Membrane Module Diagram [6]	17
Figure 9: Liquid-Membrane Module Test Apparatus [6]	17
Figure 10: Water Recovery for Sweep Air (Solid Line Indicates the Maximum Ideal Value, and Dashed Line is the Theoretical Model) [6]	18
Figure 11: Water Recovery for Inlet Relative Humidities (Solid Line Indicates the Maximum Ideal Value, and Dashed Line is the Theoretical Model) [6]	19
Figure 12: Vacuum Sweep Dehumidification Apparatus Diagram [7]	20
Figure 13: Dehumidification Performance for Various Sweep Gas Flow Rates [7]	21
Figure 14: Complete Feed-Air System	42
Figure 15: Simplified Vacuum System Diagram (Terminology and Component Depictions from Vacuum Technology Standards [15])	47
Figure 16: Vacuum Pump Operation Range [19]	62
Figure 17: Inlet Chamber Temperatures for Various Mass Flow Rates	67
Figure 18: Pump Exhaust Temperature	69
Figure 19: Water Saturation Curve Determined Using EES	74
Figure 20: Completed Vacuum System	90

Figure 21: System Schematic	101
Figure 22: Temperature and Humidity Test Conditions	104
Figure 23: Humidity Ratio Variation from Set Point	105
Figure 24: Water Vapor Permeance Relationship to Temperature	107
Figure 25: Water Vapor Permeance Relationship to Humidity Ratio.....	108
Figure 26: Water Vapor Permeance for Different Permeate Pressures.....	109
Figure 27: Water Vapor Permeation Rate for Given Temperatures.....	110
Figure 28: Separation Factors for Various Inlet Temperatures.....	111
Figure 29: Water Vapor Permeation Uncertainty EES Code	120
Figure 30: Water Vapor Permeation Uncertainty EES Values	121
Figure 31: Feed-Air Pipe Pressure Drop EES Code	125
Figure 32: Feed-Air Pipe Pressure Drop EES Results	126
Figure 33: WA 251 Roots Blower Characteristics [29]	127
Figure 34: Sensible and Latent Load Comparison Calculations EES Code	128
Figure 35: Sensible and Latent Load Comparison Calculations EES Results	129
Figure 36: Sensible and Latent Condenser Loads for Various Conditions	130
Figure 37: Condenser Load Calculations in EES.....	131
Figure 38: Condenser Areas for Various LMTDs.....	132
Figure 39: System Air Leakage Data and Calculations	134
Figure 40: Air Leakage Uncertainty Propagation	135
Figure 41: Water Vapor Permeance for Various Inlet Humidity Ratio	136
Figure 42: Water Vapor Permeance for Various Flow Rate	137
Figure 43: Water Vapor Permeance for Various Permeate Pressure	137
Figure 44: Water Vapor Permeance for Membrane Outlet Temperature.....	138

Figure 45: Water Vapor Permeance for Membrane Inlet Temperature	138
Figure 46: Temperature Gradients Effect on Water Vapor Permeance	139
Figure 47: Feed Air Temperature Drop Dependence on Room Air	140

LIST OF TABLES

	Page
Table 1: PNNL and ADMA Module Details	8
Table 2: Water Vapor Permeation Uncertainty	29
Table 3: Potassium Sulfate Calibration	33
Table 4: Magnesium Chloride Calibration	34
Table 5: Sodium Chloride Calibration	35
Table 6: Feed-Air Pipe Pressure Drop	37
Table 7: Complete Feed-Air System Variables	43
Table 8: Module Dehumidification Parameters	49
Table 9: Vacuum Terminology [15]	50
Table 10: Flow Regime Ranges [15]	51
Table 11: Pipe Diameter Comparison	55
Table 12: Intermediate Compressor Performance Comparison	62
Table 13: Intermediate Compressor Ultimate Pressure	68
Table 14: Roots Blower Power Consumption	72
Table 15: Vaporization Enthalpies for Various Condenser Conditions (EES)	75
Table 16: Water Stream Enthalpy of Vaporization	76
Table 17: Complete Vacuum System Variable Details	91
Table 18: System Leakage Compared to Module Air Permeation	93
Table 19: Condenser Cooling Capacity Test #1	98
Table 20: Condenser Cooling Capacity Test #2	98
Table 21: System Schematic Legend	102
Table 22: Testing Control Variables	103

Table 23: Tabulated Test Results	106
Table 24: ARPA-E Condition Test Results.....	112
Table 25: Power Consumption for Membrane System	112
Table 26: Water Vapor Permeation EES Results	122
Table 27: Potassium Sulfate Calibration.....	123
Table 28: Magnesium Chloride Calibration.....	123
Table 29: Sodium Chloride Calibration	124
Table 30: Calibration Temperatures Comparison	124
Table 31: EES Code Variable Information	129
Table 32: Measured Test Data Conditions	141
Table 33: EES Calculated Results.....	142
Table 34: Fuji Compressor (Fan) Power Consumption Details	146
Table 35: Intermediate Compressor Power Consumption Details	146

1. INTRODUCTION

The heating, ventilation, and air conditioning (HVAC) industry is a multi-billion dollar industry that addresses the building energy consumption needs of the world, which is responsible for about 40% of global energy consumption [1]. Dehumidification technologies are at the forefront of HVAC cooling efficiency improvements since they utilize chemical selectivity of water vapor rather than traditional condensation techniques. A recent development in dehumidification technology was made by Pacific Northwest National Laboratory (PNNL) regarding dehydration membranes. The breakthrough involved making zeolite membrane films ($< 2 \mu\text{m}$) backed with a porous sheet substrate ($\sim 50 \mu\text{m}$), giving the combined membrane an estimated water vapor flux in warm, humid environments greater than any previous membrane module technology [2]. PNNL and ADMA Products then collaborated to combine layers of these membrane sheets into single modules for various air flow sizes. This paper discusses the development of a test apparatus for evaluating a novel membrane dehumidifier-enabled air cooling system, using the membrane modules designed by PNNL and ADMA Products.

1.1 Dehumidification Techniques

Conventional dehumidification systems remove water vapor from the air by cooling the mixture enough to cause the water vapor to condense out. Removing the water vapor in this manner is very energy-intensive because it not only requires removing the thermal energy, referred to as sensible cooling, to cool the water-air

mixture to the water vapor's saturation temperature, but it also requires the removal of chemical energy, referred to as latent cooling, to condense the water vapor until the equilibrium water vapor saturation pressure is reached. Often times, the latent cooling loads can account for a majority of the cooling demands, since the chemical energy removal required for water condensation is over $2000 \frac{\text{kJ}}{\text{kg}}$ and the thermal energy removal required to cool the gas mixture is approximately $1 \frac{\text{kJ}}{\text{kg}\cdot\text{K}}$ [3].

The novel membrane dehumidifier-enabled air cooling system aims to replace the conventional dehumidification systems with a more efficient alternative. This is accomplished by using a membrane to selectively and efficiently separate the water vapor from the air, thus reducing the latent load requirements.

1.2 Membrane Module Commercial System

The novel membrane dehumidification-enabled cooling system operation can be categorized into two cooling stages: the latent cooling stage, which is performed using the novel membrane's water vapor selectivity, and the sensible cooling stage, which is implemented at the membrane outlet using conventional cooling techniques. According to the theoretical membrane cooling system characteristics provided, the humid air should enter the membrane module and be isothermally dehumidified to a point which only sensible cooling is required to meet the target system outlet-air conditions.

The novel membrane dehumidifier-enabled air cooling system was designed to be capable of operating in dehumidification applications world-wide; however, the

cooling system performance variations under different climates were not established. In order to evaluate the performance in comparison with conventional cooling systems, a design operating condition for testing was determined.

The Advanced Research Projects Agency-Energy (ARPA-E) specified feed-air inlet and outlet operation conditions that the membrane cooling system was to be evaluated in for comparison to other cooling techniques. The cooling system inlet-air conditions were defined to be 90°F and 90%RH, and the cooling system target outlet conditions were specified to be 55°F and 50% RH; this corresponds to membrane module inlet conditions of 90°F and 90%RH and outlet conditions of 90°F and 15%RH. Ultimately, the cooling system meeting these target conditions would perform 80 kJ of cooling for every kg of air that passes through the membrane module.

1.3 Membrane Operation

The membrane technology developed by PNNL is at the core of the novel membrane dehumidifier-enabled air cooling system's innovative solution for cooling. The membrane technology for the novel membrane dehumidifier-enabled cooling system has a water vapor selectivity that is dependent on the surrounding water vapor partial pressure. This results in the membrane's water vapor adsorption increasing with higher water vapor partial pressures, and decreasing as the water vapor partial pressure is reduced [2]. Therefore, the water vapor pressure gradient across the membrane module is the driving force for the water vapor transfer through the membrane.

1.3.1 Membrane Operation

Since water vapor transfers through the module in the direction of decreasing water vapor concentration, each membrane module is categorized into two sections: the high water vapor concentration side, termed the feed air side; and low water vapor concentration side, termed the permeate side. When the membrane module is operating in a dehumidification system, the outdoor air is passed through the feed side of the membrane module to be dehumidified, while the water vapor on the permeate side is evacuated using a series of vacuum pumps; however, water vapor is only removed from the feed side if the water vapor partial pressure is lower on the permeate side than the feed side. Figure 1 below provides a simplified illustration of the membrane module pressure and flow components.

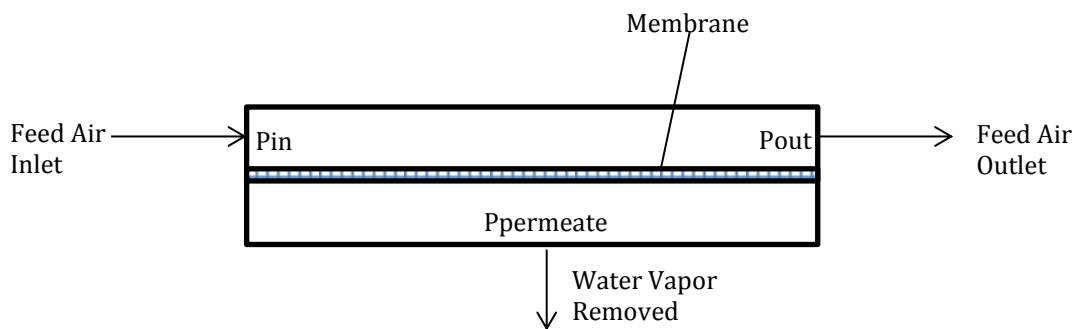


Figure 1: Simplified Membrane Module Illustration

The partial pressures of water vapor at the feed air inlet, feed air outlet, and permeate side are labeled in Figure 1 as P_{in} , P_{out} , and $P_{permeate}$, respectively. The amount

of water vapor removed from the feed air side was known to depend on P_{permeate} , P_{in} , P_{out} , and the feed air flow rate, though other dependencies were investigated in this project as well.

It is important to emphasize that the membrane dehumidification process is limited by the rate at which the permeate side can be evacuated; in addition, the energy consumption of the membrane dehumidification process is determined by the method of evacuating the permeate side. The design of the novel membrane dehumidification-enabled cooling system included a method of efficiently evacuating the permeate side and recovering the water.

1.3.2 Membrane Permeation

The term used to describe the molecular flow rate of a substance through the membrane module is permeation, usually quantified in kmol/s. Although the membrane modules provided by PNNL and ADMA Products were designed to only allow water vapor into the permeate side, some air was expected to pass through to the permeate side as well. The quantification of this air permeation was of interest for characterizing the membrane module selectivity as well as evaluating the implications that the air might have on the overall system effectiveness.

1.3.3 Water Vapor Permeance

An effective metric for evaluating and comparing the membrane module's performance is the water vapor permeance of the membrane module. The water vapor permeance is the inverse of the water vapor flow resistance through the membrane

module, analogous to conductivity in heat transfer. The equation used to calculate the water vapor permeance is shown below.

$$\text{Permeance}_{\text{water vapor}} = \frac{\dot{N}_{\text{water vapor}}}{A_{\text{membrane}}\Delta P} \quad (1)$$

where $\dot{N}_{\text{water vapor}}$ is the water vapor permeation rate through the membrane, A_{membrane} is the membrane area, and ΔP is taken to be the difference between the permeate water vapor pressure and the feed side water vapor pressure. Since the water vapor pressure varies along the feed side, the aforementioned ΔP is calculated by using the log mean pressure difference equation shown below.

$$\Delta P = \text{LMPD} = \frac{\Delta P_{\text{in}} - \Delta P_{\text{out}}}{\ln\left(\frac{\Delta P_{\text{in}}}{\Delta P_{\text{out}}}\right)} \quad (2)$$

where ΔP_{in} and ΔP_{out} are the water vapor pressure difference across the membrane at the feed side inlet and outlet, respectively. The purpose of using a log mean pressure difference, which is analogous to the log mean temperature difference used for heat exchangers, is to account for the decrease in pressure difference that occurs across the membrane module [4].

1.3.4 Separation Factor

The separation factor (SF) is a metric for comparing the air permeation through various membrane modules with respect to the feed and permeate side conditions. The separation factor is calculated by taking the molar ratio of water vapor to air on the permeate side and dividing it by the molar ratio of water vapor to air on the feed side, which is shown below [4].

$$SF = \frac{N_{w,p}/N_{a,p}}{N_{w,f}/N_{a,f}} \quad (3)$$

The molar mass of water vapor on the permeate and feed side are indicated by $N_{w,p}$ and $N_{w,f}$, respectively; whereas the molar mass of air on the permeate and feed side are indicated by $N_{a,p}$ and $N_{a,f}$, respectively. Original productions of the membrane module exhibited separation factors ranging in the hundreds; however, they are anticipated to have separation factors in the thousands after future design improvements.

1.4 Test Apparatus Design Goals

The purpose of this project was to design a test apparatus for evaluating critical performance variables for the novel membrane dehumidifier-enabled air cooling system, which could then potentially be used for characterizing the cooling system's performance under various operation conditions. This required developing a method of conditioning air to simulate the operating conditions that the cooling system might experience and constructing the cooling system design components required for the membrane dehumidification and sensible cooling, with the exception of the membrane module which was provided by PNNL. Since no prior novel membrane dehumidifier-enabled air cooling system apparatus had been developed for this membrane technology, much of the development of the test apparatus went into to implementing the cooling system operation designs for the membrane evacuation process.

The test apparatus was developed to evaluate the membrane cooling system for two different membrane module sizes and operating ranges; details of these membrane modules and operating ranges are shown in Table 1.

Table 1: PNNL and ADMA Module Details

MODULE NUMBER	EFFECTIVE MEMBRANE AREA	DESIGN FLOW RATE
#1	0.024 m ²	1 $\frac{\text{ft}^3}{\text{min}}$
#2	0.2592 m ²	10 $\frac{\text{ft}^3}{\text{min}}$

The design flow rates for each membrane module shown in Table 1 were determined by PNNL based on the assembled membrane module characteristics. Though these flow rates and membrane module areas are not sizes that would be used for a commercial cooling system, their sizes could be scaled up proportionally for use in commercial applications; thus these modules sizes were useful for evaluating the cooling system technology for future developments into larger systems.

The test apparatus developed for evaluating the membrane cooling system required two fundamentally different operating systems: the feed-air system, which was responsible for simulating the inlet-air conditions and performing the feed-air dehumidification and cooling; and the vacuum system, which was responsible for evacuating the permeate side of the membrane module to enable the feed-air

dehumidification. The development of these components of the test apparatus and preliminary test results are discussed in the subsequent chapters.

2. LITERATURE REVIEW

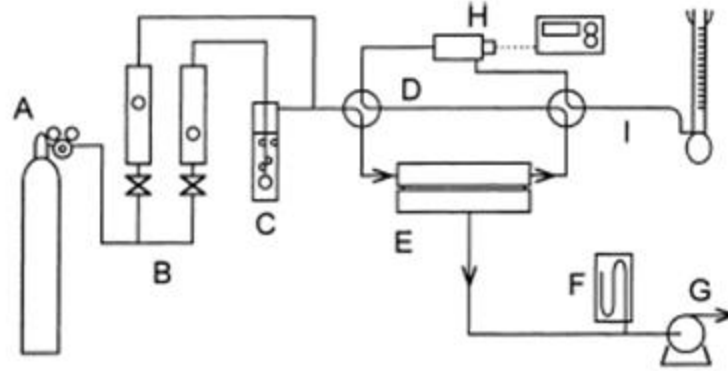
A literature review was conducted in order to investigate other membrane vacuum-dehumidification systems as well as the general interactions of water in vacuum systems. This literature was used to increase awareness of challenges that might be faced for given system designs as well as successful system implementations.

2.1 Previous Membrane Vacuum-Dehumidification Technologies

Although many membrane dehumidification systems exist, there are few systems that operate with the water vapor rejection side under a vacuum; this vacuum operation distinction was important to make when evaluating other membrane dehumidification systems, since factors such as air permeation and flow distribution can be significantly influenced by large air partial pressure differentials and vacuum flow regimes, respectively. Two previous vacuum dehumidification systems were evaluated based on their similarities in operating conditions to the novel membrane dehumidification-enabled cooling system considered for the test facility development.

2.1.1 Liquid-Membrane Dehumidification System

An experimental test apparatus was previously developed for evaluating a liquid-membrane dehumidification technology; a diagram illustrating this apparatus is shown in Figure 2 [5].



Experimental apparatus. A: air supply; B: flow controllers; C: water holder; D: four-way valve; E: membrane cell; F: manometer; G: vacuum pump; H: dew-point meter; I: bubble flow meter.

Figure 2: Liquid-Membrane Dehumidification System Diagram [5]

The liquid-membrane dehumidification system depicted in Figure 2 was capable of providing controlled air-flow rates and humidity ratios to the feed side of membrane fixture, which was evacuated on the permeate side to provide the water vapor partial pressure necessary for feed-air dehumidification [5]. This liquid-membrane technology performing the dehumidification was developed by applying a hygroscopic liquid to a hydrophilic membrane substrate, which had an 83% porosity; a diagram depicting this membrane structure is shown in Figure 3 below [5].

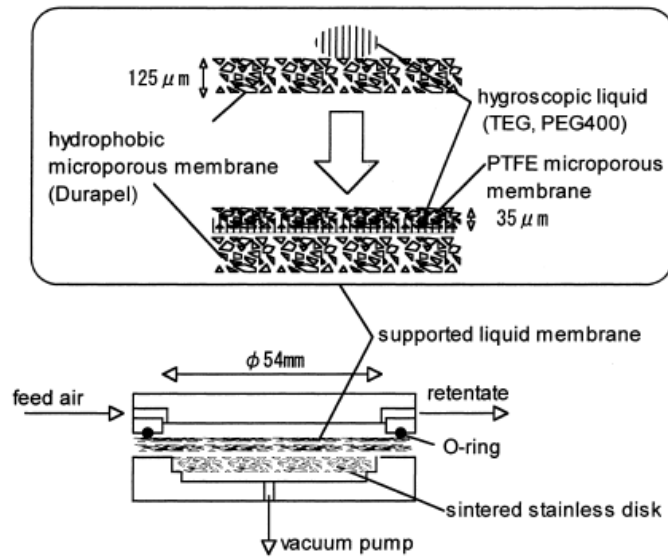


Figure 3: Membrane Dehumidification Assembly Diagram [5]

The performance of the membrane shown in Figure 3 was evaluated under several operating conditions; the variables modified during testing included the permeate pressure, inlet humidity ratio, and the feed air flow rate.

A test was conducted to evaluate the membrane-outlet relative humidity response for varying membrane-inlet relative humidity air supplies. In order to isolate the influence of the membrane-inlet relative humidity, the permeate pressure of the membrane was maintained at a constant 0.13kPa, and the feed air flow rate to the membrane was maintained between $97 \frac{\text{cm}^3}{\text{min}}$ to $105 \frac{\text{cm}^3}{\text{min}}$; the results from this test are illustrated in Figure 4 [5].

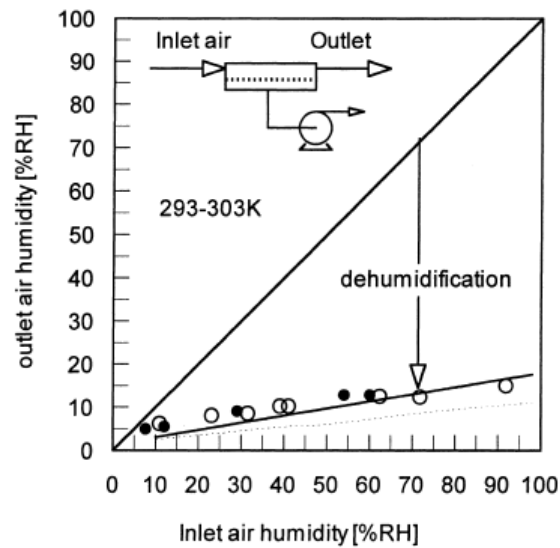


Figure 4: Dehumidification Results for the Liquid-Membrane [5]

The results for this test suggested that the water vapor permeation across the membrane fixture increased with a water vapor partial pressure differential increase. This behavior was reasonable since the permeation rate is theoretically proportional to the partial pressure differential for a constant permeability. Another dehumidification test was conducted by varying the feed air flow rate for a constant inlet relative humidity and permeate pressure [5]. The membrane-outlet relative humidity results for this test are shown in Figure 5.

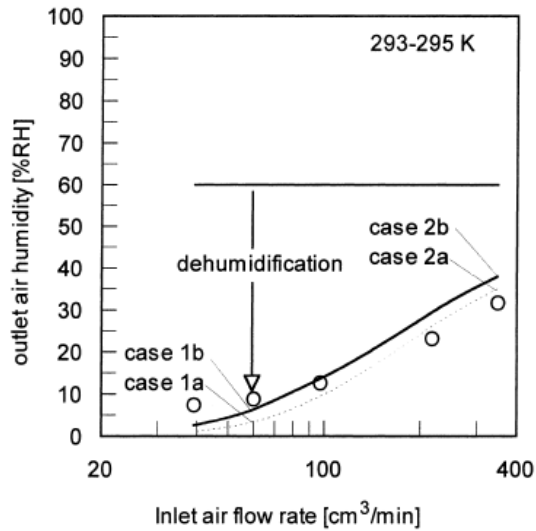


Figure 5: Feed Air Flow Rate Effect on the Liquid-membrane Dehumidification [5]

The results for the variable flow rate test suggested an increase in the membrane-outlet humidity ratio for increases in the feed air flow rate. A possible explanation for this relationship is that as the feed air flow rate is increased, the water vapor on the feed air side has less time to interact with the membrane; therefore, this is a result that would be expected to occur in the novel membrane dehumidification-enabled cooling system as well. The next dehumidification test performed involved evaluating the membrane-outlet relative humidity for various permeate pressures, while maintaining a constant membrane-inlet relative humidity and feed air flow rate; the results for this test are shown in Figure 6.

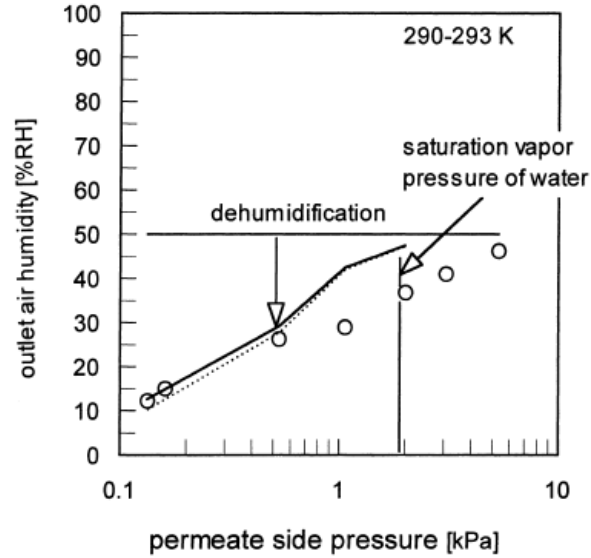


Figure 6: Permeate Pressure Effect on the Liquid-membrane Dehumidification [5]

The permeate pressure effect on the outlet humidity ratio was similar to the membrane-inlet relative humidity effect; the water vapor partial pressure differential across the membrane decreases as the permeate side pressure is increased, and this decrease in partial pressure causes a decrease in the water vapor permeation.

Finally, the permeabilities for both the air and water vapor were compared over the performance test conditions to compare the selectivity; the results for this comparison are shown in Figure 7.

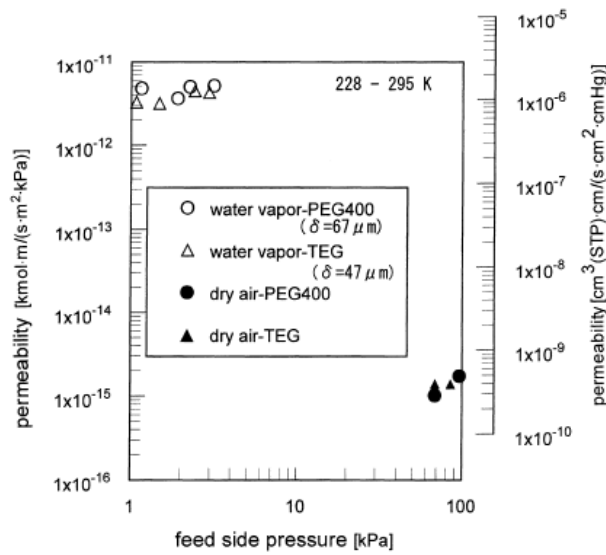


Figure 7: Permeability Comparison [5]

The water vapor permeability data in conjunction with the liquid-membrane composition suggested a water vapor permeance for the membrane that was in the range of 10^{-5} to $10^{-6} \frac{\text{kmol}}{\text{kPa}\cdot\text{m}^2\cdot\text{s}}$, which was comparable to the water vapor permeability of the zeolite membrane reported by PNNL. In addition, the permeability evaluation indicated a water vapor to air selectivity that was over 2000 [5].

The liquid-membrane dehumidification technology was then evaluated in a cooling system using a membrane module, which contained layers of membrane films; the membrane module packing method is illustrated in Figure 8 below [6].

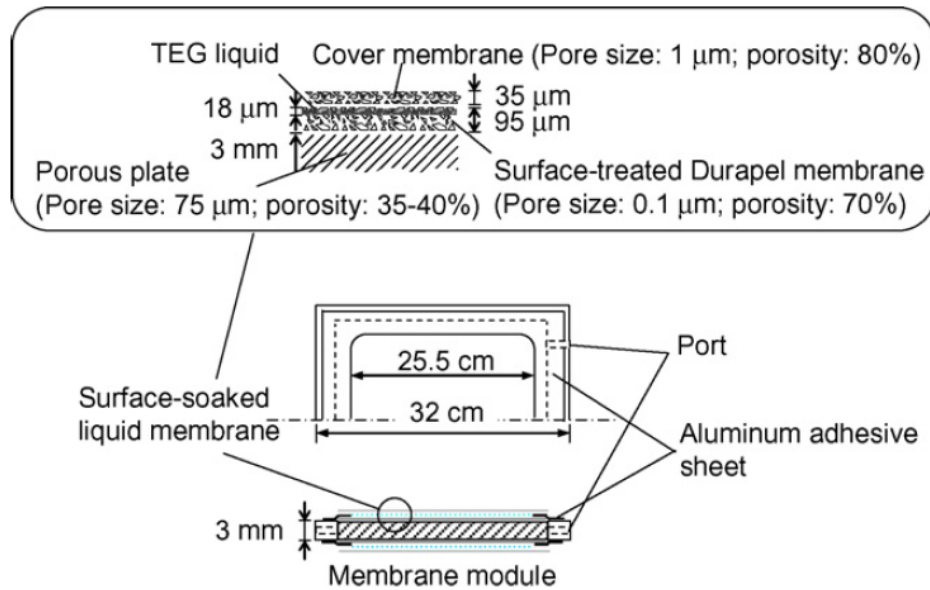


Figure 8: Liquid-Membrane Module Diagram [6]

The membrane module assembly was then evaluated in a cooling system test apparatus, which included a sweep air inlet device and a distinct water recovery method at the outlet of the vacuum pump; a diagram of the membrane module test apparatus is shown in Figure 9.

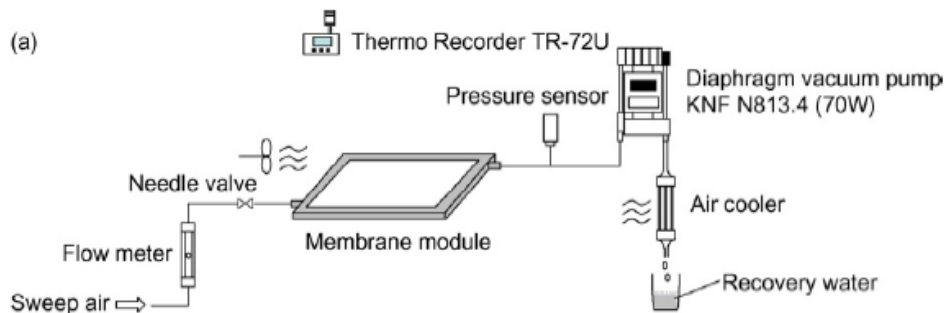


Figure 9: Liquid-Membrane Module Test Apparatus [6]

The membrane module was tested in the apparatus depicted in Figure 9 to determine the effects of sweep air and feed-air inlet relative humidity on the water recovery, which was measured using the collected condensed water from the vacuum pump exhaust. The results of the water recovery rates for various sweep air flow rates are shown in Figure 10 below.

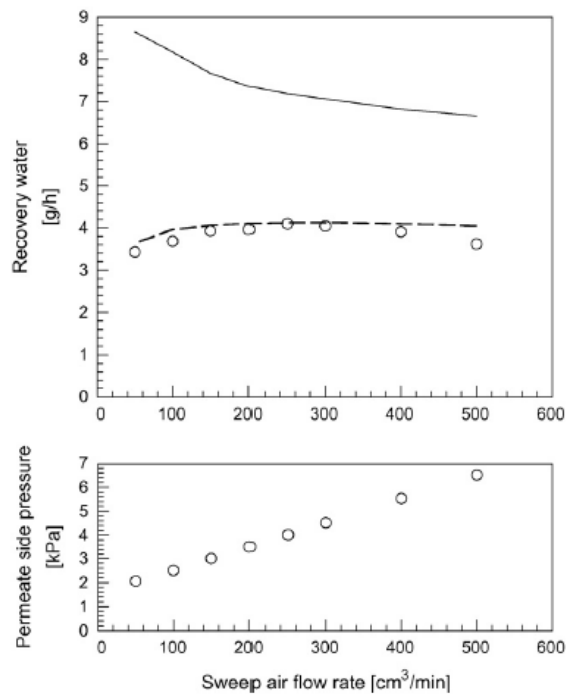


Figure 10: Water Recovery for Sweep Air (Solid Line Indicates the Maximum Ideal Value, and Dashed Line is the Theoretical Model) [6]

The results indicated a peak water recovery rate between sweep air flow rates of 200 and 300 $\frac{\text{cm}^3}{\text{min}}$. It is important to make a note that the vacuum pump exhaust was air-

cooled, and as a consequence any non-condensables in the sweep gas might have contained water vapor entrained. Therefore, this decrease in water recovery could be a function of the recovery method and not a function of the permeation rate. The results for the water recovery with respect to the feed-air inlet relative humidity are shown in Figure 11.

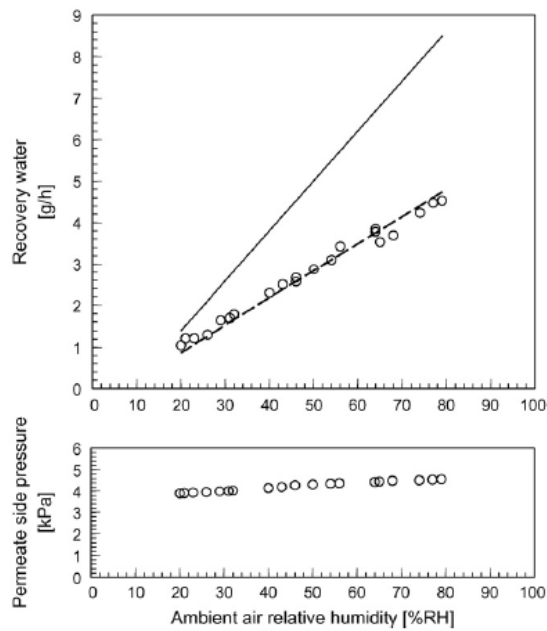


Figure 11: Water Recovery for Inlet Relative Humidities (Solid Line Indicates the Maximum Ideal Value, and Dashed Line is the Theoretical Model) [6]

The results shown in Figure 11 indicated an increase in water recovery for an increase in the membrane-inlet air relative humidity.

2.1.2 Vacuum Sweep Dehumidification

Another vacuum dehumidification system investigated used a vacuum sweep dehumidification test apparatus to evaluate the dehumidification performance of an [emim][BF₄] membrane material, which had permeance values similar to many polymer membrane materials [7]. The various components of the vacuum sweep dehumidification apparatus are shown in Figure 12.

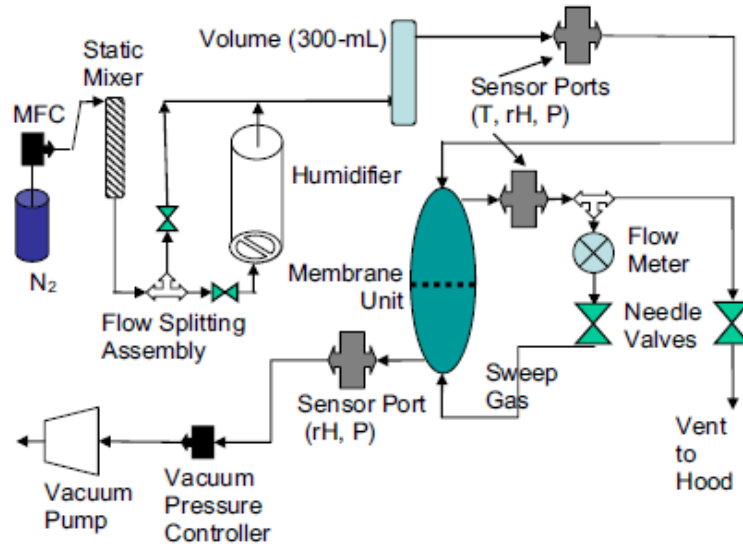


Figure 12: Vacuum Sweep Dehumidification Apparatus Diagram [7]

This vacuum sweep dehumidification process essentially consisted of a membrane which was dried out using a vacuum pump in combination with a sweep gas, which was supplied from the dehumidified feed-air flow stream. Some of the test results for varying permeate pressures and sweep rates under fixed inlet-air conditions, 31.4°C and 94%RH, are shown in Figure 13.

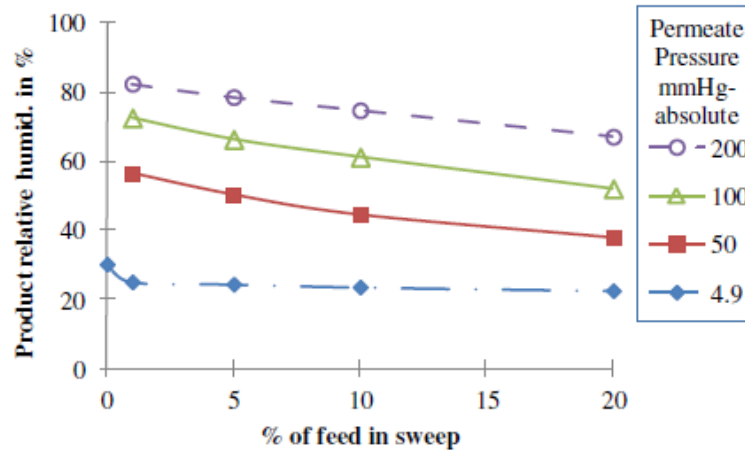


Figure 13: Dehumidification Performance for Various Sweep Gas Flow Rates [7]

The results in Figure 13 illustrate the impact of the sweep gas in removing water vapor from the permeate side of the membrane module. This sweep gas affect illustrates a hybrid performance for the vacuum system operation and ambient condition operations; as the sweep air increases, the system permeate flow approaches the continuity of an ambient condition.

In conclusion, these various vacuum dehumidification setups developed contained methods of evaluating operational dependencies, but analyses of temperature effects on the permeance properties were scarce.

2.2 Water Vapor in Vacuum Systems

An investigation was also performed to evaluate the response that water vapor might have on the vacuum apparatus operation for the applications specified by the

novel membrane dehumidification-enabled cooling system. The evacuation process for vacuum systems can be intricately dependent on the water vapor interactions with the system; for example, many internal surfaces and elastomer O-rings contain previously adsorbed or absorbed water that is released as the pressure is decreased in the system [8]. This effect can be observed by evacuating a vacuum system to its ultimate pressure, backfilling it with dry N₂ to atmospheric pressure, and then pumping it back down to its ultimate pressure range, which will usually occur faster than the initial pumpdown due to the lack of desorption load requirements imposed by water [9]. The aforementioned backfilling of the system with an inert gas is influential because it acts to fill the small voids that would otherwise allow water vapor diffusion; however, this influence is limited by the various materials' dispositions to permeate gases from the ambient environment to the vacuum system [8]. The effects of these various internal surface and elastomer O-rings on water vapor desorption and permeation rates was important to consider to determine if they could potentially influence the membrane module water vapor permeation. In fact, for typical vacuum systems the water vapor becomes the primary gas in the vacuum system at the 10⁻¹ pascal pressure range [8], and approximately 99% of the gas load in this low pressure range is due to the desorption of water [9]. A general range of water vapor outgassing ranges was reported to be from 10⁻⁷ $\frac{\text{mol}}{\text{m}^2\text{s}}$ to 10⁻¹¹ $\frac{\text{mol}}{\text{m}^2\text{s}}$ depending on characteristics such as the operating pressure [10]; however, in comparison to the 12 · 10⁻⁶ $\frac{\text{kmol}}{\text{kPa}\cdot\text{m}^2\cdot\text{s}}$ permeance of the membrane module, reported by PNNL, this outgassing effect was determined to be negligible.

3. FEED-AIR SYSTEM DESIGN

3.1 Feed-Air System Overview

The feed-air system can be categorized into three main sections: the membrane-inlet air treatment section, the membrane module dehumidification section, and the membrane-outlet air conditioning section. The membrane-inlet air treatment section components consist of flow, temperature, and humidity measurement and control devices necessary for simulating the membrane cooling system environmental operating conditions. The membrane module dehumidification section contains the membrane module and critical measurement devices necessary for evaluating the membrane module dehumidification performance. The membrane-outlet air conditioning section consists of a heat exchanger with measurement and control devices for reaching desired cooling system outlet conditions; it is important to note that the membrane-outlet air conditioning heat exchanger is a component that would be used in an implemented cooling system to perform sensible cooling, whereas the membrane-inlet air treatment components are entirely for simulating the cooling system's inlet-air operating conditions. In addition to the aforementioned sections, there were a variety of section interfaces and connections used to develop the complete system; the development of the complete feed-air system components is discussed in this chapter.

3.2 Membrane-Inlet Air Treatment

The inlet-air conditioning components consist of the flow control devices, the humidifier, and the air heater; the purpose of these components was to take indoor lab air

and modify it to achieve the desired air-inlet humidity ratio and dry bulb temperature for a target flow rate. These components were essential for simulating various global air conditions, and their development is discussed in more detail below.

3.2.1 Humidifier

The humidifier section was designed to be capable of humidifying air to achieve humidity ratios of $0.028 \frac{\text{kg}}{\text{kg}}$ from lab air humidity ratios at around $0.009 \frac{\text{kg}}{\text{kg}}$ for feed-air flow rates up to 10 standard cubic feet per minute (scfm). This was accomplished by passing the feed-air stream through small-pore, air diffusers that were submerged underwater inside a corrosion-resistant container. The diffusers, originally designed as air stones for aquariums, were used to separate the air into bubbles that then pass through several inches of temperature-controlled water; the diffusers were necessary because they increased the effective surface area for evaporation to occur. Inside the container, submerged in the water, were two flexible, 16 inch long immersion heater elements capable of providing 250W of heating each. The first heater was controlled by a Novus PID controller with a relay output connected to the heater and an RTD measuring the water temperature; the second heater was connected to a 120 V power supply and used as an assist heater for achieving power inputs beyond those permitted by the Novus controller on the first heater. The air temperature just above the water level in the humidifier was also measured using an RTD, and this temperature was assumed to be the feed-air, wet-bulb temperature. This assumption was verified by passing air through the humidifier at various flow rates and measuring the outlet relative humidity using several independent humidification measurement technologies; the most accurate

of these technologies, having an uncertainty of $\pm 3\%$ relative humidity, measured values of 98% relative humidity at the exit of the humidifier for the various flow rate and humidifier heat output conditions. Furthermore, the humidity sensor data recorded at the membrane module inlet was used to verify the wet-bulb temperature measurement prior to taking data for each test.

3.2.2 Air Heater

The air-heater component was designed to be capable of heating the saturated air leaving the humidifier to a desired dry-bulb temperature; therefore, it functioned entirely to provide sensible heating. This air-heater component consisted of a copper tube, having an internal diameter of 0.94 inches, coated with heat-flux paste and a 25 Watt strip heater fastened around the tube using electrical tape; the air-heater component was connected to the system tubing via hose clamps. The tube temperature was controlled using a Novus PID controller with a relay output connected to the heater and an RTD measuring the heater outlet temperature, which was measured at the membrane inlet. For flow rates less than 3 scfm, the response time of the RTD to the heater output temperature was slow enough to cause significant temperature overshoots; therefore, a variable voltage output device was connected to the Novus controller in order to reduce the maximum power input to the heater.

3.2.3 Flow Control

The air flow rate to the membrane module was supplied using a 1.10 HP Regenerative Blower manufactured by the Fuji Electric company. This compressor was capable of achieving a wide range of flow rates from 0 to 98 CFM, which was controlled

using a VFD with 0.1 Hz precision. Furthermore, the blower was capable of operating at system pressure drops up to 54.5 inches of water column (w.c.). In order to prevent contamination or abrasive particles from entering the feed-air system, a compact air-intake filter was installed at the inlet of the Fuji blower. The filter had a maximum flow rate tolerance of 35 scfm, and was reported to remove 99% of particles down to 2 microns.

The air flow rate into the feed-air system was measured using a FLR1203 turbine flow meter, which was capable of measuring up to 50 liters per minute (LPM) with an uncertainty of $\pm 3\%$ of full scale.

3.3 Membrane-Outlet Air Conditioning

A membrane cooling system operating under ARPA-E test conditions requires a mechanism to provide sensible cooling for the dehumidified air exiting the membrane module. The sensible cooling for this apparatus was performed by passing the feed air through a heat exchanger that was cooled using chilled water. The heat exchanger used was an in-house, 4-foot long shell-and-tube heat exchanger that had a 3-inch shell outer diameter. The chilled water was supplied to the heat exchanger using a diaphragm water pump that cycled water through a temperature-controlled reservoir, which was cooled by an in-house conventional refrigeration system. The water reservoir temperature was measured using a T-type thermocouple and controlled using a NOVUS PID controller, which had its relay output connected to the refrigeration system's power supply; the heat exchanger inlet and outlet water temperatures were also measured and recorded using T-

type thermocouples. The feed-air temperature and humidity were measured at the heat exchanger outlet using a thermocouple and humidity sensor, respectively, to ensure that only sensible cooling was occurring; the feed-air temperature and humidity at the inlet of the heat exchanger was measured at the membrane module exit using a RTD and humidity sensor, respectively.

3.4 Membrane Dehumidification Measurements and Calculations

The membrane module inlet and outlet condition measurements were critical to understanding the membrane module performance. In order to improve the accuracy of these readings, the membrane inlet-air conditions were measured immediately before the entrance to the membrane module, and the membrane outlet-air conditions were measured immediately after the exit of the membrane module. These measurements included air temperature and relative humidity, which were used to evaluate water vapor permeation and heat transfer interactions across the membrane module.

As aforementioned, the accuracy of the flow, temperature, and humidity measurements at the membrane module inlet and outlet were critical for determining important membrane operation characteristics, such as water vapor permeation. While accurate sensors for measuring temperature are relatively inexpensive, the prices for accurate flow meters and humidity sensors can be orders of magnitude larger; in addition, accurate humidity and flow meters can be highly susceptible to damage. Several sensors with moderate uncertainty ranges, $\pm 3\%$ of full scale, were investigated for use based on durability and cost. In order to determine the impact that these sensor

uncertainties might have on the overall uncertainty of the water vapor permeation, a preliminary uncertainty propagation calculation was performed.

The flow meter, temperature, and humidity measurements were all required for calculating the water vapor permeation rate. The propagation of the various measurement uncertainties on the water vapor permeation rate uncertainty was calculated in EES using the Kline and McClintock uncertainty propagation technique; the general Kline and McClintock uncertainty equation is shown below.

$$\delta R = \left[\left(\sum_{i=1}^n \frac{\partial R}{\partial X_i} \delta X_i \right)^2 \right]^{1/2} \quad (4)$$

where δR is the total uncertainty of variable R , δX is the uncertainty of variable X , $\frac{\partial R}{\partial X}$ is the partial derivative of variable R with respect to variable X , and the subscripts i and n indicate the range of variables that R is dependent on. The water vapor permeation uncertainty calculated in EES was performed using a permeation equation derived from the conservation of mass.

$$\dot{N}_{wv,permeation} = \dot{N}_{wv,inlet} - \dot{N}_{wv,outlet} \quad (5)$$

where the water vapor molecular flow rates at the inlet and outlet were defined by the following equation.

$$\dot{N}_{wv,x} = M_{air} \dot{V}_x \rho_x \omega_x \quad (6)$$

The calculations for the permeation uncertainty were performed using EES. The absolute uncertainty inputs for the individual sensor measurements are shown in Table 2.

Table 2: Water Vapor Permeation Uncertainty

δT_{sensor}	$\delta \phi_{sensor}$	$\delta \dot{V}_{sensor}$	δP_{atm}
0.3 C	3 %RH	0.053 CFM	1 kPa

More information regarding the equation inputs, sensor uncertainty inputs, and uncertainty results can be found in Appendix A. Ultimately, the calculation results indicated that for ARPA-E membrane module operating conditions, which were 90°F and 90%RH at the inlet and 90°F and 15%RH at the outlet, the total permeation uncertainty would be approximately 8% for a feed-air flow rate of 1scfm. The results also suggested that the total permeation uncertainty would increase as the inlet and outlet relative humidities converge, assuming isothermal dehumidification. The permeation uncertainty was also calculated for varying operating temperatures from 20°C to 32°C at constant relative humidity values; however, the effects of these temperature variations on the total water vapor permeation uncertainty were less than 1%.

3.5 Humidity Sensor Selection and Calibration

The feed-air system components were required to operate accurately over a range of extreme relative humidity conditions. This was important to consider because relative humidity conditions near saturation can pose the risk of condensation on the sensors, which in some cases can permanently damage the sensor or void the calibration. Therefore, in order to avoid any high-cost risks and ensure sensor reliability, inexpensive humidity sensor technologies were investigated. The sensor selected for operating in the feed-air system was the DS1923-F5 Hygrochron Temperature and Humidity Data

Logger purchased from www.ibuttonlink.com, which uses capacitive polymer relative humidity sensor technology. This sensor was chosen due to its accuracy and durability in condensation-sensitive environments. However, prior to installation in the feed-air system, the uncertainty of the sensor was calculated at several humidity ranges using salt calibration tests. The salt calibration tests require mixing a chemically pure salt and water to form a saturated salt solution; in a closed system each saturated salt solution creates its own unique and consistent relative humidity, which can be referenced from previously published data . The Hygrochron sensors were tested by being placed in these saturated salt solution environments, and the sensors' relative humidity measurements were recorded. The relative humidity values acquired during testing were then compared to the calibrated values for given salt solutions; these calibration values were found from www.omega.com, and are included in the results tables under *Calibrated Instrument*. More details regarding the testing procedure and uncertainty analysis are discussed below.

3.5.1 Calibration Test Procedure

The procedure used to calibrate the humidity sensors was the following:

1. Rinse out the test container with distilled water
2. Pour the appropriate amount of test salt into each test container
 - a. Potassium Sulfate
 - b. Magnesium Chloride
 - c. Sodium Chloride

3. Using a dropper, add the appropriate amount of water to ensure that the water is fully saturated
4. Place the humidity sensors on an elevated position inside the temperature-controlled test container to ensure that the humidity sensor does not touch the water
5. Seal the test container so that there is minimal interaction with the ambient environment
6. Place the test container in a storage area that is well insulated and maintained at room temperature
 - a. Approximately 22°C (See Appendix B for temperature details)
7. Leave the sensors long enough for them to reach steady state and then remove the humidity sensors to retrieve the logged data

3.5.2 Uncertainty Analysis

The humidity sensor total uncertainty calculations incorporated bias uncertainties and random uncertainties; the equation incorporating these factors is shown below.

$$\delta_{\text{total}} = \left[(\delta_{\text{bias}})^2 + (\delta_{\text{cal}})^2 + (\delta_{\text{random meas}})^2 + (\delta_{\text{human+temperature}})^2 \right]^{1/2} \quad (7)$$

The bias uncertainty (δ_{bias}) of the humidity sensor was calculated as the difference between the calibrated relative humidity value and measured relative humidity value.

$$\delta_{\text{bias}} = \phi_{\text{cal}} - \phi_{\text{meas,avg}} \quad (8)$$

The calibrated relative humidity values and error values were all referenced from the published data on www.omega.com; however, the average measured relative

humidity and random error values were calculated from the test results. In order to get the random error of the sensor to a confidence level greater than 99%, three standard deviations were used.

$$\delta_{\text{random meas}} = 3\sigma \quad (9)$$

The uncertainty of the temperature measurement ($\pm 0.5^\circ\text{C}$) was also incorporated into the total sensor uncertainty analysis. The dependence of relative humidity on temperature for the saturated salt solutions was calculated using linear interpolation of published data, which showed minimum variations in relative humidity over a wide range of temperatures. This dependence suggested that a temperature uncertainty of 0.5°C correlated to a maximum relative humidity uncertainty of $0.1\% \text{RH}$. Considering that the measurements were recorded digitally with negligible rounding error, the human error was assumed to be negligible. Therefore, the combined human and temperature error values were considered to have the least effect on the total sensor uncertainty.

$$\delta_{\text{human+temperature}} = \pm 0.1\% \text{RH} \quad (10)$$

It is important to note that the uncertainty analysis was only performed on data after the sensor readings had reached steady state conditions. For the purposes of this experiment, steady state was reached when the following conditions were met: the standard deviation of the data remained less than $1\% \text{RH}$ for a period of two hours, and the range of the relative humidity data set did not exceed $3\% \text{RH}$.

3.5.3 Results

Humidity calibration tests were performed for three DS1923-F5 Hygrochron Temperature and Humidity Data Loggers at three different relative humidity conditions;

in addition, a repeatability test was performed with one sensor for two of the relative humidity condition tests. The different humidity sensors are indicated by the latter units of their serial numbers and an assigned sensor number. In addition, prior to the first test, sensor B2E was dipped in water and removed immediately to monitor the effects of condensed water exposure. The results for the humidity calibration of three DS1923-F5 Hygrochron Temperature and Humidity Data Loggers for three different salt conditions are shown in Table 3 below, and additional information for these tests is provided in Appendix B.

Table 3: Potassium Sulfate Calibration

POTASSIUM SULFATE CALIBRATION	TEST #	MEASURED		CALIBRATED INSTRUMENT		APPROXIMATE SENSOR UNCERTAINTY (%RH)
		Average Relative Humidity [%]	Std. Dev.	Relative Humidity [%]	Uncertainty	
Sensor #1 DCC6	1	97.38	0.52	97.45	±0.49	1.64
	2	98.59	0.47	97.45	±0.49	1.88
Sensor #2 B2E	1	98.12	0.43	97.45	±0.49	1.53
Sensor #3 B7F9	1	98.48	0.48	97.45	±0.49	1.83

The potassium sulfate calibration test was performed to evaluate the accuracy of the sensor at high relative humidities, which would be occurring at the inlet of the membrane module. The results for the potassium sulfate test shown in Table 3 indicate a maximum uncertainty of approximately 2%, and the repeatability test performed with Sensor #1 verified the previously acquired uncertainty value. The next salt calibration

considered was the magnesium chloride calibration; the results for this calibration test are summarized in Table 4.

Table 4: Magnesium Chloride Calibration

MAGNESIUM CHLORIDE CALIBRATION	TEST #	MEASURED		CALIBRATED INSTRUMENT		APPROXIMATE SENSOR UNCERTAINTY (%RH)
		Average Relative Humidity [%]	Std. Dev.	Relative Humidity [%]	Uncertainty	
Sensor #1 DCC6	1	35.38	0.42	32.93	±0.17	2.80
	2	35.55	0.39	32.93	±0.17	2.91
Sensor #2 B2E	1	35.45	0.35	32.93	±0.17	2.77
Sensor #3 B7F9	1	35.35	0.36	32.93	±0.17	2.70

The magnesium chloride calibration test was performed to evaluate the accuracy of the sensor at low relative humidities, which would be occurring at the outlet of the membrane module. The data in Table 4 suggests that the total uncertainty of the sensor at this low relative humidity is approximately 3%RH; furthermore, the Sensor #1 repeatability test shows agreement with the previously acquired results. The next salt calibration considered was the sodium chloride calibration; the results for this calibration test are summarized in Table 5.

Table 5: Sodium Chloride Calibration

SODIUM CHLORIDE CALIBRATION	TEST #	MEASURED		CALIBRATED INSTRUMENT		APPROXIMATE SENSOR UNCERTAINTY (%RH)
		Average Relative Humidity [%]	Std. Dev.	Relative Humidity [%]	Uncertainty	
Sensor #1 DCC6	1	77.60	0.55	75.38	±0.13	2.80
Sensor #2 B2E	1	77.32	0.40	75.38	±0.13	2.33
Sensor #3 B7F9	1	77.42	0.37	75.38	±0.13	2.37

The sodium chloride calibration provided another useful relative humidity condition to evaluate the sensor accuracy. The results in this relative humidity range indicate an accuracy similar to those acquired in the magnesium chloride calibration tests, which indicate approximately 3%RH uncertainty.

3.5.4 Conclusions

The test results from these salt calibration tests suggests that the Hygrochron temperature and humidity data loggers exhibit consistent performance with relative humidity uncertainty values of approximately 3%RH at temperature ranges from 21°C to 23°C. In addition, the results from sensor B2E in comparison to the others provided evidence to suggest that the Hygrochron can tolerate brief exposure to condensed water and still operate within the aforementioned uncertainty limits.

3.6 Tube Selection

The tube selection was based on several factors including compatibility with various system components, tube transparency for condensation detection, the pressure

drop across the tube for various flows, and the tube maximum pressure and temperature tolerances. The tube material chosen was clear, PVC tubing with operating temperatures up to 165°F and operating pressures up to 20 psi. The PVC tube size was determined by performing several pressure drop calculations for available tube internal diameters ranging from 0.5 inches to 1.5 inches ; sizes above 1.5 inches were disregarded because they had a large bend radius and were more difficult to connect to certain components. The equation used to calculate the pressure drop across a circular pipe was the following [11].

$$\Delta P_{\text{pipe}} = f \frac{L}{D} \frac{\rho V^2}{2} \quad (11)$$

In order to calculate the friction factor for turbulent flow, the Swamee Jain equation [12] was used.

$$f = \frac{0.25}{\left[\log_{10} \left(\frac{e}{3.7D} + \frac{5.47}{Re^{0.9}} \right) \right]^2} \quad (12)$$

A pipe roughness of 0.0015 mm was used for this friction factor equation, since this value was at the upper bounds of the normal PVC roughness range [13]. The results for the pressure drop calculations performed using EES are shown in Table 6; more details regarding the equations used for the pressure drop calculation are shown in Appendix C.

Table 6: Feed-Air Pipe Pressure Drop

$D_{internal}[in]$	$\dot{V}_{feed}[CFM]$	$V_{pipe}[\frac{m}{s}]$	Re_{pipe}	$\frac{\Delta P}{L_{pipe}}[\frac{in_{H_2O}}{ft}]$
0.5	10	37.3	31284	6.20
1	10	9.3	15642	0.28
1.5	10	4.1	10428	0.03

A volumetric flow rate of 10 scfm was used for the pressure drop calculations because it was the worst-case flow rate scenario. The results shown in Table 6 indicate the strong dependence that the diameter has on the pressure drop for a constant flow rate; the 0.5 inch internal diameter (ID) tubing has a pressure drop of 6.2 inches of water column for every foot of tubing length, whereas the 1.5 inch ID tubing has a pressure drop of only 0.03 inches of water column for every foot of tubing length. Putting this in context of the feed-air Fuji blower pressure limits of 54.5 inches w.c. suggested that the 0.5 inch ID tubing would restrict the flow too much for 10 scfm operation. Furthermore, after considering the bend radius and various system component compatibilities, the 1 inch ID tubing proved to be the optimum tubing size.

3.7 Heat Transfer and Insulation

The feed-air system was designed to provide temperature measurements that could be used to determine potential membrane module performance dependencies on temperature. In order to minimize the feed-air system's heat transfer interactions with

the ambient lab air, insulation was applied throughout the system and compensation control methods were established. The membrane module was isolated from the ambient lab using a thermal blanket, and most of the tubing throughout the feed-air system was encased in ¾” thick, soft Buna-N/PVC rubber pipe insulation that has a K factor of 0.25 [14]; the sensible cooler was insulated using the same PVC rubber pipe insulation material, but in a larger size. The PID controllers were used for compensating heat losses and gains throughout the system as well. For example, at the membrane-inlet air treatment locations losses could be compensated for by increasing the heat input, and for the sensible cooler location gains could be compensated for by lowering the heat exchanger temperature, though this might increase the energy consumption of the already inefficient refrigeration system used.

3.8 Measurement Stations

3.8.1 Measurement Locations

Temperature and relative humidity measurements were made throughout the system to evaluate performance, with the more accurate sensors being placed at locations critical to understanding the membrane dehumidification characteristics. Therefore, Pt100 Class A RTDs purchased from Omega were used to measure the temperatures at the membrane inlet, membrane outlet, and throughout the membrane-inlet air treatment section. In-house, T- type thermocouples were used to measure the room temperature and the sensible cooler outlet temperature, and Hygrochron temperature and humidity

loggers were placed at the membrane inlet, membrane outlet, and sensible cooler outlet for measuring relative humidity.

3.8.2 Power Consumption

The power consumption was determined for all of the single-phase equipment and the three-phase equipment that would be implemented in a novel membrane dehumidification-enabled cooling system; it is important to emphasize that from a power consumption perspective the current equipment is not sized appropriately for operation in an efficient membrane cooling system, but the power consumption is still measured to provide preliminary system data.

The power consumption for the single-phase equipment, such as the water circulation pump and sensible cooler refrigeration system, was calculated using data recorded from Fluke measurement devices; the current was measured using a clamp-on Fluke 333 ammeter, and the voltage was measured using a Fluke 179 multimeter. In order to improve the accuracy of the current measurement, two current loops were included in the clamp-on ammeter.

The three-phase Fuji compressor power consumption was measured using a Fluke 39 power meter device with 3-phase measurement capabilities. The active, reactive, and total power consumption of the compressor for each power line was displayed, which was then converted into a total compressor power consumption.

3.8.3 Data Acquisition Hardware

The raw digital data was collected using National Instruments data acquisition hardware. A NI-9174, 4-slot chassis was purchased from National Instruments to stream

information from the various measurement modules to the LabVIEW computer software used for real-time measurements. The four chassis slots were occupied with the following modules for each of the various measurement systems: two NI-9217, 4-channel input modules for measuring the RTD readings; one NI-9213, 16-channel thermocouple module for measuring the temperatures at various locations using thermocouples; and one NI-9205 analog input module used to measure data from the flow meter.

3.9 System Variable Controls

3.9.1 Variable Frequency Drive

A Toshiba VF-S7 variable frequency drive (VFD) was installed on the FUJI compressor motor in order adjust the feed-air flow rate; the precision achievable with this VFD was 0.1 Hz.

3.9.2 Digital Controllers

Novus PID controllers were used throughout the system to provide a sophisticated method of temperature control. The Novus N480D PID controller used a 1.5 A relay output, which was sufficient for the load requirements of the various components it was installed on.

3.9.3 Variable Voltage Output

A variable voltage output device was used in conjunction with a PID controller to adjust the power input to the air heaters. This was useful for preventing a significant temperature overshoot during the controller startup for 1 scfm tests.

3.10 Complete Feed-Air System

The completed feed-air system was assembled after incorporating all of the prior research, calculations, and preliminary test data for each of the components. A diagram showing the completed feed-air system with a sample membrane module is provided in Figure 14; in addition, the details for the variables indicated in Figure 14 are included in Table 7.

The various components shown in Figure 14 were connected together using a variety of NPT fittings including barbed adapters and through-wall fittings. In order to prevent leakage at the various connections, all of the threads for these fittings were wrapped with polytetrafluoroethylene (PTFE) tape and all of the system tubing was fastened to the barbed fittings using hose clamps.

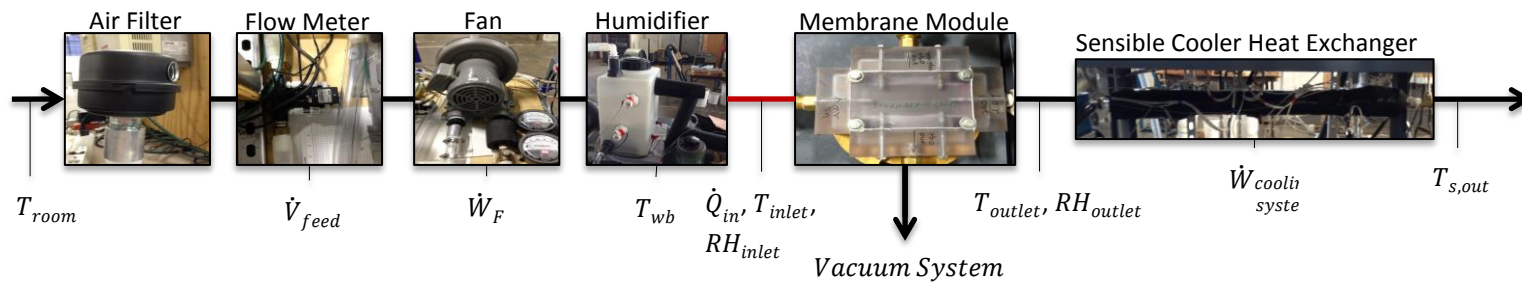


Figure 14: Complete Feed-Air System

Table 7: Complete Feed-Air System Variables

Symbol	Variable Name	Variable Details
\dot{W}_F	Fan Power Input	Current fan is oversized to handle humidification system flow restrictions
$\dot{W}_{cooling\ system}$	Sensible Cooling System Power Input	Consists of work input to the refrigeration system and water circulation pump
\dot{Q}_{in}	Air Supply Heat Input	A controlled heater is used to condition the dry bulb air temperature after exiting the humidifier at saturation
\dot{V}_{feed}	Feed Air Volumetric Flow Rate	The volumetric flow rate of the feed air going through the membrane module
RH_{inlet}	Relative Humidity of Inlet Air	The inlet relative humidity is measured using a data logger that is coupled with a temperature sensor
RH_{outlet}	Relative Humidity of Outlet Air	The outlet relative humidity is measured using a data logger that is coupled with a temperature sensor
T_{wb}	Wet Bulb Temperature	The temperature of the air immediately after it passes through the humidifier section, which is at saturation
T_{room}	Room Temperature	This measures the room temperature continuously
T_{inlet}	Inlet Air Temperature	This is an RTD measurement of the air going into the membrane module
T_{outlet}	Outlet Air Temperature	This is an RTD measurement of the air leaving the membrane module
$T_{s,out}$	Sensible Cooling Air Outlet Temperature	The temperature of air as it exits the sensible heat exchanger

A leak test across the various system components was performed prior to connecting the membrane module to the system. The leak test was performed by measuring the flow at both the inlet and outlet of the system, given a constant supply frequency to the Fuji compressor from the VFD; the difference between the two readings was then considered to be attributed to air leakage. This was a valid method for indicating air leakage, since a system with negligible air leakage would demonstrate the same system pressure drop and actual flow rate regardless of the location of the flow meter, assuming the power supply frequency is constant. Indeed, the results of these flow comparisons indicated that there were no differences in flow measurement outside the range of the flow meter uncertainty.

3.11 Feed-Air System Summary

The completed feed-air system was designed and developed with the capability of achieving the ARPA-E design operation conditions using the novel membrane dehumidification-enabled cooling system. The feed-air system constructed was able to produce high humidity and temperature inlet-air conditions, such as the 90°F and 90%RH conditions specified by ARPA-E, for feed air flow rates up to 10 scfm. In addition, the system was capable of measuring critical performance variables across the membrane module, and a cooling system was installed at the membrane outlet to perform the sensible cooling required to reach the 55°F and 50%RH conditions specified by ARPA-E. A preliminary uncertainty propagation analysis was performed to determine the water vapor permeation uncertainty for the various feed-air system sensor

uncertainties; the results indicated a water vapor permeation uncertainty of 8% for ARPA-E operating conditions at 1 scfm of feed-air flow.

4. VACUUM SYSTEM THEORY AND DESIGN

4.1 Vacuum System Overview

The vacuum system of the membrane module test apparatus was designed to simulate the vacuum components of a fully-functional membrane module cooling system under a variety of environmental conditions. Much research and testing went into the preliminary design of the vacuum components, since the vacuum equipment requirements for various environmental conditions were stringent. In addition, the total power consumption of the fully-functional cooling system was determined to be largely dependent on the vacuum equipment selection, based on simulations performed in a previous research project relating to this membrane module cooling system [4].

The vacuum system was designed around several critical components: the permeate chamber, the intermediate compressor, the condenser, and the vacuum pump. A simplified vacuum system diagram, using the *Fundamentals of Vacuum Technology* standard equipment illustrations, is shown in Figure 15.

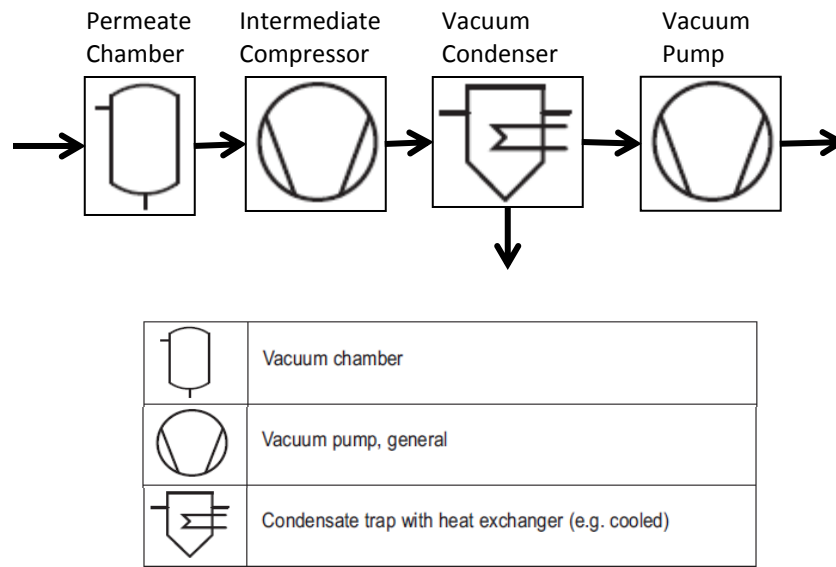


Figure 15: Simplified Vacuum System Diagram (Terminology and Component Depictions from Vacuum Technology Standards [15])

The membrane module permeation gases enter the vacuum system through the permeate chamber. Once inside the permeate chamber, the temperature and pressure of the fluid mixture are measured. Then the gas mixture travels to the intermediate compressor where it is compressed to its saturation pressure for a given vacuum condenser temperature. The condensed liquids travel down a condenser pipe to a liquid pump that discharges the fluid to atmosphere, while a vacuum pump rejects the remaining uncondensed vapors to ambient lab conditions. The purpose of this dual vacuum pump design was to reduce the energy consumption of the system by compressing the water in its liquid state rather than its gaseous state; this can be proven by evaluating the enthalpy difference between pressurizing an incompressible fluid, like

water, and pressurizing that same fluid in its vapor phase, which has a much larger specific volume.

The vacuum system developed in this project was designed to be capable of not only reaching the design system operating conditions, but also measuring critical performance characteristics such as the water vapor permeation and air permeation through the membrane module into the vacuum system. A special subsystem was developed just for recovering and measuring the outputs of the vacuum pump and water pump to calculate these permeation values, which is termed the Vacuum Rejection Measurement Subsystem. In addition, the vacuum system was designed to be capable of isolating variables for performing parametric tests to develop conclusions about the membrane module and system performance characteristics.

4.2 Design Parameters

The vacuum system was designed to maintain a constant permeate pressure and meet the flow requirements necessary for achieving the ARPA-E specified dehumidification test conditions, which were established as being some of the most demanding potential operating conditions for a complete membrane module cooling system. The ARPA-E specified membrane module conditions were to have inlet conditions of 90°F and 90%RH for 1 and 10 scfm of feed air flow; more details regarding the membrane dehumidification requirements for achieving the ARPA-E specified conditions are shown in Table 8.

Table 8: Module Dehumidification Parameters

LOCATION	T_{db} [F]	T_{wb} [F]	Φ [%]	ω [$\frac{kg_{water}}{kg_{air}}$]	$P_{watervapor}$ [kPa]
Membrane Inlet	90	87	90	0.028	4.3
Membrane Outlet	90	46	15	0.0046	0.74

Therefore, the test apparatus' tolerable vacuum flow rate was developed to be capable of removing all the water vapor from this feed air stream, as well as any permeated air through the membrane module. In addition, air and water vapor permeance data, provided by PNNL, was used to determine other potential operating conditions for the vacuum system. The values for the membrane's water vapor and air permeance were $12 \cdot 10^{-6} \frac{\text{kmol}}{\text{kPa}\cdot\text{m}^2\cdot\text{s}}$ and $6.4 \cdot 10^{-9} \frac{\text{kmol}}{\text{kPa}\cdot\text{m}^2\cdot\text{s}}$, respectively [4]; however, further membrane module testing performed at PNNL suggested the air permeance might be higher depending on testing conditions and module construction. After evaluating the potential high permeability scenarios, the maximum operating volumetric flow rate for the system was determined to be approximately 4% of the feed air flow rate; however, a safety factor was included for allowing additional system flexibility. In addition, the test apparatus' operable permeate pressure range was designed to be capable of dropping below 0.74 kPa (absolute pressure), which was the maximum allowable water vapor partial pressure for achieving the ARPA-E specified membrane outlet conditions.

4.3 Vacuum Flow Theory and Tube Sizing

4.3.1 Flow Regimes

The first task in selecting the vacuum system components was to investigate the molecular interactions and deviations from continuum theory that would need to be incorporated into the design. A vacuum system can operate in several conventionally defined pressure ranges, which are shown in Table 9.

Table 9: Vacuum Terminology [15]

VACUUM RANGE TERMINOLOGY	ABSOLUTE PRESSURE RANGE [MBAR]
Rough Vacuum (RV)	1000^{-1}
Medium Vacuum (MV)	$1-10^{-3}$
High Vacuum (HV)	$10^{-3}-10^{-7}$
Ultrahigh Vacuum (UHV)	$10^{-7}-10^{-14}$

Among these pressure ranges are several flow regimes that can occur in a vacuum pumpdown process: viscous flow, transition flow, and molecular flow [15]. The appropriate equations for evaluating the properties of the flow vary among these different flow regimes due to changes in molecular interactions. According to *Fundamentals of Vacuum Technology* [15], the flow regime conditions are described as the following:

- Viscous or Continuum flow: occurs when molecules' mean free path is much shorter than the diameter of the pipe ($\lambda \ll d$)
- Knudsen flow: this is the transitional flow range and occurs when molecules' mean free path is approximately equal to the diameter of the pipe ($\lambda \approx d$)
- Molecular flow: occurs when molecules' mean free path is much larger than the diameter of the pipe ($\lambda \gg d$)

In general, these flow regimes can be related to the aforementioned pressure ranges using the equations shown in Table 10 for air at 20°C:

Table 10: Flow Regime Ranges [15]

VACUUM RANGE	FLOW REGIME	DEFINING EQUATION
Rough Vacuum	Viscous	$p \cdot d > 6.0 \cdot 10^{-1} \text{mbar} \cdot \text{cm}$
Medium Vacuum	Knudsen	$6.0 \cdot 10^{-1} \text{mbar} \cdot \text{cm} < p \cdot d < 1.3 \cdot 10^{-2} \text{mbar} \cdot \text{cm}$
High and Ultrahigh Vacuum	Molecular	$p \cdot d < 1.3 \cdot 10^{-2} \text{mbar} \cdot \text{cm}$

where $p \cdot d$ is the product of the pressure times the pipe diameter. The significance of the operating flow regime is that at lower pressure ranges the molecular behavior becomes increasingly dependent on surface area interactions. For example, in molecular

flow there is a higher statistical probability of molecular interaction with the wall surface than with another molecule [15], which will affect the molecular flow rate into the evacuation device.

4.3.2 Flow Restriction Analysis

Several calculations were performed to determine the effects that flow restrictions and piping elements might have on the allowable flow rates in various flow regimes. The kinetic gas theory was used for parts of this analysis because it accounts for particle mean free path length changes with respect to their container size [15].

Fundamentals of Vacuum Technology describes a metric for evaluating vacuum flow rates supported by the kinetic gas theory that is expressed as the following.

$$q_{pV} = (p_1 - p_2) \cdot C \quad (13)$$

where q_{pV} is the flow rate in terms of $\frac{\text{mbar}\cdot\text{l}}{\text{s}}$, $p_1 - p_2$ is the pressure differential across the piping element or flow restriction, and C is the proportionality factor or conductance, which is primarily affected by geometrical properties [15]; the units for C and p are $\frac{\text{l}}{\text{s}}$ and mbar , respectively. The pressure and volumetric flow rate product can then be converted into a mass flow using the ideal gas law, as shown below.

$$\dot{m} = \frac{p\dot{V}}{R_{\text{specific}}T} = \frac{(p_1 - p_2) \cdot C}{R_{\text{specific}}T} \quad (14)$$

As shown in Equation 14, the mass flow rate through a given component is dependent on the pressure differential across the component and the conductance value of the component. *Fundamentals of Vacuum Technology* defines the conductance for laminar,

Knudsen, and, molecular flow through a straight pipe with a circular cross section of diameter d as the following.

$$C = 135 \cdot \frac{d^4}{l} \cdot \bar{p} + 12.1 \cdot \frac{d^3}{l} \cdot \frac{1 + 192 \cdot d \cdot \bar{p}}{1 + 237 \cdot d \cdot \bar{p}} \quad (15)$$

where d is in cm, l is in cm, and \bar{p} is the average pressure along the piping component in mbar. Equation 15 above can be simplified depending on the flow regime present. For example, in the viscous flow regime the first term is the dominating factor; therefore, the equation can be simplified to the following:

$$C = 135 \cdot \frac{d^4}{l} \cdot \bar{p} \quad (16)$$

However, in the molecular flow regime the pressures approach zero, and the dominating factor becomes the second term in the equation.

$$C = 12.1 \cdot \frac{d^3}{l} \cdot \frac{1 + 192 \cdot d \cdot \bar{p}}{1 + 237 \cdot d \cdot \bar{p}} \quad (17)$$

Once a conductance value is calculated, a conversion factor must be incorporated to account for vapors other than air; in the case of water vapor, the conversion factor is 1.263 [15].

The conductance equations aforementioned are considered in the context of a vacuum system, which usually contains various devices and connection components in series. Components in series that are contributing to the overall conductance of the system must be added in a manner similar to total resistance for resistors in parallel [15]; the equation for adding the conductance components is shown below.

$$\frac{1}{C_{\text{components}}} = \frac{1}{C_{\text{comp1}}} + \frac{1}{C_{\text{comp2}}} + \dots \quad (18)$$

These conductance values add together to create a total system conductance value that can then be incorporated into calculating the vacuum fluid flow rates for a given vacuum pump evacuation rate or known pressure differential. Since the pressure differential across a pipe is a measured physical property that varies for given pumping speeds, it is useful to calculate the vacuum fluid flow rate using the conductance in the context of a specific vacuum pump. The effect of various component conductances on the evacuation rate is a function of pumping speed, which is shown in the equation below [15].

$$\frac{1}{S_{\text{eff}}} = \frac{1}{S_{\text{pump}}} + \frac{1}{C_{\text{system}}} \quad (19)$$

where S_{pump} is the pumping speed of the vacuum pump in $\frac{1}{s}$, C_{system} is the total system conductance from all of its components prior to the vacuum pump, and S_{eff} is the effective pumping speed of the vacuum pump in $\frac{1}{s}$. It is evident from Equation 19 that as the conductance of the system increases, its influence on the effective pumping speed decreases; this is analogous to a decrease in electrical resistance allowing for an increase in electrical current flow, for a fixed voltage differential [15]. Finally, the vacuum fluid flow rate, or vacuum pump throughput, can be calculated using the equation below [15].

$$Q_{pV} = p_{\text{inlet}} \cdot S_{\text{eff}} \quad (20)$$

where p_{inlet} is the inlet pressure. The pressure and volumetric flow rate product can then be converted into a mass flow using the ideal gas law, as shown below.

$$\dot{m} = \frac{p\dot{V}}{R_{specific}T} = \frac{p_{inlet} \cdot S_{eff}}{R_{specific}T} \quad (21)$$

Once the mass flow rate is calculated, the conductance of the system can be optimized using different components to determine a vacuum system's design characteristics.

4.3.3 Tubing Selection

The primary purpose of the vacuum system tubing is to connect the various components of the vacuum system without inhibiting a vacuum pump's evacuation rate. A calculation was performed, using the aforementioned conductance and pumping speed equations, to determine the effects that various tubing diameter sizes would have on the vacuum flow rates. Table 11 shows the variations in the effective pumping speed for various tube diameters and pumping speeds at an average pressure of 0.5kPa.

Table 11: Pipe Diameter Comparison

D [IN]	L [FT]	\bar{P} [KPA]	C [L/S]	S_{pump} [L/S]	S_{eff} [L/S]	$\frac{S_{eff}}{S_{pump}}$ [%]
0.5	4	0.5	18.4	4.2	3.42	81
0.5	4	0.5	18.4	15	8.27	55
1	4	0.5	292.9	4.2	4.14	99
1	4	0.5	292.9	15	14.27	95
1.5	4	0.5	1480.2	4.2	4.19	100
1.5	4	0.5	1480.2	15	14.85	99

It is evident from Table 11 that the influence tubing size has on the effective pumping speed is affected by the pumping speed itself. As the pumping speed increases, the influence of the tubing size on the effective pumping speed increases for a fixed average pressure and tube length. A comparison of the three tubing sizes evaluated in Table 11 suggests that a tube with a length of 4 feet and an internal diameter of 1.5 inches has almost no effect on the vacuum pump for pumping speeds less than $15 \frac{1}{s}$, while a tube with the same length and an internal diameter of 0.5 inches can cause a 40% decrease in the pump throughput for pumping speeds of $15 \frac{1}{s}$. It is also important to note that a tube under the same operation constraints as the others, but with an internal diameter of 1 inch, seems to effect the pumping throughput by less than 6% for pumping speeds less than $15 \frac{1}{s}$.

The final tube selection was determined based on flow restriction, construction flexibility, operating ranges, and cost. Vacuum-rated, steel-reinforced, clear pvc tubing was selected because of its compatibility with the system operating pressures, its physical flexibility, and its usefulness for detecting undesired condensation. Furthermore, a 1 inch internal diameter was selected based on its increased flexibility compared to 1.5 inch diameter tubing, and the availability and cost of other 1 inch barbed fitting adapters that could be used to join the tubing to components of the system.

4.4 Vacuum Pump Selection

4.4.1 Operation Considerations

Two important vacuum pump operation parameters were its ultimate pressure and pumping speed, which can be often related. The vacuum pump was required to achieve ultimate pressures below 3kPa to allow for condenser pressure modifications. In addition, the vacuum pump was required to be capable of evacuating the maximum permeation of air and water vapor through the membrane module under extreme test conditions; this required a sufficient pumping speed at a lower inlet pressures. The pumping speed of each individual vacuum pump is affected by its inlet pressure, and this relationship is typically illustrated by a performance curve. The minimum allowable design flow rate for the vacuum pump was selected to be 0.5 scfm to account for worst-case water vapor and air permeation scenarios. When available, the pump curves were consulted for each potential vacuum pump to ensure that the pump's evacuation rate corresponded to the necessary flow rate. It is also important to add that priority was given to the pumps with larger flow rates, since the performance of the vacuum pump also influences the effectiveness of the intermediate compressor.

Contamination

Careful consideration was given to evaluating all of the potential contaminants that a given vacuum pump might introduce to both the vacuum system and the vacuum pump exhaust water recovery system. Some of the contaminants considered were oil particles, carbon particles, purge gases, ambient air, and even the potential of introducing water vapor if a liquid ring pump were used. The primary concern was to

reduce any contamination that might affect the vacuum-condenser or membrane performance characteristics, since the vacuum pump exhaust water recovery system contamination could be removed using conventional separation techniques. After investigating the membrane characteristics, it was determined that neither the oil particles nor the carbon particles would be able to reach concentrations large enough near the membrane surface to affect its performance, since this would require visible quantities of either contaminant to be significantly influential. Therefore, the only vacuum pump contaminants capable of traveling from the inlet of the pump to the vacuum-condenser in large enough concentrations to affect its performance were the water vapor from a liquid ring pump and purge gases or ambient air leakage. Air or purge gas leakage from ambient to the vacuum system above $1 \times 10^{-8} \frac{\text{kg}}{\text{s}}$ was considered an unacceptable form of contamination because it could influence the design operating conditions for the total condenser and permeate pressure, and it could affect the heat transfer rates within the condenser; water vapor contamination above $1 \times 10^{-6} \frac{\text{kg}}{\text{s}}$ was also considered unacceptable for these same reasons. In addition, air leakage or purge gas discharged out of the vacuum pump was considered undesirable contamination, because it could influence the flow measurements at the outlet of the vacuum pump.

Technologies Considered

Two categories of vacuum pumps were considered: dry and oil-sealed. The oil-sealed rotary vane pumps considered were able to operate within all of the performance constraints with the exception of contamination, and the dry pumps were able to offer contamination-free operation but had pressure and pumping speed limitations. The

vacuum pump options were then refined down to three choices: a dry diaphragm pump, a dry rotary vane pump, and an oil-sealed rotary vane pump. These different vacuum technologies were then tested before making a final selection.

4.4.2 Preliminary Vacuum Pump Tests

Several preliminary evacuation tests were performed using an in-house Robinair VacuMaster vacuum pump with a pumping speed of 4 scfm, a GAST dry rotary vane pump with a pumping speed of 5 scfm, and a GAST dry diaphragm pump with a pumping speed of 0.5 scfm. The purpose of this test was to compare technology performance characteristics that might not be readily available from the manufacturer or a distributor of the vacuum pumps; for example, the influence of pumping speed variations and air leakage on the evacuation rates over different pressure ranges were not readily available for some vacuum pumps. The preliminary test results suggested that at a 10 kPa inlet pressure the pumping speed of the Robinair pump far exceeded that of the other two pumps.

4.4.3 Vacuum Pump Selection

The vacuum pump selected for the system was a Pfeiffer DUO 10 Dual Stage Rotary Vane Vacuum Pump with a 7 cfm pumping capacity at inlet pressures ranging from 1 kPa to 10 kPa [16]. The main advantage of this pump over the other economical options considered was that its pumping speed was more than ten times the required speed; this pumping speed increase allowed for improved flexibility on the intermediate compressor selection, and the potential to meet the demands of potential future system flow rate increases. In addition, an investigation into the pump's operation

characteristics suggested a leak rate correlating to less than 0.1% of the minimum anticipated membrane permeation rate, which was important to consider for minimizing the pump's influence on the system measurements [17, 18]; the contribution of the vacuum pump leakage to the air permeation measurements was also later measured during system tests to ensure that the impact was negligible. The disadvantages of this pump technology were that traces of oil could potentially be exposed to some of the vacuum system components, oil could be potentially introduced into the vacuum pump exhaust water recovery system, and that condensed water in the vacuum pump oil reservoir could affect water recovery results and the lifetime of the pump; however, several precautions were taken to mitigate these issues. Firstly, an oil filter was applied to the vacuum pump outlet in order to separate the liquid mist from the water vapor and air. Secondly, routine maintenance checks were also performed to remove any condensed water trapped in the oil reservoir and replace contaminated oil. Finally, the vacuum pump's gas-ballast port was opened (normally closed) routinely after performing system tests to allow air to enter the pump, which helped to reduce water condensation inside the pump; the gas ballast port was normally closed during system testing in order to avoid any influence that the introduction of gases might have had on the air permeation measurements performed at the vacuum pump exhaust.

4.5 Intermediate Compressor Selection

4.5.1 Intermediate Compressor Overview

A critical component of the vacuum system design was the intermediate compressor selection. The intermediate compressor is burdened with strict operating constraints including withstanding abrasion and corrosion, preventing outflow contamination, providing the high volumetric flow rates required at low pressures, potentially operating with water condensation, and achieving the desired compression ratios. The intermediate compressor selection process was first started by determining a list of vacuum pumps that could operate in the vacuum range desired. An image from the Pfeiffer Vacuum company indicating typical vacuum ranges for various pumps is shown in Figure 16 [19]. Several of these vacuum devices were ruled out initially such as the liquid jet pumps, ejector pumps, and sublimation pumps due to their introduction of fluids and chemicals that might affect the recovery of water and contamination of the membrane. The remaining pumps were evaluated on several categories for consideration. Factors such as membrane and vacuum-condenser contamination, ultimate vacuum, volumetric flow rate, and power consumption were all incorporated into a table for comparing the various options. Table 12 displays some characteristics of the potential intermediate compressors from various companies.



Working Ranges of Vacuum Pumps

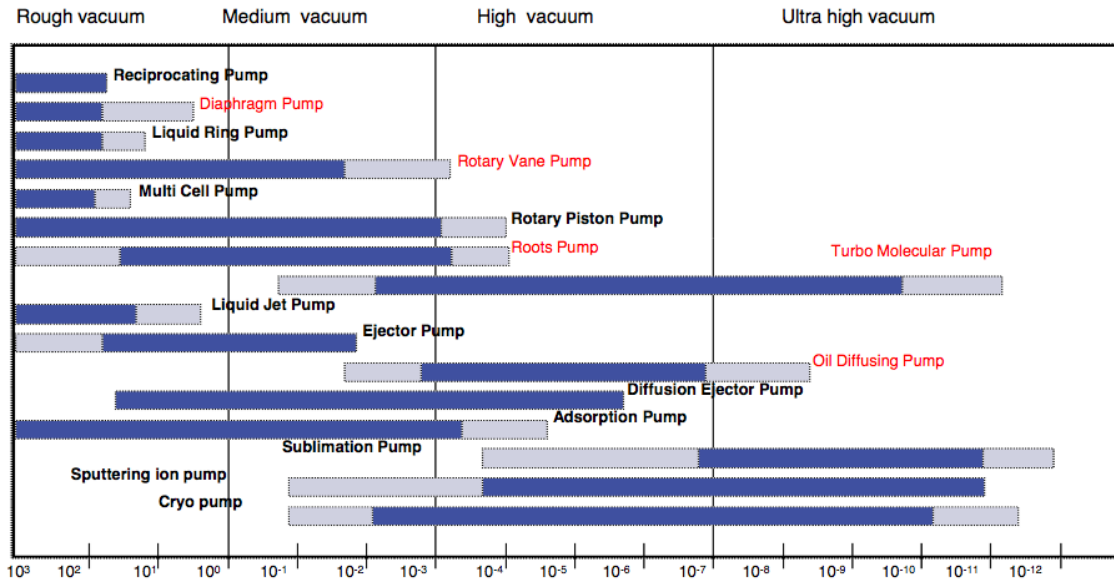


Figure 16: Vacuum Pump Operation Range [19]

Table 12: Intermediate Compressor Performance Comparison

MANUFACTURER	PUMP TYPE	FLOW RATE (CFM)	ULTIMATE VACUUM (KPA)	CONDENSATION TOLERANCE	POWER RATING (KW)	COST	CONTAMINATION TYPE
GAST	Dry Piston	6.25	5	Low	1.1	\$2,000	Teflon dust/Leakage
	Diaphragm	3.8	3	Low	0.39	\$600	None
	Dry Rotary Vane	21	6	High	1.1	\$840	Carbon Particles/Leakage
	Venturi Blowers	130	13	*Ignored b/c fluid input affects outlet pressure and contamination			
Pfeiffer	Rotary Vane Duo Line	65	< 0.1	1120 g/h	1.8	\$8,200	Carbon Particles/Mineral Oil
	Roots Blowers (1)	>100	< 0.1	Required Purge (N2)	0.74	\$9,000	Purge Gas *
Elmo-Rietschle	Liquid Ring	85	3	High	6.3	\$3,300	Water vapor
Edwards	Scroll	21	< 0.1	Low	0.53	\$13,000	Particulates/Leakage
	Screw	100	< 0.1	Required Purge (N2)	4.6	\$16,500	Purge Gas
Oerlikon-Leybold	Roots Blowers (2)*	>100	< 0.1	Purge Suggested	1.1	\$6,000	Purge Gas*

It is important to mention that Table 12 contains information inferred from the company websites and conversations with representatives; however, for accurate information the appropriate manufacturer or distributor should be consulted [18, 20].

4.5.2 Detailed Compressor Descriptions

The potential intermediate compressor pumps considered are provided below with details regarding their characteristics; these details are inferred from data on the Pfeiffer website and several phone conversations with vacuum pump specialists [18, 20].

Rotary Vane Pumps

Rotary vane pumps are typically oil sealed pumps that require a gas ballast to purging condensates for safe operation. While some dry rotary vane pumps do exist, they can be accompanied with issues such as air leakage through rotating shafts or relatively low flow capacities. Typically these vacuum pumps are used for reaching the rough vacuum range, with a typical single stage base pressure of 0.1 mbar [18, 19]; however, this base pressure is reduced by operating additional stages. These vacuum pumps can be used as fore pumps for assist blowers, but typically require a mist filter to prevent contamination. Rotary vane pumps have a relatively high water vapor tolerance; however, some pump designs can have carbon graphite vane wear due to water condensation, which in extreme cases can reduce the pump life down to weeks [18].

Diaphragm Pumps

Diaphragm pumps are dry positive displacement pumps that utilize a flexing elastomer to vary the pump's chamber volume. They typically are used for achieving the rough vacuum range and have base pressure of greater than 4mbar, though this can be

reduced by using a multistage pump [18, 19]. The pumping speeds for these are typically low, 1 to $10 \frac{\text{m}^3}{\text{hr}}$, since they rely on a flexing elastomer to displace the chamber fluids. In general, these types of pumps have low water vapor tolerance, because water vapor can condense and damage the elastomer [14]. In addition, they typically use check valves for separating the inlet and outlet chambers.

Rotary Piston Pumps

Dry rotary piston pumps are used to achieve rough vacuum and have a typical base pressure of 7 mbar [18, 19]. Their pumping speeds are relatively low, 8 to $16 \frac{\text{m}^3}{\text{hr}}$, and typically have low water vapor tolerance [18, 19].

Scroll Pumps (Oscillation Displacement Category)

Scroll pumps can come in dry or lubricated versions, and are used to reach base pressures of approximately 0.01 mbar [18, 19]. Their pumping speeds typically range from 8 to $16 \frac{\text{m}^3}{\text{hr}}$, and can release particles during normal wear [18, 19]. They also have low water vapor tolerance and short maintenance cycles.

Screw Pumps

Screw pumps are dry positive displacement vacuum pumps with high operating speeds, 100 to $600 \frac{\text{m}^3}{\text{hr}}$, and a typical base pressure of 0.1 mbar [18, 19]. These pumps have strict water vapor capacity tolerances, and are typically high cost pumps due to their tight machine tolerances.

Liquid Ring Pumps

The liquid ring pumps are positive displacement pumps that use circulating water as a rotor lubricator and seal. These types of pumps are typically able to operate in the 20-35 mbar pressure range, and have pumping speeds ranging from 30 to 40,000 $\frac{\text{m}^3}{\text{hr}}$ [18, 19]. Although these pumps can tolerate harsh environmental conditions, they can release water vapor into the evacuated system.

Roots Pumps

The roots blower is a dry positive displacement pump that is capable of handling high flow rates, ranging from 200 to 20,000 $\frac{\text{m}^3}{\text{hr}}$ at low pressures [18, 19]; however, the roots blower can only operate under strict vacuum pressure ranges, which requires it to have a backing pump. Since the roots blower operates at high speeds both the motor and rotary lobes are susceptible to overheating, depending on the operating conditions; therefore, the pump might require a cooling system. With regards to water vapor tolerance, the roots blower typically requires an N_2 purge to remove condensed liquids for long-term safety of the pump, and can be damaged by condensed water causing the rotary lobes to rust. Another issue with long-term use is the deterioration of the rotating shaft seals. Although the roots blower is a dry assist pump, there are shaft seals used to keep the gear lubrication separated from the vacuum chambers; these shaft seals can be worn out over time and require replacement.

4.5.3 Comparative Testing

A series of rudimentary tests were conducted to investigate the performance of several potential intermediate compressor technologies under various vacuum conditions; this was done to monitor and compare the effects that a given pumping technology might have on the vacuum system. Experimental testing was advantageous for evaluating these pump technology performances, because some pump technologies did not have well-documented fore-pump performance characteristics, such as vacuum pump exhaust conditions and pumping speed variations while operating under vacuum outlet conditions. The two compressor types tested were a 0.5 scfm diaphragm pump and a 5 scfm dry rotary vane pump, both from the GAST company. Although the flow rates and ultimate pressures for these pumps were not sufficient for use in the vacuum system of the test apparatus, they were an economical solution for evaluating the performance of their respective pump technologies.

The test apparatus consisted of two vacuum tanks with vacuum gauges, an intermediate compressor, two temperature sensors, and an oil-sealed positive displacement vacuum pump. Prior to testing, the inlet chamber was connected to the intermediate compressor inlet using brass compression fittings, and the outlet chamber was connected to the intermediate compressor outlet using the same brass fittings. The oil-sealed rotary vane pump was also connected to the outlet chamber using brass compression fittings and was used as the backing pump for the potential intermediate compressor evaluation.

Results

The first test conducted was for observing the thermal response of the inlet chamber during evacuation; this was considered useful for potentially discovering expansion cooling affects that might occur during testing. This test was conducted by evacuating the chamber at the inlet of the pump and measuring the temperature and pressure responses; the results of the measurements are illustrated in Figure 17.

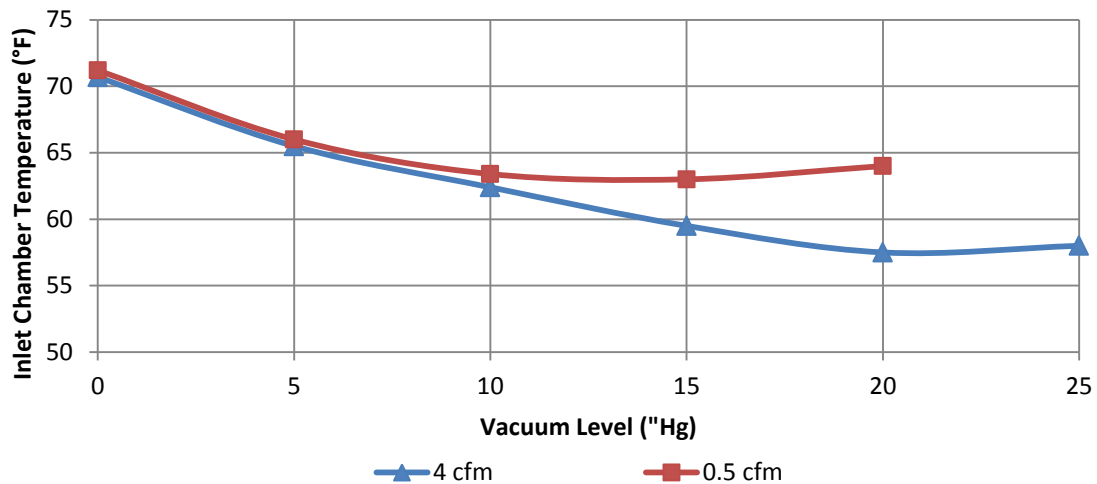


Figure 17: Inlet Chamber Temperatures for Various Mass Flow Rates

The results indicated a decrease in temperature during the evacuation process, which then started increasing with time as the system approached thermal equilibrium. The ultimate vacuum levels for the two dry vacuum pumps were measured next by evacuating the inlet chamber and monitoring the changes in ultimate pressure as the

outlet chamber pressure was reduced. The results for the ultimate vacuum level measurements with respect to the pump outlet vacuum levels are shown in Table 13.

Table 13: Intermediate Compressor Ultimate Pressure

OUTLET CHAMBER VACUUM, IN HG	ROTARY VANE	DIAPHRAGM
	Inlet Chamber Vacuum, In Hg	Inlet Chamber Vacuum, In Hg
0	27.5 ± 1.4	24 ± 1.4
10		25.5 ± 1.4
23	29 ± 1.4	
25		27 ± 1.4
28		28.5 ± 1.4

The results indicated that the ultimate vacuum achievable was a function of the pump's outlet pressure conditions, and that significant improvements in ultimate vacuum levels could be achieved with reductions in the outlet pressure. In addition, the ultimate vacuum pressures achieved with an atmospheric outlet chamber pressure showed agreement with GAST specifications for the ultimate vacuum pressure.

A study was performed to measure the exhaust temperature of the dry vacuum pumps over time; the results are shown in Figure 18.

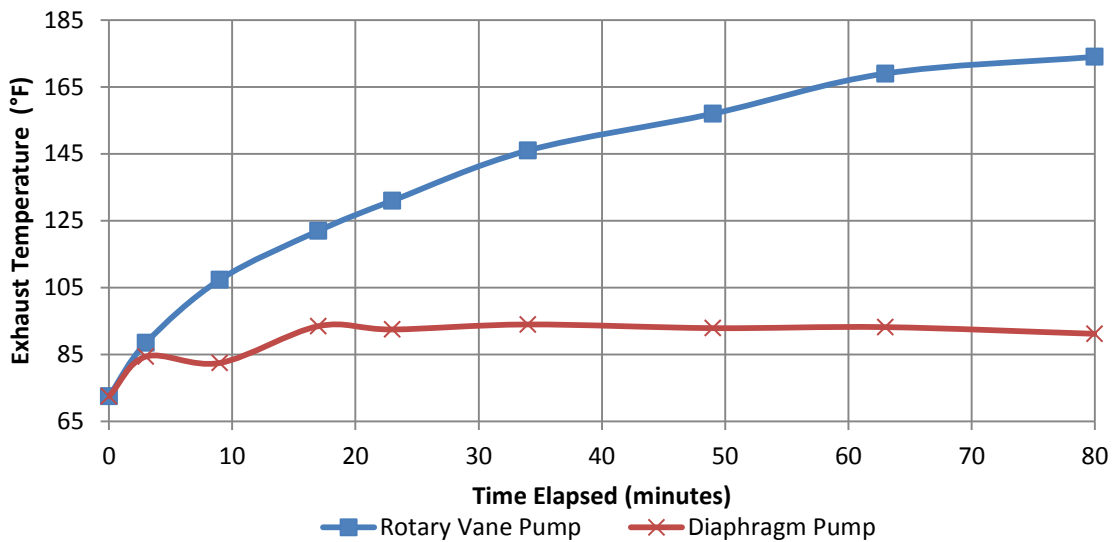


Figure 18: Pump Exhaust Temperature

The results shown in Figure 18 above indicate that the heat output of the rotary vane pumps is significantly greater than the heat output of the diaphragm pump. This discrepancy in heat outputs could be in part due to the difference in flow rates between the two pumps.

One important observation that was made during intermediate compressor testing was that the dry rotary vane pump was displaying indications of air leakage. After further investigation, it was discovered that air leakage through the shaft seal was a characteristic of the pump design.

Conclusions

The results of this experiment were used to make three generalizations regarding the intermediate compressor technology: the ultimate vacuum achievable for the

intermediate compressor is a function of the outlet pressure, the heat output of the intermediate compressor might require consideration for the condenser loads, and some dry rotary vane pumps can be susceptible to air leakage.

4.5.4 Intermediate Compressor Selection

The final choice for the intermediate compressor was chosen based on optimizing the parameters indicated in Table 12 with a high priority placed on efficiency, membrane and vacuum-condenser contamination prevention, operating pressure range, and flow rate capabilities. The cost and water vapor tolerance were given lower priority, since a solution to these issues was to buy an inexpensive pre-owned pump; therefore, any damage to the pump from operation would result in minimal losses. The intermediate compressor technology chosen was the Oerlikon-Leybold WA 251 roots blower; however, the pre-owned version purchased for the vacuum system was its predecessor model, the WA 250 roots blower. Since this pump was discontinued years back, information regarding the WA 250 model operation was limited, but further research suggested that the WA 251 specifications would be sufficient for understanding the operation characteristics of the WA 250 model. The technical specifications for the pump were primarily useful for determining the range of operating pressures and flow rates. As previously mentioned, roots blowers typically operates with a backing pump, and the roots blower's performance is influenced by the performance of the backing pump. The lowest backing pump speed indicated on the WA 251 specifications sheet was a 28 cfm, which corresponded to a roots blower speed of approximately 100 cfm, which is shown in Appendix D. This was useful for conceptualizing a proportional

dependence on the backing pump, but since the Pfeiffer backing pump selected had a lower flow rate the performance was ultimately evaluated through testing.

The primary risks for this blower were considered to be overheating the rotary lobes and damaging the motor; however, both of these issues were determined to be preventable by operating the pump in the correct pressure and temperature ranges. In order to provide additional protection to the roots blower, a circuit breaker was connected to the motor power supply line.

It is important to state that the WA 251 roots blower is oversized for the required conditions; however, any issues with oversizing become alleviated with an increased membrane module size. In addition, the roots blower is a dry vacuum pump, which can reduce the risk of membrane and condenser contamination. Although this intermediate compressor was chosen as the best solution for the aforementioned constraints, it still does not completely satisfy the desired efficiency requirement for the novel membrane dehumidification-enabled cooling system.

4.5.5 Preliminary Roots Blower Test

Once the roots blower was acquired a preliminary test was performed to evaluate its performance under a given simulated test operation with the Pfeiffer DUO 10 backing pump. In this test a constant flow was introduced to the vacuum system using a valve preceded by a rotameter, and the outlet pressure was maintained constant by adjusting the valves before the vacuum pump to control the flow rate leaving the system. The roots blowers' supply frequency was then adjusted, and the total power consumption was

recorded with a Wattson Console power measurement device (RS-485). The results for the roots blower test are shown in Table 14 below.

Table 14: Roots Blower Power Consumption

POWER CONSUMPTION {FLOW RATE OF 0.08 SCFM}				
Frequency [Hz]	Inlet Pressure [kPa]	Outlet Pressure [kPa]	Pressure Differential [kPa]	Power Consumption [kVA]
58	0.7	5	4.3	1.51875
50	0.9	5.2	4.3	1.07163
40	1	5.2	4.2	0.70227
30	1.4	5.2	3.8	0.29403
20	2	5	3	0.15552

One important observation was that as the frequency of the power supply was decreased below 30 Hz, the performance of the pump decreased drastically; this resulted in the pump no longer being able to maintain a pressure differential of greater than 3.8 kPa at the 0.08 cfm inlet conditions. In addition, the power consumption of the intermediate compressor showed a decrease in performance efficiency from 40Hz to 58Hz: the power consumption was reduced by 50%, while the pressure differential across the compressor remained within 10%.

4.6 Condenser Selection

The novel membrane dehumidification-enabled cooling system design specified an efficient method of rejecting water vapor from the permeate side of the membrane to atmosphere by compressing the water in its liquid state rather than in its gaseous state. This method involved condensing the water vapor at a low pressure and using a water pump to pressurize the liquid back to ambient conditions. The design also specified that the condenser temperature operate near the ambient wet-bulb temperature, since this can be achieved efficiently for a commercial system by using a cooling tower. The condenser design implemented in this apparatus incorporated these conceptual designs as well as design considerations acquired through testing and analysis.

The condenser was designed to ensure that the fluid mixture rejected from the intermediate compressor would reach the condenser design operating temperature, which was previously mentioned to be the wet bulb temperature of the simulated environmental inlet conditions for each test. The condenser pressure was also designed to be modifiable to optimize condensation parameters, which at the very least required the ability to increase the water vapor partial pressure in the condenser so that it exceeded the saturation pressure for the corresponding condenser temperature; the saturation curve for water vapor is shown in Figure 19 below.

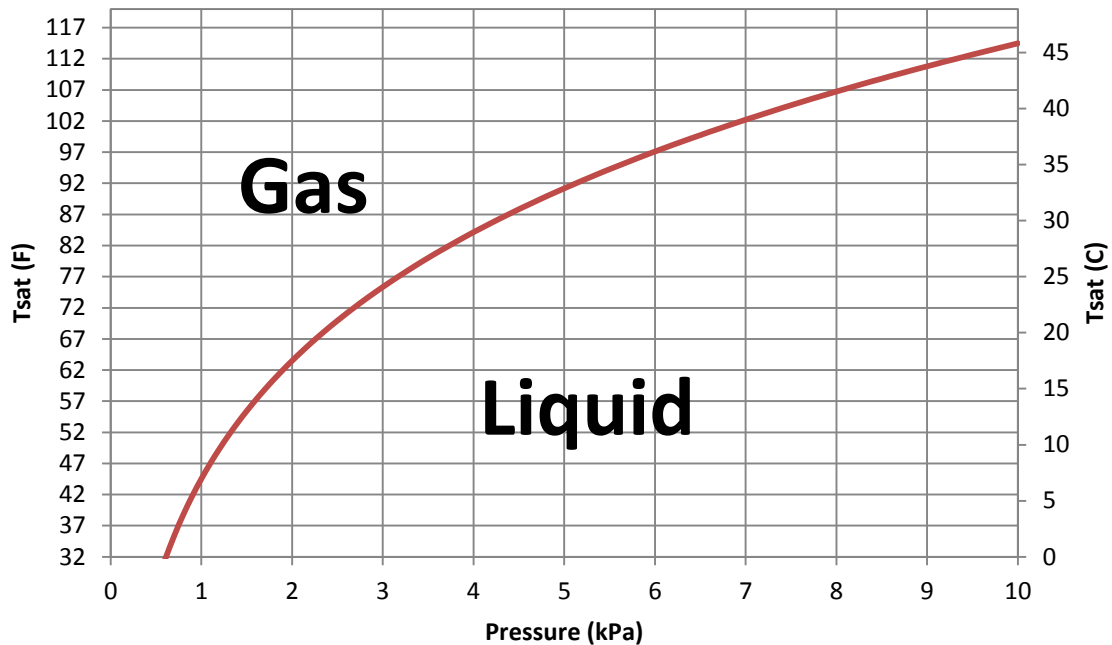


Figure 19: Water Saturation Curve Determined Using EES

It is important to emphasize the distinction between the total pressure and partial pressure when defining the condenser pressure. Since the partial pressure of water vapor is not measured directly, the total condenser pressure was set to a value that would account for the partial pressure of both the permeated water vapor and the permeated air. In addition, the condenser temperature and pressure were considered to be control variables for simulating various wet-bulb temperatures and for optimize overall system performance, respectively.

4.6.1 Heat Exchanger Evaluation

The critical condenser design characteristics were determined by performing heat transfer analyses and referencing published data on empirical condenser performance

results; this was then followed up by testing several viable condenser options to acquire more specific empirical data. The development of the vacuum condenser system is discussed below.

Condenser Sizing

One critical parameter of the heat exchanger used for condensation was the effective area for heat transfer. This effective heat transfer area for the condenser was determined by first evaluating the heat transfer load requirements for the condenser. These heat transfer loads were approximated by using several assumptions for simplification purposes: first, the heat transfer load for conditioning the air in the vacuum system was considered to be negligible since it was estimated to account for less than 1% of the vacuum fluid mixture; second, the sensible loads were neglected since they were estimated to account for less than 2% of the total heat transfer load (see Appendix E). This resulted in the heat transfer load being determined by the latent load requirements to condense the water vapor. The values for various vaporization enthalpies at different condenser conditions were determined using EES, and are shown in Table 15.

Table 15: Vaporization Enthalpies for Various Condenser Conditions (EES)

CONDENSER TEMPERATURE (°C)	SATURATION PRESSURE (kPa)	ENTHALPY OF VAPORIZATION ($\frac{kJ}{kg}$)
10	1.2	2477
15	1.7	2465
20	2.3	2453
25	3.2	2442
30	4.2	2430
35	5.6	2418

The condenser load requirements were then calculated using the worst-case scenario vaporization enthalpy, which was $2418 \frac{\text{kJ}}{\text{kg}}$, for the worst-case scenario water vapor mass flow rate; this calculation was performed in EES using Equation (18) below.

$$Q = m h_{fg} \quad (22)$$

where Q is the heat transfer rate, m is the water vapor mass flow rate through the condenser, and h_{fg} is the latent heat of vaporization. The results for the aforementioned condenser load calculations are shown in Table 16.

Table 16: Water Stream Enthalpy of Vaporization

HVAC SIZE (CFM)	\dot{m} (KG/S)	ENTHALPY OF VAPORIZATION AT 10KPA [KJ/KG]	Q_REQUIRE D (W)	Q_REQUIRE D (BTU/HR)
10	9.85E-05	2392	235.612	804.137

In order to translate the heat transfer load requirements into a required condenser area, additional heat transfer analysis was necessary. The heat transfer to the condenser vacuum fluids was evaluated using the following relationship [21].

$$Q = \bar{h}_L \cdot A \cdot (T_{\text{sat}} - T_s) \quad (23)$$

where \bar{h}_L is the average heat transfer coefficient across the plate of length L , A is the flat plate surface area, T_{sat} is the saturation temperature of the water vapor at the given

condenser pressure, and T_s is the condenser surface temperature. This heat transfer equation was rewritten to isolate the area component, as shown in the equation below.

$$A = \frac{Q}{\bar{h}_L(T_{\text{sat}} - T_s)} \quad (24)$$

Prior to solving for the condenser area, an analysis was performed to determine the average heat transfer coefficient. *Fundamentals of Heat and Mass Transfer* provides an equation for calculating the average heat transfer coefficient for laminar, condensing flow along a flat, vertical plate of length L [25], which is shown below.

$$\bar{h}_L = 0.943 \left[\frac{g\rho_l(\rho_l - \rho_v)k_l^3 h_{fg}}{\mu_l(T_{\text{sat}} - T_s)L} \right] \quad (25)$$

where g is the acceleration of gravity, ρ_l is the density of the condensed fluid, ρ_v is the density of the inlet vapor, k_l is the thermal conductivity of the condensed liquid, μ_l is the dynamic viscosity of the condensed fluid, and L is the length of the plate. Given a condenser pressure of 5kPa and a condenser temperature of 30°C, the average heat transfer coefficient was calculated to be approximately $1600 \frac{\text{W}}{\text{m}^2\text{K}}$, see Appendix F for more information. This heat transfer rate was compared with empirical data on average heat transfer rates for steam condensers operating under vacuum conditions. The heat transfer coefficients reported for vacuum, steam condensers ranged from $200 \frac{\text{W}}{\text{m}^2\text{K}}$ to $3400 \frac{\text{W}}{\text{m}^2\text{K}}$ [22, 23, 24]. Although heat transfer coefficients can vary for many reasons, including geometrical and flow regime differences, this empirical data was useful because it provided a range of practical condenser operation characteristics that showed agreement with the theoretical analysis. In order to avoid under-sizing the condenser, the

worst-case scenario heat transfer rate ($200 \frac{W}{m^2K}$) was selected for calculating the minimum condenser area. The complete set of values used to calculate the minimum condenser area, using Equation 24, is shown in Appendix G. The results for the condenser area calculation suggested a heat exchanger area of approximately 1.2 m^2 under worst-case log mean temperature difference conditions. This information was used to select one of several heat exchangers for preliminary testing to compare performance characteristics under actual operating conditions.

Condenser Temperature Control and Energy Balance

The condenser temperature was controlled using a Cole Parmer cooler/heater bath equipped with its own temperature monitoring and control system; this system was necessary to simulate the wet-bulb temperature conditions of a cooling tower operating at the feed-air inlet conditions. In addition, the condenser system was designed to provide measurement data for analyzing the heat transfer interactions between the vacuum side and the cooling fluid side. This was achieved by measuring the inlet and outlet temperatures of the condenser cooling fluid using RTDs, and measuring the cooling fluid flow rate using a rotameter calibrated for an operating range of 0.2-2gpm and an uncertainty of $\pm 5\%$ of full scale. These measurements were also useful for validating the Cole Parmer temperature output.

Condensed Water Storage

The condensed water rejected from the heat exchanger was designed to be separated from the vapors by using a condenser trap made in-house, which consisted primarily of a copper tee, a pipe bend, and a storage container. The copper tee was used

as a gravity trap to capture the condensed water exiting the vacuum condenser and lead it to a storage container, while the remaining vapor and mist traveled through a pipe bend up to the vacuum system exhaust. This pipe bend was included to capture any liquid mist that might have been entrained in the uncondensed vapor mixture, which after adhering to the tube surface could then drip down into the storage container. The container consisted of a clear pipe with graduated markings along the edge for calculating volumetric flow rate of the condensed water. Once the storage container was filled, a water pump separated by a valve was used to remove the contents. In order to prevent potential re-evaporation prior to emptying the storage container, the cooling water supply line was connected to the condenser storage area and encased in insulation.

4.6.2 Preliminary Condenser Evaluation

Several heat exchanger technologies were evaluated for their operation performance under vacuum using water vapor supply flow rates similar to those introduced by a membrane module experiencing 1 scfm feed-air operation conditions. A brief description of the various heat exchangers is discussed below.

Shell-and-Tube Heat Exchanger

The shell-and-tube heat exchanger purchased was designed for use in water-to-water cooling applications, and had a maximum heat transfer capacity of 70kW for water-to-water applications. The dimensions for the heat exchanger were the following: 4.8 inches in height, 10.375 inches in length, and 4.5 inches in width.

Flat Plate Heat Exchangers

Two flat plate heat exchangers were purchased and evaluated. The first heat exchanger was a B3-12A 40 plate heat exchanger from *dudadiesel.com*. This heat exchanger had an area of 0.48 m^2 , and a refrigeration capacity of 1-5kW. The second heat exchanger was a B3-36A 60 plate heat exchanger from *dudadiesel.com*. This heat exchanger had an area of 2.05 m^2 , and a refrigeration capacity of 4-15kW.

Performance Comparison

The difference in performance between the various heat exchangers was as expected. The 60 plate heat exchanger recovered the most water vapor for similar condenser operating conditions, but also had the largest condensed water storage before releasing the water to the intended storage container.

4.6.3 Condenser Selection

The 60 plate *dudadiesel* flat plate heat exchanger was selected for use as the vacuum condenser because of its ability to meet the required performance constraints and its compatibility with future system flow increases. Although the heat exchanger was oversized for the required conditions, the disadvantages of this oversized condenser were minimal; the disadvantages primarily consisted of a moderate increase in cost and a larger internal condenser storage which increased the time required to reach steady state.

Another factor that was accounted for in the condenser performance was fouling; over time, the condenser surfaces can accrue material that reduce its heat transfer coefficient, which is referred to as fouling. By selecting an oversized heat exchanger, the influence of fouling on achieving the operation performance requirements was mitigated.

4.7 Vacuum Rejection Measurement Subsystem

4.7.1 Air Permeation

The air permeation through the membrane module was designed to be measured at the exhaust of the vacuum system, since the anticipated quantities of air permeation would not be accurately detectable in the feed-air flow. However, there was a significant amount of uncertainty with regards to the amount of air permeation that might occur in the membrane module, since previous membrane modules had not been constructed and tested under the operating conditions that the novel membrane dehumidification-enabled cooling system demanded; therefore, the vacuum rejection measurement system was designed to be easily modifiable in order to accommodate different flow measurements.

Many flow meter technologies were investigated for this application; among those technologies considered were hot wire anemometers, turbine flow meters, coriolis flow meters, and differential pressure flow meters. Initially two flow meters were purchased based on cost, accuracy, and operating range with the intention of acquiring other flow meters in the future as more detailed air permeation data was acquired. One of the two flow meters selected was a turbine flow meter, FLR1006-D, capable of measuring air flow rates up to 5 L/min with an uncertainty of $\pm 3\%$ of full scale; the other flow meter was a turbine flow meter from the same manufacturer, FLR1002 model, capable of measuring flow rates in the range of 40mL/min to 200mL/min with an uncertainty of $\pm 3\%$ of full scale. More information on the flow meters selected is provided in Appendix H.

Preceding the flow meter were a condensate trap (ONF 25 S) and a flat plate heat exchanger, which was maintained at 55°F to condense water vapor entrained in the exhaust air. These two items were included to remove any oil mist or water particles that might affect the flow meter's accuracy. In addition, the influence of the complete vacuum system and vacuum pump leakage on the flow measurements was evaluated when considering the sensor measurement uncertainty.

4.7.2 Water Vapor Permeation

The water vapor permeation through the membrane module to the vacuum system was measured by recovering all of the condensed water exiting the vacuum system. There were two design locations for recovering water: the vacuum condenser storage container and the vacuum pump exhaust. In order to recover the moisture rejected from the vacuum pump exhaust an oil trap followed by a condenser were placed at the vacuum pump outlet. The condensed water recovered from the vacuum pump exhaust was then combined with the water from the vacuum condenser storage container and measured on a scale to measure the amount of water recovered.

4.8 Measurement Stations and Fittings

4.8.1 Permeate Chamber

The permeate chamber was designed to be a measurement station for monitoring critical membrane permeate-side properties, such as temperature and pressure; in addition, the chamber was designed to be compatible with various fittings that might be installed for future component modifications or membrane connection modifications.

The permeate-side vacuum conditions determined for proper membrane module performance required that there be no condensation in the permeate chamber. Therefore, a cost-effective steel tank with six National Pipe Thread (NPT) female connections was used as the permeate chamber. Several adapters were connected at these NPT connections and were brazed onto the steel using an oxy-acetylene torch. These adapters were then used to connect to a variety of devices and valves, including the intermediate compressor, the membrane module, and the membrane module simulation devices.

4.8.2 Fittings and Sealant

The vacuum system was equipped with many types of fittings to ensure compatibility with various components. NPTF fittings, NPT fittings, barbed hose fittings, vacuum tubing and hose clamps were used throughout the system to connect components like the permeate chamber, intermediate compressor, vacuum condenser, and condenser storage container to the each other. For example, the intermediate compressor inlet and outlet ports were adapted to barbed hose fittings by machining aluminum flanges to have NPT connections for barbed hose fitting adapters; the NPT barbed hose fitting adapters were then sealed to the aluminum flanges using an epoxy. In contrast, the vacuum pump installed used a variety of KF vacuum fittings, BSPT fittings, and Barbed hose fittings to connect to the vacuum system without having any flow restrictions.

Lox-8 paste was used as a thread sealant for all BSPT, NPT, NPTF, and barbed hose fittings to prevent leakage into the system. Lox-8 was selected because of its ability to seal threads at extreme pressures and its compatibility with wet environments due to

its waterproof nature [25]. Dow Corning vacuum grease was also used in the vacuum system; however, it was only applied on o-rings for the KF vacuum fittings.

4.8.3 Vacuum System Insulation

The vacuum system was insulated to minimize the influence of the ambient lab temperature on the vacuum fluids, especially to avoid unwanted condensation or re-evaporation. Therefore, the insulation selected throughout the vacuum system was designed for a goal of preventing any heat transfer interactions greater than 5 Watts, not including transient thermal storage interactions. A variety of insulation types were used in an effort to achieve this goal. First, the permeate chamber was surrounded with 1 inch thick, high-density polystyrene foam insulation that had a K factor of 0.20 [26]. The tubing throughout the vacuum system was then wrapped with a 1/8" thick butyl rubber pipe wrap, and then encased in 3/4" thick, soft Buna-N/PVC rubber pipe insulation that had a K factor of 0.25 [14]. Finally, the vacuum condenser was covered in 1/8" thick beutel rubber pipe wrap and was surrounded by the aforementioned 1 inch thick, high-density polystyrene foam insulation.

4.8.4 Power Input Measurements

The power consumption of the vacuum system equipment was measured using two methods: one for the single-phase equipment and one for the three-phase equipment. A Fluke 333 and Fluke 179 were used to measure current and voltage, respectively, for the single phase equipment, which consisted of the vacuum condenser water pump and the vacuum pump; this data was then used to calculate the apparent power consumption by taking the product of the voltage and current. In addition, to increase the accuracy of

the current measurements, several wire loops were made around the clamp-on ammeter (Fluke 333) so that the count uncertainty would be diminished relative to the current value.

The intermediate compressor power consumption was measured using a Wattson power meter (RS-485), which was developed to be capable of measuring three-phase equipment power consumption. The Wattson power meter was used to display the real power, reactive power, and total power consumption of the intermediate compressor in real time. Although the data for each power line and total power were recorded, a higher priority was placed on the total real power measurements since reactive power loads can be balanced using conventional compensation techniques.

4.8.5 Temperature Measurement Considerations

The temperature sensors used in the vacuum system were Pt100 Class A RTDs with 6 inch probes purchased from Omega, and in-house T-type thermocouples. Prior to testing, all of the sensors were evaluated together at room temperature for comparison to ensure that the in-house thermocouple sensor uncertainties were within the appropriate limits, which are included below.

Class A Resistance Temperature Detectors (RTD) were selected for measuring temperature at the critical temperature measurement locations. These were selected over thermocouples due to their increased accuracy; class A RTDs typically have an uncertainty of approximately 0.2°C in the operating ranges considered for this application, whereas many thermocouples operating in this same range have an uncertainty of approximately 1°C [27, 28].

Another factor considered regarding the use of RTDs was self-heating. Self-heating is essentially the conversion of electrical energy to thermal energy during RTD operation. A preliminary calculation was performed to determine the potential influence self-heating might have on the measurements. The RTD in consideration had a 100 ohm resistor and an operating current range of 4-20mA. Assuming all of this energy is converted into thermal energy, the maximum thermal energy introduced to the system is the product of the voltage times the current, approximately 0.04Watts. This was considered to be negligible in comparison to the other heat transfer rates experienced in the system.

Finally, consideration was given to the effect of probe length on the RTD measurement. RTD measurements are averaged over the entire length of the probe; therefore, the accuracy of the RTD can be reduced if the entire probe length is not exposed to the area in consideration. To avoid any problems with maldistribution along the RTD, an RTD with a 6 inch probe length was installed to cover the diameter of the permeate chamber, without allowing the end of the probe to touch the chamber. This ensured that a significant portion of the RTD was in direct contact with the vacuum fluid.

4.8.6 Pressure Measurements

The pressure measurements in the vacuum system were acquired using several Setra Model 730 Transducers with 2.7kPa and 13.3kPa pressure ranges and accuracies of $\pm 0.5\%$ of reading; in addition, vacuum gauges with the full vacuum range, 0-101kPa,

were installed on each tank for monitoring the pressures when the Setra transducers were out of range.

4.8.7 Data Acquisition and Sensors

The raw digital data was collected using National Instruments data acquisition hardware. A NI-9174, 4-slot chassis was purchased from National Instruments to stream information from the various measurement modules to the LabVIEW computer software used as an interface for real-time measurements. The four chassis slots were occupied with the following modules for each of the various measurement systems: two NI-9217, 4-channel input modules for measuring RTD readings; one NI-9213, 16-channel thermocouple module for measuring the temperatures at various locations using thermocouples; and one NI-9205 analog input module used to measure data from the pressure transducers and flow meters.

4.9 System Variable Control Methods

There were three critical vacuum system variables that required regulation for performing parametric cooling system studies: the permeate pressure, which was adjusted to reach the desired membrane outlet conditions; the condenser temperature, which was adjusted to simulate a design environmental cooling tower set point; and the condenser pressure, which was adjusted to condense the water vapor at the given condenser temperature. The vacuum system contained several control methods for adjusting these three variables, and those control methods were a variable frequency drive, manually operated gate valves, and a temperature-controlled thermal bath.

4.9.1 Variable Frequency Drive

A Toshiba VF-S7 variable frequency drive (VFD) was installed on the intermediate compressor motor in order adjust the permeate pressure, and reduce the compressor's power consumption in the process.

4.9.2 Valves

Several types of valves were initially considered for the vacuum system, including butterfly, gate, ball, and needle valves. These valves were initially selected based on optimizing the constraints of cost, flow restriction, control precision, and air leakage. The gate valves ended up having the best performance of all the valves purchased on an equal cost constraint, so these were selected to be in the vacuum system.

The gate valves selected for the vacuum system were placed before the membrane, after the permeate chamber, and after the vacuum condenser. This allowed for isolation from the membrane module, as well as flow restriction capabilities to increase the permeate pressure and condenser pressures. At fully open valve positions, the permeate and condenser pressures were at their minimum achievable pressures.

4.9.3 Condenser Chiller/Heater

An in-house Cole Parmer temperature control bath was used to control the vacuum condenser temperature. This control method was critical because the condenser temperature was designed to simulate operating cooling tower temperatures, which operate near the ambient wet bulb temperatures. In addition, for parametric studies it was essential to have a method for maintaining a constant condenser temperature.

4.10 Completed Vacuum System

The final vacuum system was assembled after incorporating all of the prior research, calculations, and preliminary test data for each of the components. A diagram showing the completed vacuum system with a sample membrane module is provided in Figure 20; in addition, the details for the variables indicated in Figure 20 are included in Table 17.

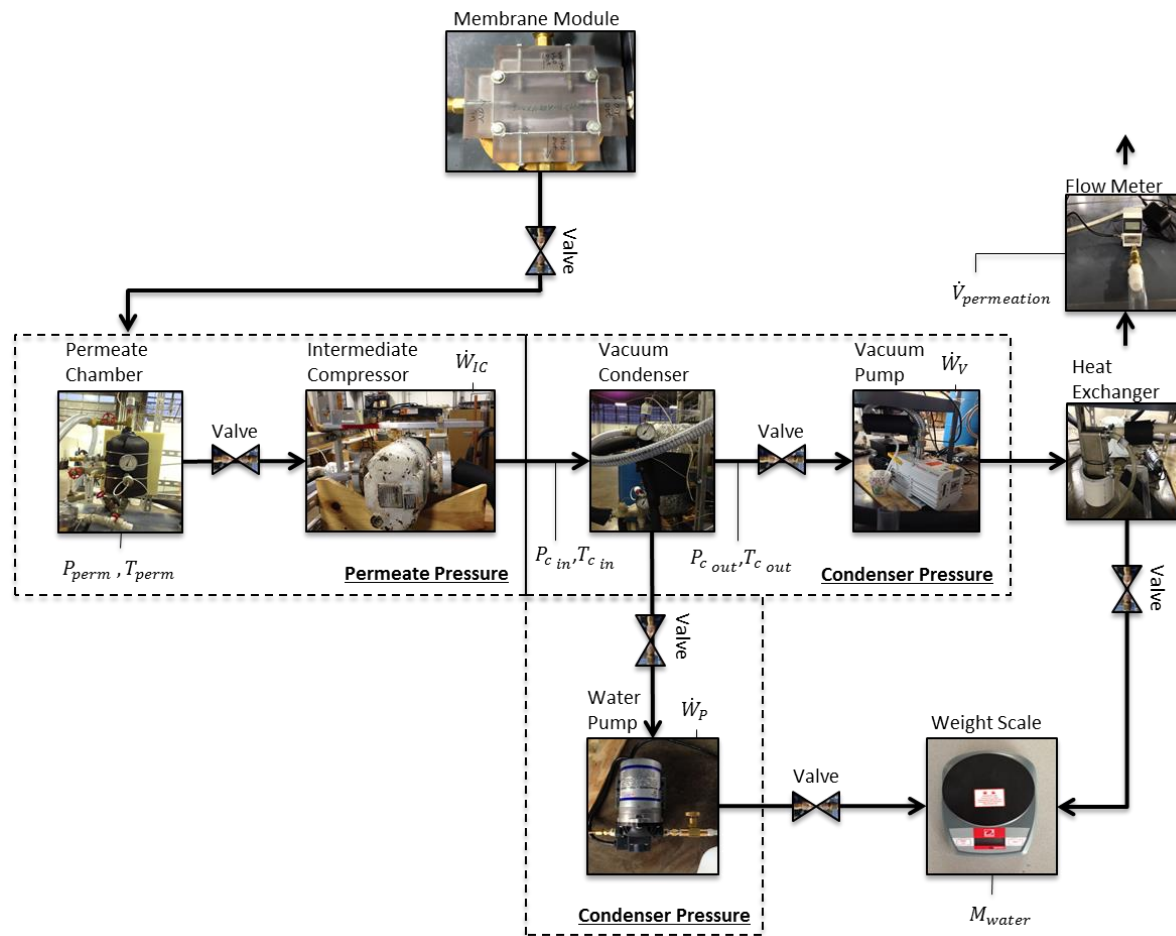


Figure 20: Completed Vacuum System

Table 17: Complete Vacuum System Variable Details

Symbol	Variable Name	Variable Details
\dot{W}_{IC}	Intermediate Compressor Power Input	Power required to pressurize all permeation fluids from permeate pressure to condenser pressure
\dot{W}_V	Vacuum Pump Power Input	Power required to reject all non-condensable gases and any remaining water vapor passing through the cooling tower simulator
\dot{W}_P	Water Pump Power Input	Power required to reject the condensed water from the vacuum system to atmospheric pressure
$\dot{V}_{permeation}$	Membrane Permeation Volumetric Flow Rate	The volumetric flow rate of the non-condensable gases that permeate through the membrane module
T_{perm}	Membrane Permeate Temperature	The temperature of the permeated gases through the membrane, located in the measurement tank
$T_{c\ in}$	Cooling Tower Inlet Temperature	The temperature of the permeated gases as they enter the cooling tower simulator heat exchanger
$T_{c\ out}$	Cooling Tower Outlet Temperature	The temperature of the permeated gases as they leave the cooling tower simulator heat exchanger
P_{perm}	Membrane Permeate Pressure	The pressure of the permeated gases through the membrane, located in the measurement tank
$P_{c\ in}$	Cooling Tower Inlet Pressure	The pressure of the permeated gases as they enter the cooling tower simulator heat exchanger
$P_{c\ out}$	Cooling Tower Outlet Pressure	The pressure of the permeated gases as they leave the cooling tower simulator heat exchanger
M_{water}	Mass of Condensed Water	The mass of all condensed water vapor permeated through the membrane

The membrane module was equipped with ¼” NPT female connections on the permeate side, which were converted to 1” ID barbed hose fittings using adapters. The module was then connected to the permeate chamber using 1” ID reinforced vacuum tubing, which was secured and sealed to the barbed fittings using hose clamps and Loctite-8 paste, respectively; this was also the method used for connecting the permeate chamber to the intermediate compressor, the intermediate compressor to the vacuum condenser, and the vacuum condenser to the vacuum pump. The vacuum condenser was connected to the water pump via ¼” copper tubing and compression fittings for an air-tight seal. In addition, the tubing at the inlet and outlet of the vacuum condenser was assembled with a downward slope towards the condenser to capture any potential water vapor condensed in the tubes. All of the valves shown in the schematic above were 1” pipe size gate valves, and were manually operated during testing. Finally, the water pump and vacuum pump outlet heat exchanger directed the water to storage containers that were then placed on top of a weight scale to measure their contents.

Prior to installing the membrane module, the vacuum system performance was evaluated using a series of tests to isolate variables such as the system air leakage and water vapor recovery method; the results for these tests are discussed in the section below.

4.11 Preliminary Vacuum System Tests

4.11.1 System Leakage Measurements

The vacuum system developed for the membrane module evacuation was constructed to prevent laboratory air from leaking into the water vapor recovery system. A constraint on the maximum allowable air leakage rate into the system was set to be 1% of the total ideal air permeation through the membrane module. In order to measure air leakage rates in this range without incurring additional equipment costs, an ideal gas law correlation was used to convert measured system pressure increases over time into mass flow rates. This increase in pressure was considered to be attributed to air leakage, since the vacuum system was isolated and dried out through continuous evacuation prior to testing. More information on the calculations used can be found in the uncertainty analysis section.

Leakage Test Results

An 82 hour leak test was performed while the pressure and temperature were monitored in order to calculate a mass change in the system. The air leakage results of this test in comparison with the calculated air permeation rates are shown in Table 18, and the complete set of results can be found in Appendix I.

Table 18: System Leakage Compared to Module Air Permeation

MODULE SIZE (SCFM)	$\dot{M}_{air\ permeated} \left(\frac{kg_{air}}{s} \right)$	$\dot{M}_{leakage} \left(\frac{kg_{air}}{s} \right)$	LEAKAGE (%)
1	1.97E-06	5.14E-09	0.2605
10	1.97E-05	5.14E-09	0.0260

The results show that the leakage into the system was below the tolerable limit of 1% of the membrane module's air permeation rates. In addition, this percent leakage would be reduced with increases in module size.

Uncertainty

A Kline & McClintock uncertainty analysis was performed in order to evaluate the uncertainty in the leakage results. The mass in the tank was evaluating using the ideal gas law shown in Equation 26.

$$m = \frac{PV}{R_{\text{specific}}T} \quad (26)$$

Substituting the ideal gas law equation into the Kline & McClintock uncertainty analysis equation for the mass of the tank yields the following.

$$\delta m_1 = \left[\left(\frac{\partial m_1}{\partial V} \delta V \right)^2 + \left(\frac{\partial m_1}{\partial T} \delta T \right)^2 + \left(\frac{\partial m_1}{\partial R_{\text{specific}}} \delta R_{\text{specific}} \right)^2 + \left(\frac{\partial m_1}{\partial P} \delta P \right)^2 \right]^{1/2} \quad (27)$$

where m_1 indicates the mass in the tank at a given time interval. The various measurement uncertainty values are shown in the equations below.

$$\delta V = \pm 0.001 \text{ m}^3 \quad (28)$$

$$\delta T = \pm 1^\circ\text{C} \quad (29)$$

$$\delta R_{\text{specific}} = 0.001 \frac{\text{kJ}}{\text{kgK}} \quad (30)$$

$$\delta P = 0.5\% \text{ of Reading} \quad (31)$$

The mass flow rate into the tank is written as the following.

$$\dot{m} = \frac{m_2 - m_1}{t_2 - t_1} \quad (32)$$

The respective Kline & McClintock uncertainty analysis for this equation yields the equation below.

$$\delta \dot{m} = \left[\left(\frac{\partial \dot{m}}{\partial m_1} \delta m_1 \right)^2 + \left(\frac{\partial \dot{m}}{\partial m_2} \delta m_2 \right)^2 + \left(\frac{\partial \dot{m}}{\partial t_1} \delta t_1 \right)^2 + \left(\frac{\partial \dot{m}}{\partial t_2} \delta t_2 \right)^2 \right]^{1/2} \quad (33)$$

assuming that $\delta t = 0$ due to the accuracy of the data acquisition system, Equation 33 simplifies to the following.

$$\delta \dot{m} = \left[\left(\frac{\partial \dot{m}}{\partial m_1} \delta m_1 \right)^2 + \left(\frac{\partial \dot{m}}{\partial m_2} \delta m_2 \right)^2 \right]^{1/2} \quad (34)$$

Substituting the appropriate values into the aforementioned Kline & McClintock equations results in a total leakage uncertainty of approximately 7%; see Appendix I for the detailed analysis on EES.

It is important to mention that over the duration of this leak test the pressure in the system increased by approximately 9 kPa. The consequence of this is that the driving pressure differential for air leakage between the ambient system and the vacuum system was changing, though only by about 10% for an atmospheric pressure of 101 kPa; however, this still must be taken into consideration when evaluating the leakage uncertainty.

4.11.2 Membrane Module Simulation

Prior to receiving a membrane module, the vacuum system performance was evaluated using components constructed to simulate the membrane module air and water vapor permeation rates for a range of potential feed air flow rates. The development of these membrane-simulator components and preliminary vacuum system test results are discussed below.

Water Vapor Permeation Simulator

The water vapor permeation through the membrane module was simulated using a water evaporation device. This device was developed by installing barbed fittings and a 400 Watt immersion heater into a clear storage container, which was then vacuum sealed using an adhesive. After water was inserted, the container was connected to the vacuum apparatus via vacuum tubing and barbed hose fittings. During operation, the water temperature inside the tank was controlled using a PID controller, which received feedback from a thermocouple inserted into a thermowell that was submerged under the water. In addition, the pressure in the evaporation device was controlled by manually adjusting the gate valve connecting the evaporation device to the vacuum system; prior to operation, the evaporation device was maintained at a rough vacuum for several hours in order to remove most of the air entrained in the water. The amount of water removed from the evaporation device was calculated by observing the volume difference of the water at atmospheric pressure both before and after the test was performed, as well as during vacuum operation. The volume difference was determined by using graduated markings on the storage container to measure height changes and then multiplying these

height changes by the known cross sectional area, which was capable of providing volume differences to a precision of less than 3mL.

Air Permeation Simulator

The air permeation through the membrane module was simulated using a manually adjustable valve connecting the vacuum system to ambient air. A rotameter was installed at the entrance of the valve to measure the air flow rate entering the vacuum system; this was installed on the ambient pressure side of the valve to ensure that the flow meter operated in its calibrated environment.

Membrane Simulation Test Results

Two tests were conducted to determine the vacuum system's water storage capacity and transient response by using the water vapor permeation simulator. The first test consisted of introducing 0.05 scfm of water vapor into the system with no air flow; prior to testing, the water vapor simulator was evacuated overnight to remove any air trapped in the water. The vacuum condenser temperature and water collection container was set to 21°C and the condenser pressure was set to 3kPa, while the vacuum pump exhaust condenser temperature was set to 13°C to recover water vapor not condensed in the vacuum condenser. The test was conducted over a period of 4.75 hours, and condensed water started exiting out of the condenser after 3.25 hours of testing . The results of the test are shown in Table 19.

Table 19: Condenser Cooling Capacity Test #1

COMPONENT	WATER VAPOR RECOVERED
Vacuum Condenser Recovery Container	93g
Vacuum Condenser Storage	92g
Vacuum Pump Exhaust Condenser	18g
<i>Total System Recovery</i>	203g
<i>Total Water Vapor Input to the System</i>	227g

The results in Table 19 indicate that the total accountability of water vapor was approximately 89%. The remainder of water vapor unaccounted for was assumed to have condensed in the vacuum pump during compression and remained entrained in the vacuum pump oil.

The second test consisted of introducing 0.05 scfm of water vapor into the system with no air flow, but at a higher condenser pressure and temperature. The condenser temperature was set to 26°C and the condenser pressure was set to 4.5kPa, while the vacuum pump exhaust condenser temperature remained at 13°C. The results of the test are shown in Table 20 below.

Table 20: Condenser Cooling Capacity Test #2

COMPONENT	WATER VAPOR RECOVERED
Vacuum Condenser Recovery Container	137g
Vacuum Condenser Storage	90g
Vacuum Pump Exhaust Condenser	17g
<i>Total System Recovery</i>	244g
<i>Total Water Vapor Input to the System</i>	303g

It is important to note that while the total accountability of water vapor was approximately 81% for this test, during steady state operation the water recovery reached as high as 96%. The overall system recovery was lower due to time spent adjusting condenser parameters. In addition, the remainder of the water was assumed to be trapped in the vacuum pump oil; this assumption was later reinforced by removing the pump oil contents and discovering condensed water.

4.12 Vacuum System Summary

The vacuum system was designed and developed with the capability of evacuating the permeate side of the membrane module using the novel membrane dehumidification-enabled cooling system design. The vacuum pump selected for the system was a Pfeiffer DUO 10 Dual Stage Rotary Vane Vacuum Pump with a 7 cfm pumping capacity, and it was preceded by an Oerlikon-Leybold WA 250 roots blower, which was selected to be the intermediate compressor. Between these two positive displacement pumps was a 60 plate heat exchanger with an effective area of 2.05m² that was temperature-controlled to simulate the vacuum condenser operation in a complete cooling system. The air leakage in the vacuum system developed was calculated to be less than 1% of the theoretical air permeation through the membrane module, and the water vapor recovery of the system was established to be 89% under a specific set of simulated operating conditions.

5. COMPLETE SYSTEM TESTS

Once the test apparatus design and construction was complete, the novel membrane dehumidification-enabled cooling system was evaluated under simulated real-world operating conditions using a membrane module with an area of 0.024 m² supplied by PNNL. The data acquired from these tests provides membrane module performance characteristics as well as a proof-of-concept for a fully functional membrane module cooling system, though not yet optimized for minimizing energy consumption. Furthermore, the preliminary results were used to evaluate test apparatus limitations and potential improvements.

5.1 Complete Test Apparatus

The feed-air system and vacuum system were combined to complete the test apparatus development. A schematic in Figure 21 below shows the complete membrane module testing system with labeled critical measurement points and the novel membrane dehumidification-enabled cooling system work input requirements; in addition, details for the variables indicated in Figure 21 are included in Table 21.

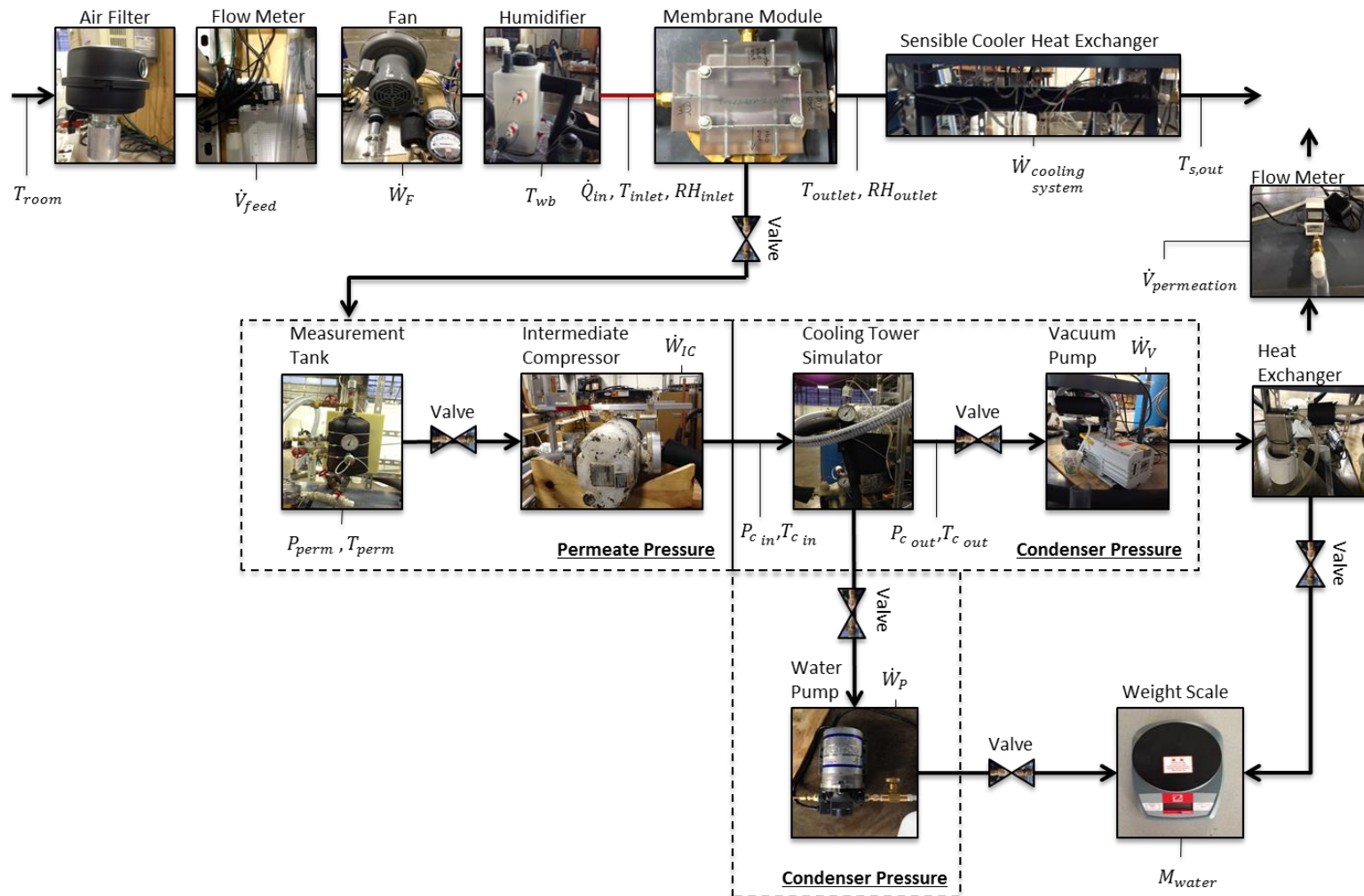


Figure 21: System Schematic

Table 21: System Schematic Legend

Symbol	Variable Name	Variable Details
\dot{W}_F	Fan Power Input	Current fan is oversized to handle humidification system flow restrictions
$\dot{W}_{cooling\ system}$	Sensible Cooling System Power Input	Consists of work input to the refrigeration system and water circulation pump
\dot{W}_{IC}	Intermediate Compressor Power Input	Power required to pressurize all permeation fluids from permeate pressure to condenser pressure
\dot{W}_V	Vacuum Pump Power Input	Power required to reject all non-condensable gases and any remaining water vapor passing through the cooling tower simulator
\dot{W}_P	Water Pump Power Input	Power required to reject the condensed water from the vacuum system to atmospheric pressure
\dot{Q}_{in}	Air Supply Heat Input	A controlled heater is used to condition the dry bulb air temperature after exiting the humidifier at saturation
\dot{V}_{feed}	Feed Air Volumetric Flow Rate	The volumetric flow rate of the feed air going through the membrane module
$\dot{V}_{permeation}$	Membrane Permeation Volumetric Flow Rate	The volumetric flow rate of the non-condensable gases that permeate through the membrane module
RH_{inlet}	Relative Humidity of Inlet Air	The inlet relative humidity is measured using a data logger that is coupled with a temperature sensor
RH_{outlet}	Relative Humidity of Outlet Air	The outlet relative humidity is measured using a data logger that is coupled with a temperature sensor
T_{wb}	Wet Bulb Temperature	The temperature of the air immediately after it passes through the humidifier section, which is at saturation
T_{room}	Room Temperature	This measures the room temperature continuously
T_{inlet}	Inlet Air Temperature	This is an RTD measurement of the air going into the membrane module
T_{outlet}	Outlet Air Temperature	This is an RTD measurement of the air leaving the membrane module
$T_{s,out}$	Sensible Cooling Air Outlet Temperature	The temperature of air as it exits the sensible heat exchanger
T_{perm}	Membrane Permeate Temperature	The temperature of the permeated gases through the membrane, located in the measurement tank
$T_{c\ in}$	Cooling Tower Inlet Temperature	The temperature of the permeated gases as they enter the cooling tower simulator heat exchanger
$T_{c\ out}$	Cooling Tower Outlet Temperature	The temperature of the permeated gases as they leave the cooling tower simulator heat exchanger
P_{perm}	Membrane Permeate Pressure	The pressure of the permeated gases through the membrane, located in the measurement tank
$P_{c\ in}$	Cooling Tower Inlet Pressure	The pressure of the permeated gases as they enter the cooling tower simulator heat exchanger
$P_{c\ out}$	Cooling Tower Outlet Pressure	The pressure of the permeated gases as they leave the cooling tower simulator heat exchanger
M_{water}	Mass of Condensed Water	The mass of all condensed water vapor permeated through the membrane

5.2 Membrane Module Performance Characterization

5.2.1 Performance Test Conditions

A series of tests were conducted to provide a preliminary performance evaluation of the novel membrane dehumidification-enabled cooling system using a membrane module designed for 1 scfm of feed air flow ($A_{\text{membrane}} = 0.024 \text{ m}^2$). In order to isolate variable dependencies, several control variables were maintained constant while others were varied; the control variables for evaluating the membrane module performance were determined to be the permeate pressure, the flow rate, the dry bulb temperature, and the humidity ratio. Air velocity distribution in the membrane was determined to be a parameter coupled with the flow rate since the membrane module inlet fittings were specified, and no reductions in area were made below that specification. In addition, the log mean pressure difference across the membrane module was accounted for through the water vapor partial pressure at the feed air side and the permeate side. The given variable parameters for the tests are shown in Table 22 below.

Table 22: Testing Control Variables

CONTROL VARIABLE	VALUE
Volumetric Flow Rate	1 scfm
Permeate Pressure	0.3-0.4 kPa
Dry Bulb Temperature	See Figure 22
Humidity Ratio	See Figure 22

The distribution of the dry-bulb temperature and humidity ratio set point conditions referenced in Table 22 are shown in Figure 22 below.

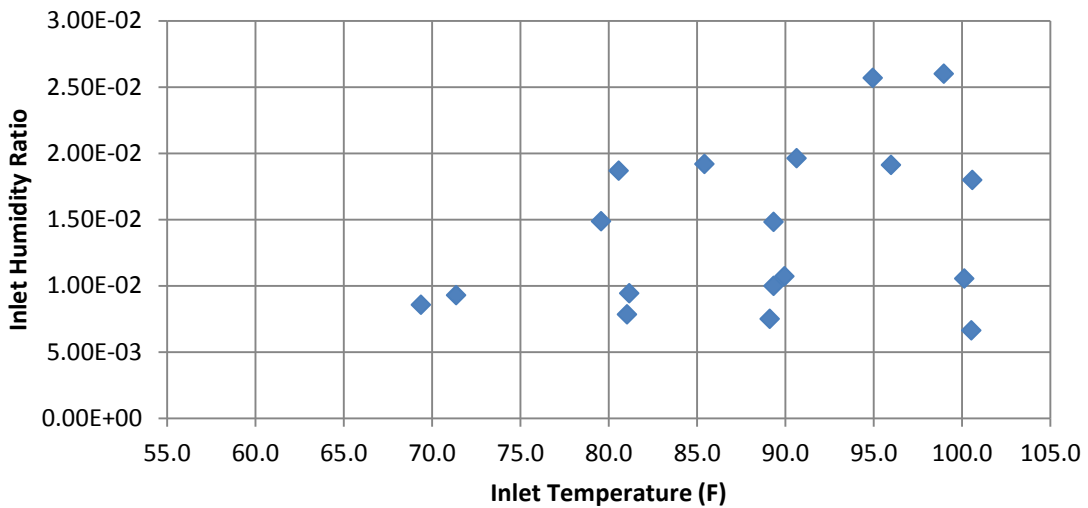


Figure 22: Temperature and Humidity Test Conditions

For several of the tests the inlet humidity ratio was set to remain constant so that the dry bulb temperature could be evaluated individually. However, occasionally the humidity ratio values did stray from the set points. This deviation was taken into account for all of the consequent calculations. Figure 23 below shows the measured inlet humidity ratios for the various set points.

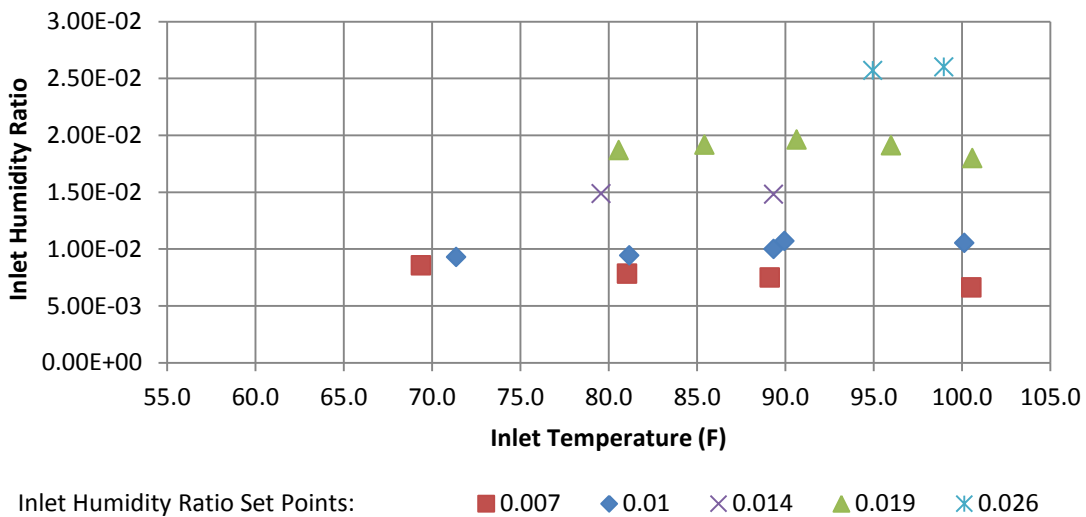


Figure 23: Humidity Ratio Variation from Set Point

As indicated by the legend in Figure 23, the inlet humidity ratio set points were chosen to range from 0.007 to 0.026, and the temperature set points were chosen to be between 70°F and 100°F. This range was chosen to contain a wide variety of common environmental operation conditions as well as less-practical, extreme test conditions in order to accentuate any membrane performance dependencies on temperature and humidity ratio. During testing, the inlet humidity ratio deviations from the set points did not exceed 0.0016, and the measured inlet humidity ratio values were tabulated along with the results.

5.2.2 Membrane Module Performance Results

The tabulated test results of the membrane’s water vapor permeance for the various aforementioned control variable operating conditions are shown in Table 23.

Table 23: Tabulated Test Results

FEED-AIR FLOW RATE [CFM]	MEMBRANE INLET TEMPERATURE [F]	INLET HUMIDITY RATIO	PERMEATE PRESSURE [KPA]	WATER VAPOR PERMEANCE [KMOL/KPA-M ² -S]
1.0	69	0.009	0.35	3.93E-06
1.0	71	0.009	0.35	4.23E-06
1.0	80	0.015	0.36	4.72E-06
1.0	81	0.019	0.34	4.70E-06
1.0	81	0.008	0.35	4.29E-06
1.0	81	0.009	0.35	4.84E-06
1.0	85	0.019	0.36	5.18E-06
1.0	89	0.007	0.35	4.71E-06
1.0	89	0.015	0.35	5.19E-06
1.0	89	0.010	0.35	5.33E-06
1.0	90	0.011	0.34	5.13E-06
1.0	91	0.020	0.37	5.58E-06
1.0	95	0.026	0.42	5.41E-06
1.0	96	0.019	0.40	5.79E-06
1.0	99	0.026	0.44	5.75E-06
1.0	100	0.011	0.36	5.88E-06
1.0	101	0.007	0.35	5.67E-06
1.0	101	0.018	0.42	5.76E-06

Throughout the tests, the feed-air flow rate and the permeate pressure were controlled to maintain a constant value; it is evident from the tabulated data that while attempts to control the feed-air flow rate were successful, there were some variations in the permeate pressures. Furthermore, it is important to note that the permeate pressure indicated in Table 23 is the total permeate pressure measured by the pressure transducer and not the water vapor permeate pressure; however, the difference between these two values was calculated by using the ideal gas law and Dalton's law to correlate air and water vapor permeation data into partial pressures of the gases, which was then incorporated into the analysis of the performance. Finally, it is important to mention that

the water vapor permeation rates used to calculate the water vapor permeance values were determined using measurements from the feed-air stream humidity ratio changes and not the water vapor recovery system.

The results shown in Table 23 indicate a water vapor permeance dependence on temperature; this relationship, decoupled from the other variables, is more clearly illustrated Figure 24 below.

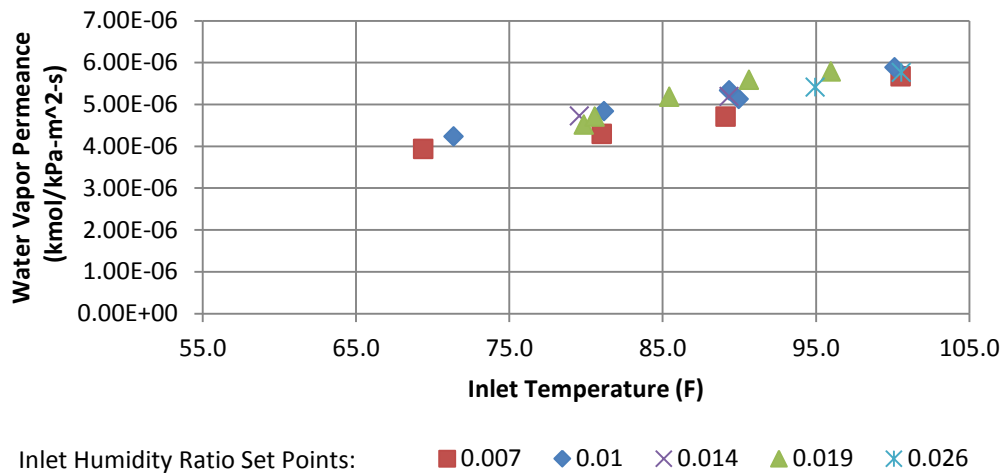


Figure 24: Water Vapor Permeance Relationship to Temperature

Figure 24 illustrates a proportional increase in water vapor permeance for feed air temperature increases; however, other control variable dependencies were also considered, with the exception of the feed-air flow rate since it remained unchanged throughout the tests. The relationship between the humidity ratio and water vapor permeance is shown in Figure 25 below.

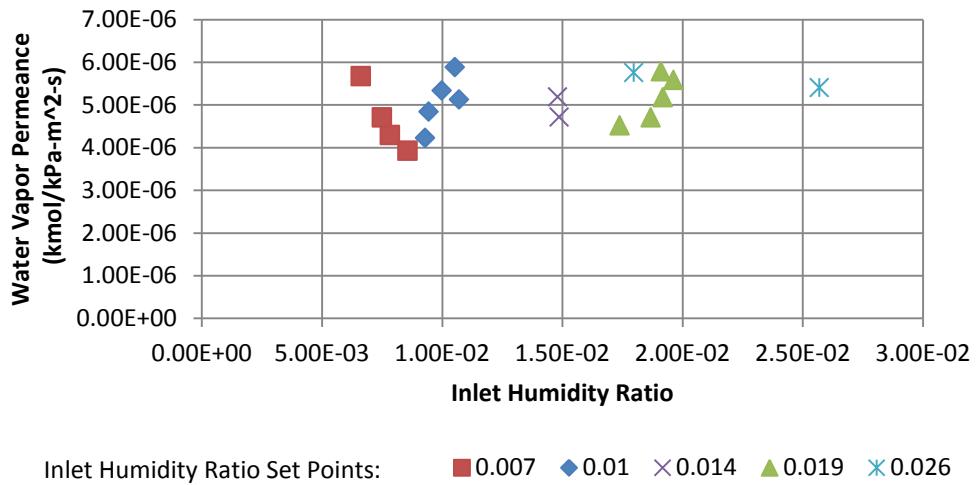


Figure 25: Water Vapor Permeance Relationship to Humidity Ratio

The data in Figure 25 supports the results illustrated in Figure 24, and also suggests that the water vapor permeance has a stronger dependence with temperature than the inlet humidity ratio under the given test conditions.

The relationship between the water vapor permeance and the permeate pressure is plotted in Figure 26 below.

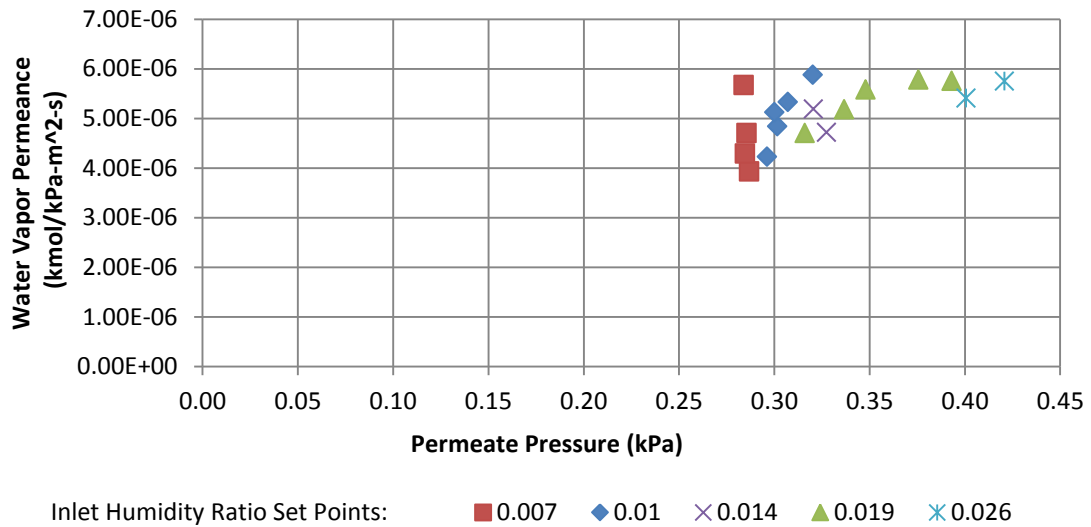


Figure 26: Water Vapor Permeance for Different Permeate Pressures

The data in Figure 26 does not indicate a clear dependence of water vapor permeance on permeate pressure. The water vapor permeance plotted with respect to more variables is shown in Appendix J.

The influence of the control variables on the water vapor permeation rate was also examined. Figure 27 below illustrates the relationship of the water vapor permeation to the membrane inlet temperature and humidity ratio.

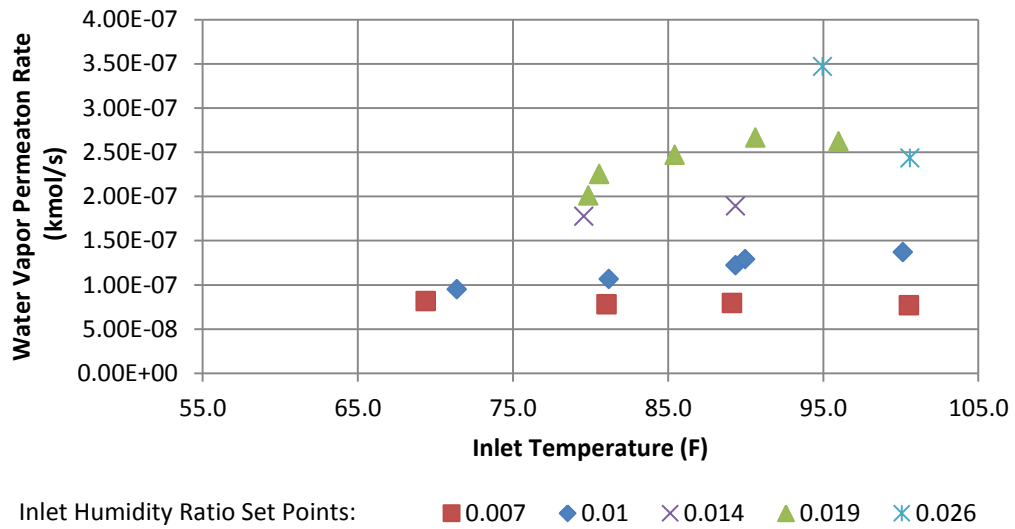


Figure 27: Water Vapor Permeation Rate for Given Temperatures

As shown in Figure 27, the water vapor permeation rate increases with inlet humidity ratio, but appears to have no general trend with respect to the inlet temperature.

Finally, the separation factor was considered over the range of inlet temperature conditions; the results for the relationship between the separation factor and inlet temperature are shown in Figure 28.

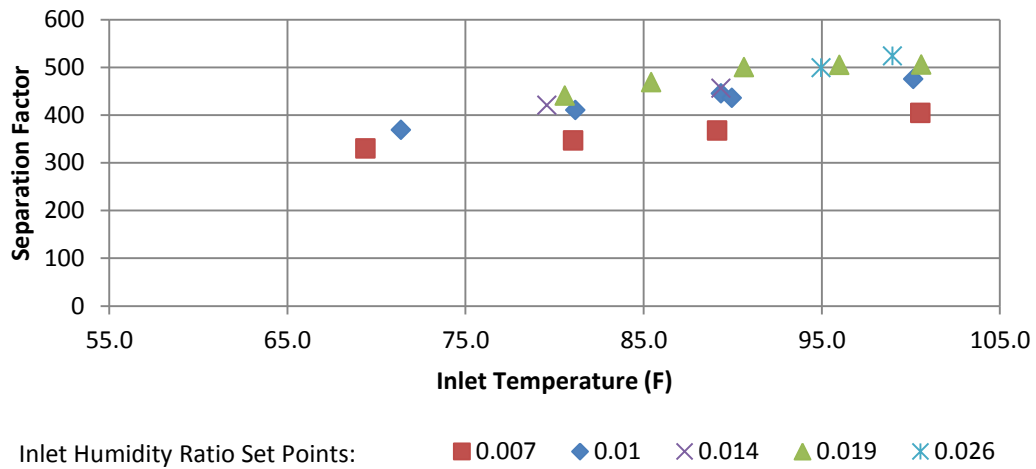


Figure 28: Separation Factors for Various Inlet Temperatures

The results shown in Figure 28 indicate a potential increase in separation factor with temperature, and a separation factor in the hundreds.

5.3 Novel Membrane Dehumidification-Enabled Cooling System Test

A complete system test was performed using the same membrane module to determine if the system was capable of achieving the ARPA-E operating conditions, which were inlet and outlet conditions of 90%RH at 90°F and 50%RH at 55°F, respectively. The results for this test are shown in Table 24.

Table 24: ARPA-E Condition Test Results

Variable	Value	Units
Feed Air Flow Rate	0.16	CFM
Inlet Dry Bulb Temperature	90	F
Inlet Relative Humidity	88	%
Inlet Humidity Ratio	0.0272	lbw/lba
Outlet Dry Bulb Temperature	76	F
Outlet Relative Humidity	13	%
Outlet Humidity Ratio	0.00241	lbw/lba
Sensible Cooler Outlet Temperature	55	F
Sensible Cooler Outlet Relative Humidity	26	%
Water Vapor Permeance	2.82E-06	kmol/kPa-m ² -s

The results indicate that the current system is capable of achieving and exceeding the cooling load requirements established by ARPA-E; this was primarily significant for establishing preliminary dehumidification performance of the novel membrane dehumidification-enabled cooling system.

The power consumption was measured for the various components of the complete cooling system; these results are shown in Table 25 below.

Table 25: Power Consumption for Membrane System

Equipment	Motor Rating	Meas. V	Meas. A	Meas. W	Calc. W
Fan	650 W	See App.	See App.	157	
Cooling Sys Pump	115 W	122.3	0.3		41
Cooling Sys Refrigeration		122.5	0.3		35
Vacuum Pump	550 W	119.3	4.5		537
Water Pump	115 W	0	0		0
Intermediate Compressor	1000 W	See App.	See App.	867	

Both the intermediate compressor and the fan had three phase motors and a variable frequency device connected to them; therefore, the power consumption was measured before the VFDs and for each power line. Only the real power component for these two pieces of equipment was included in Table 25 above. For the apparent power and individual line loads see Appendix M.

It is evident from Table 25 that a majority of the system power consumption is from the intermediate compressor and the vacuum pump, both of which were not optimized for efficiency; for example, the system power consumption could be reduced by replacing the current vacuum pump with a smaller capacity, intermittent duty vacuum pump. In addition, the remaining system components such as the fan power supply, cooling system circulation pump, and the refrigeration system are significantly oversized for the current demands.

6. CONCLUSIONS

A test facility was designed and constructed with the capability of isolating critical variables for controlling the novel membrane dehumidification-enabled cooling system's operation parameters as well as for acquiring preliminary membrane and cooling system performance measurements. The completed test facility consisted of two systems:

1. the feed-air system, which simulated the inlet-air conditions and performed the feed-air dehumidification and sensible cooling
2. the vacuum system, which evacuated the permeate side of the membrane module to enable the feed-air dehumidification.

The feed-air system as constructed was able to supply membrane-inlet flow rates up to 10 scfm over a range of temperature and relative humidity conditions, including 90°F and 90%RH, which was specified by the project sponsor. In addition, the feed-air system components included a membrane module installation site for dehumidification as well as a sensible cooling system to cool the membrane-outlet air down to the 55°F and 50%RH conditions again specified by the sponsor. Measurement stations were placed at the membrane-inlet, membrane-outlet, and the sensible cooler outlet to measure the temperature and relative humidity at these critical locations. The vacuum system as built used a Pfeiffer DUO 10 Vacuum Pump with a 7 cfm pumping capacity, which was preceded by a 60 plate heat exchanger with an effective area of 2.05m² and an Oerlikon-Leybold WA 250 roots blower. The air leakage in the vacuum system was calculated to be less than 1% of the theoretical air permeation through the membrane

module. Finally, the apparatus was constructed with the capability of measuring the power consumption of the equipment used for the dehumidification and sensible cooling process.

The functionality of the test facility was demonstrated through preliminary testing of the membrane module and the operation of the complete cooling system. The results suggested that the membrane material exhibited an increase in water vapor permeance from temperatures of 70 to 100°F, with permeance values ranging from $3.93 \cdot 10^{-6}$ to $5.88 \cdot 10^{-6} \frac{\text{kmol}}{\text{kPa} \cdot \text{m}^2 \cdot \text{s}}$. In addition, the results indicated that the novel membrane dehumidification-enabled cooling system was capable of achieving the specified operating conditions at a feed-air flow rate of 0.16 scfm by using a membrane module area of 0.024m².

REFERENCES

- [1] "Why Buildings." United Nations Environment Programme (UNEP) – SBCI. Accessed 27 January, 2014. <http://www.unep.org/sbci/AboutSBCI/Background.asp>.
- [2] Moxson, V., W. Liu, and D. Claridge. "High Efficient, On-Line Membrane Air Dehumidifier Enabling Sensible Cooling for Warm and Humid Climates." Unpublished Manuscript.
- [3] F-Chart Software. Engineering Equation Solver. Academic Version 9.445. 1992.
- [4] Bynum, J. D. "Thermodynamic Modeling of a Membrane Dehumidification System." PhD Dissertation, Texas A&M, (2012) 40-73.
- [5] Ito, A. "Dehumidification of Air by a Hygroscopic Liquid Membrane Supported on Surface of a Hydrophobic Microporous Membrane." *Journal of Membrane Science*, Vol. 175, No. 1, (2000) 36-41.
- [6] Ito, A. "Dehumidification and Humidification of Air by Surface-Soaked Liquid Membrane Module with Triethylene Glycol." *Journal of Membrane Science*, Vol. 325, No. 2, (2008) 1007-1011.
- [7] Scovazzo, P. and A. J. Scovazzo. "Isothermal Dehumidification or Gas Drying Using Vacuum Sweep Dehumidification." *Applied Thermal Engineering*, Vol. 50, No. 1, (2013) 225-231.
- [8] Danielson, P. "The Effects of Humidity on Vacuum Systems." *A Journal of Practical and Useful Vacuum Technology*. Accessed 15 October, 2012. <http://www.vacuumlabor.com/articles.htm>.

- [9] Danielson, P. "Desorbing Water in Vacuum Systems: Bakeout or UV?" A Journal of Practical and Useful Vacuum Technology. Accessed 15 October, 2012.
<http://www.vacuumbiol.com/articles.htm>.
- [10] Podesta, Michael D., Gavin Sutton, Robin Underwood, Stephanie Bell, Mark Stevens, Thomas Byrne, and Patrick Josephs-Franks. "Outgassing of Water Vapour, and its Significance in Experiments to Determine the Boltzmann Constant." Metrologia, Vol. 48, No. 1, (2010) L1-L5.
- [11] Fox, Robert W., Philip J. Pritchard, and Alan T. McDonald. "Calculation of Head Loss." In Introduction to Fluid Mechanics. Seventh ed., 329-330: John Wiley & Sons, Inc., 2009.
- [12] "Friction Factor." Piping-Designer. Accessed 13 November, 2012. http://piping-designer.com/Friction_Factor.
- [13] "Roughness & Surface Coefficients of Ventilation Ducts." The Engineering ToolBox. Accessed 13 November, 2012. http://www.engineeringtoolbox.com/surface-roughness-ventilation-ducts-d_209.html.
- [14] "Unslit Foam Rubber Pipe Insulation." Accessed 5 February, 2013. McMaster-Carr. <http://www.mcmaster.com/#4463k192/=s1dcup>.
- [15] Umrath, Walter. "Vacuum Physics." In Fundamentals of Vacuum Technology: Oerlikon leybold vacuum, (2007) 9-18.
- [16] "Duo 10m: Pfeiffer Vacuum Operation Manual." Pfeiffer Vacuum. Accessed 6 August, 2012.

- [17] "DUO 10 M, 1-Phase Motor, 100-110 V, 50 Hz; 100-120 V, 60 Hz." Pfeiffer Vacuum. Accessed 6 August, 2012. <http://www.pfeiffer-vacuum.com/products/rotary-vane-pumps/two-stage/duoline/duo-10-m/onlinecatalog.action?detailPdoId=1911#product-technical-data>.
- [18] *Private Communication*. Pfeiffer Vacuum Specialist. 03 September, 2012 to 6 December 2012.
- [19] Vasgaard, Jeff. "Generation of Vacuum: Pfeiffer Vacuum." Pfeiffer Vacuum. Accessed 04 October, 2012.
- [20] Pfeiffer Vacuum Website. Accessed 6 August, 2012. <http://www.pfeiffer-vacuum.com/>
- [21] Incropera, Frank P., David P. Dewitt, Theodore L. Berman, and Adrienne S. Lavine. "Laminar Film Condensation on a Vertical Plate." In *Fundamentals of Heat and Mass Transfer*. Sixth ed., 646: John Wiley & Sons, Inc., 2007.
- [22] "Heat Transfer Coefficients." H&C Heat Transfer Solutions, Inc. Accessed 5 November, 2013. <http://www.hcheattransfer.com/coefficients.html>.
- [23] "Typical overall Heat Transfer Coefficients (u-Values)." ENGINEERING page. Accessed 5 November, 2013. <http://www.engineeringpage.com/technology/thermal/transfer.html>.
- [24] "U in Heat Exchangers." Accessed 5 November, 2013. <http://www.cheresources.com/content/articles/heat-transfer/u-in-heat-exchangers>.
- [25] "Lox-8 Thread Sealants." FLUORAMICS, INC. Accessed 13 August, 2012. <http://www.fluoramics.com/lox8.shtml>.

[26] "Lightweight Polystyrene Foam Insulation." McMaster-Carr. Accessed 23 September, 2013. <http://www.mcmaster.com/#9255k1/=s2dvwp>.

[27] "What are RTD Sensors? Why use them? how do they Work?" Omega. Accessed 13 November, 2012.

http://www.omega.com/Temperature/pdf/RTD_Gen_Specs_Ref.pdf.

[28] "Introduction to Thermocouples." Omega. Accessed 13 November, 2012.

<http://www.omega.com/productinfo/thermocouples.html>.

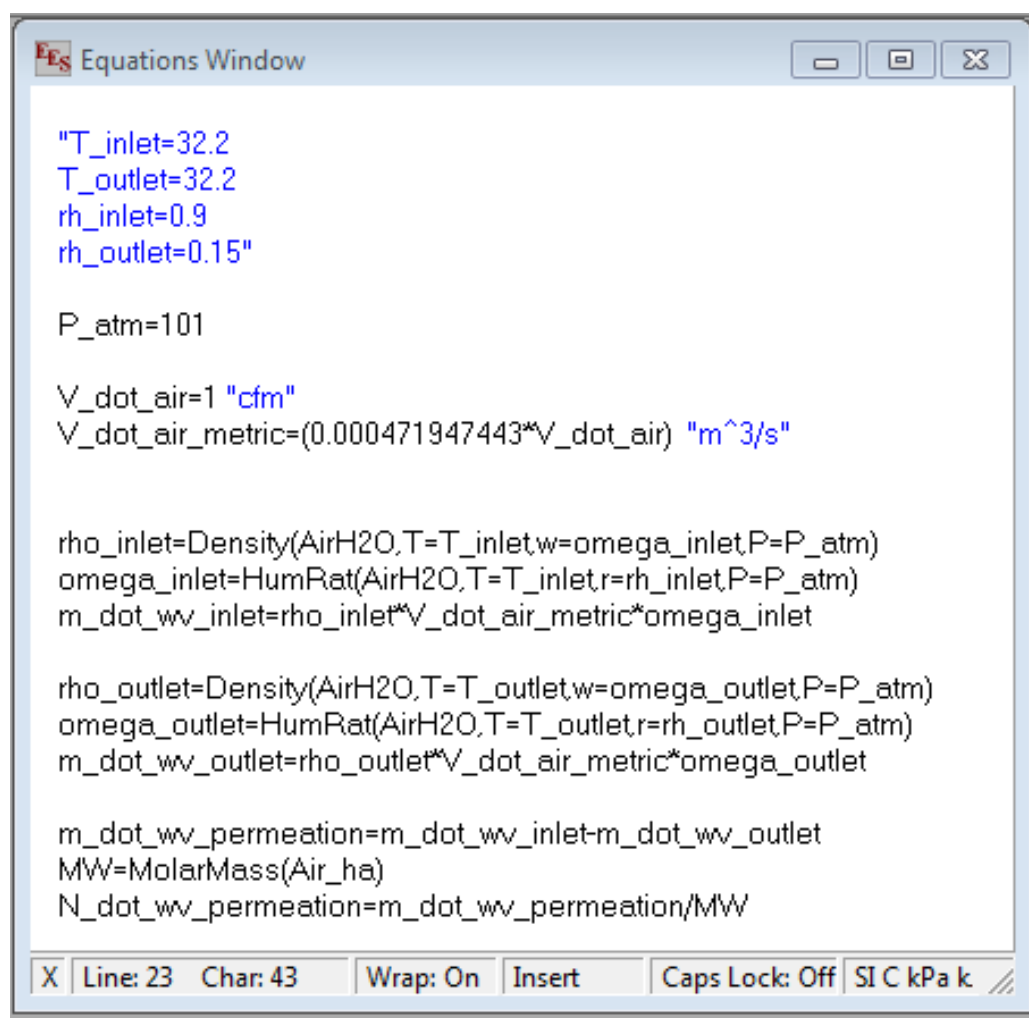
[29] "RUVAC WA/WAU " Leybold Vacuum. Accessed 6 August, 2012.

http://www.idealvac.com/files/ManualsII/Leybold_RUVAC_WA_WAU_151_251_501_1001_2001_Users_Manuals.pdf.

APPENDIX A

WATER VAPOR PERMEATION UNCERTAINTY

Preliminary water vapor permeation calculations were performed to determine the propagation of uncertainty that might occur from specific sensor uncertainties, as discussed in Section 3.4. EES was used to calculate the uncertainty propagation using the equations shown in Figure 29.



```
"T_inlet=32.2
T_outlet=32.2
rh_inlet=0.9
rh_outlet=0.15"

P_atm=101

V_dot_air=1 "cfm"
V_dot_air_metric=(0.000471947443*V_dot_air) "m^3/s"

rho_inlet=Density(AirH2O,T=T_inlet,w=omega_inlet,P=P_atm)
omega_inlet=HumRat(AirH2O,T=T_inlet,r=rh_inlet,P=P_atm)
m_dot_wv_inlet=rho_inlet*V_dot_air_metric*omega_inlet

rho_outlet=Density(AirH2O,T=T_outlet,w=omega_outlet,P=P_atm)
omega_outlet=HumRat(AirH2O,T=T_outlet,r=rh_outlet,P=P_atm)
m_dot_wv_outlet=rho_outlet*V_dot_air_metric*omega_outlet

m_dot_wv_permeation=m_dot_wv_inlet-m_dot_wv_outlet
MW=MolarMass(Air_ha)
N_dot_wv_permeation=m_dot_wv_permeation/MW
```

X Line: 23 Char: 43 Wrap: On Insert Caps Lock: Off SI C kPa k //

Figure 29: Water Vapor Permeation Uncertainty EES Code

The EES file uses the atmospheric pressure (P_{atm}), the feed-air volumetric flow rate (V_{dot_air}), the various densities (ρ_{inlet} , ρ_{outlet}), and the various humidity ratios (ω_{inlet} , ω_{outlet}) to calculate the water vapor mass flow rates ($m_{dot_wv_inlet}$, $m_{dot_wv_outlet}$), the water vapor permeation mass flow rate ($m_{dot_wv_permeation}$), and the water vapor permeation molar flow rate ($N_{dot_wv_permeation}$). In addition, EES was able to output the uncertainty propagation for set variable uncertainty inputs; these inputs are shown in Figure 30.

Variable	Value	Units	Absolute Uncertainty	Relative Uncertainty
P_atm	101		1	
rh_inlet	0.9		0.03	
rh_outlet	0.55		0.03	
T_inlet	20		0.3	
T_outlet	20		0.3	
V_dot_air	1		0.053	

Figure 30: Water Vapor Permeation Uncertainty EES Values

The results for the water vapor permeation molar flow rates and uncertainty propagation are shown in Table 26 below for various temperature and relative humidity conditions.

Table 26: Water Vapor Permeation EES Results

$T_{inlet}[C]$	$T_{outlet}[C]$	$RH_{inlet}[\%]$	$RH_{outlet}[\%]$	$\dot{N}_{wv,permeation}[\frac{kmol}{s}]$	$\delta [\%]$
0.9	0.15	32.2	32.2	4.18E-07	7.99%
0.8	0.15	32.2	32.2	3.62E-07	8.64%
0.7	0.15	32.2	32.2	3.06E-07	9.59%
0.6	0.15	32.2	32.2	2.51E-07	11.04%
0.5	0.15	32.2	32.2	1.95E-07	13.44%
0.9	0.15	32.2	32.2	4.18E-07	7.99%
0.9	0.25	32.2	32.2	3.62E-07	8.71%
0.9	0.35	32.2	32.2	3.06E-07	9.77%
0.9	0.45	32.2	32.2	2.51E-07	11.39%
0.9	0.55	32.2	32.2	1.95E-07	14.08%
0.9	0.15	25	25	2.82E-07	8.02%
0.8	0.15	25	25	2.44E-07	8.67%
0.7	0.15	25	25	2.07E-07	9.61%
0.6	0.15	25	25	1.69E-07	11.06%
0.5	0.15	25	25	1.31E-07	13.47%
0.9	0.15	25	25	2.82E-07	8.02%
0.9	0.25	25	25	2.44E-07	8.75%
0.9	0.35	25	25	2.07E-07	9.82%
0.9	0.45	25	25	1.69E-07	11.46%
0.9	0.55	25	25	1.31E-07	14.17%
0.9	0.15	20	20	2.11E-07	8.04%
0.8	0.15	20	20	1.83E-07	8.69%
0.7	0.15	20	20	1.55E-07	9.63%
0.6	0.15	20	20	1.27E-07	11.08%
0.5	0.15	20	20	9.86E-08	13.48%
0.9	0.15	20	20	2.11E-07	8.04%
0.9	0.25	20	20	1.83E-07	8.78%
0.9	0.35	20	20	1.55E-07	9.85%
0.9	0.45	20	20	1.27E-07	11.51%
0.9	0.55	20	20	9.86E-08	14.25%

APPENDIX B

HUMIDITY SENSOR CALIBRATION TEST DATA

Section 3.5 discussed the salt calibration tests that were used to determine the total uncertainty of the humidity sensors used in the test apparatus. Several humidity ranges were tested using different salt saturation mixtures, and the data recorded during these calibration tests is included in the tables below (Table 27 through Table 30), which also contain information about the time durations and calibration instruments uncertainties as well.

Table 27: Potassium Sulfate Calibration

POTASSIUM SULFATE CALIBRATION	TEST #	TIME ELAPSED [HRS]	TIME TO REACH STABILITY [HRS]	MEASURED		CALIBRATED INSTRUMENT		APPROXIMATE SENSOR UNCERTAINTY (%RH)
				Average Relative Humidity [%]	Std. Dev.	Relative Humidity [%]	Uncertainty	
Sensor #1 DCC6	1	24	3.5	97.38	0.52	97.45	±0.49	1.64
	2	71	60	98.59	0.47	97.45	±0.49	1.88
Sensor #2 B2E	1	71	35	98.12	0.43	97.45	±0.49	1.53
Sensor #3 B7F9	1	71	37	98.48	0.48	97.45	±0.49	1.83

The potassium sulfate calibration test was performed to test the sensor performance in the upper relative humidity range.

Table 28: Magnesium Chloride Calibration

MAGNESIUM CHLORIDE CALIBRATION	TEST #	TIME ELAPSED	TIME TO REACH STABILITY [HRS]	MEASURED		CALIBRATED INSTRUMENT		APPROXIMATE SENSOR UNCERTAINTY (%RH)
				Average Relative Humidity [%]	Std. Dev.	Relative Humidity [%]	Uncertainty	
Sensor #1 DCC6	1	68	5	35.38	0.42	32.93	±0.17	2.80
	2	138	50	35.55	0.39	32.93	±0.17	2.91
Sensor #2 B2E	1	138	51	35.45	0.35	32.93	±0.17	2.77
Sensor #3 B7F9	1	138	50	35.35	0.36	32.93	±0.17	2.70

The potassium sulfate calibration test was performed to test the sensor performance in the middle relative humidity range.

Table 29: Sodium Chloride Calibration

SODIUM CHLORIDE CALIBRATION	TEST #	TIME ELAPSED	TIME TO REACH STABILITY [HRS]	MEASURED		CALIBRATED INSTRUMENT		APPROXIMATE SENSOR UNCERTAINTY (%RH)
				Average Relative Humidity [%]	Std. Dev.	Relative Humidity [%]	Uncertainty	
Sensor #1 DCC6	1	98	64	77.60	0.55	75.38	±0.13	2.80
Sensor #2 B2E	1	98	66	77.32	0.40	75.38	±0.13	2.33
Sensor #3 B7F9	1	98	29	77.42	0.37	75.38	±0.13	2.37

The potassium sulfate calibration test was performed to test the sensor performance in the lower relative humidity range.

Temperature effects were also given consideration for these calibration tests. The temperature values recorded during all of the calibration tests are included together in Table 30 for comparison.

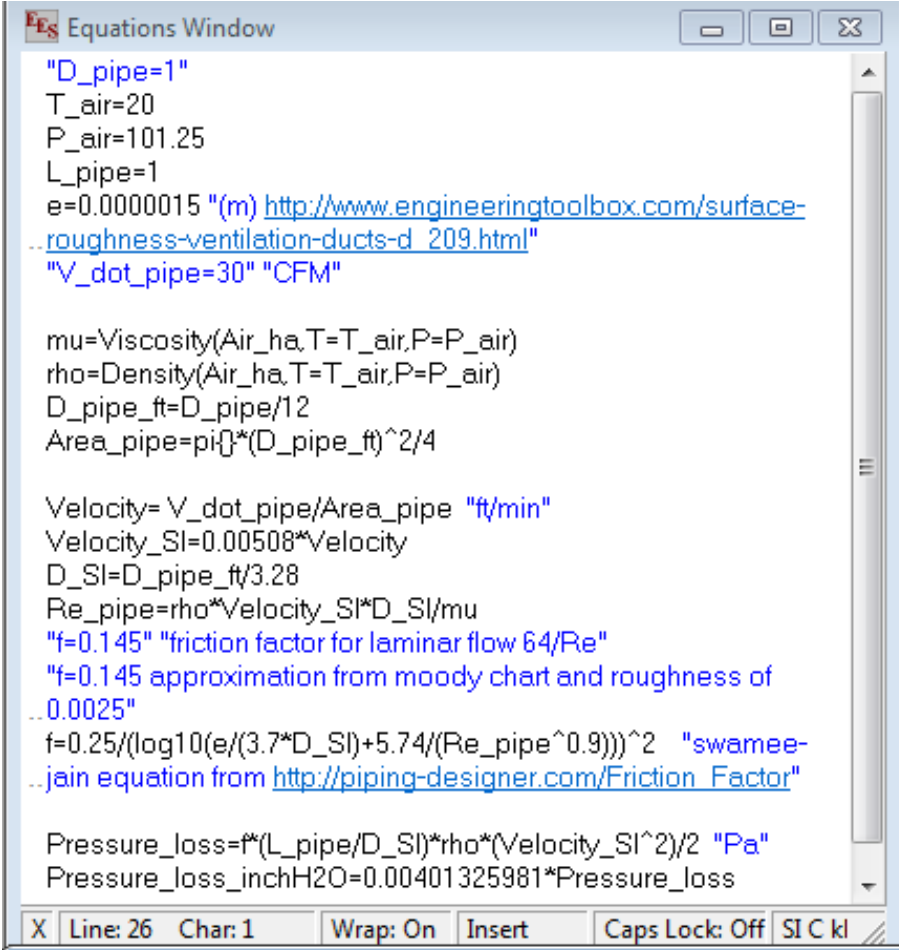
Table 30: Calibration Temperatures Comparison

SALT CALIBRATION	TEMPERATURE MEASUREMENTS [°C]		
	Sensor #1 DCC6	Sensor #2 B2E	Sensor #3 B7F9
K_2SO_4	20.9	21	21.1
$MgCl_2$	22.9	22.8	22.9
$NaCl$	22.9	22.7	23.1

APPENDIX C

FEED-AIR PIPE PRESSURE DROP CALCULATIONS

The feed-air pipe size, discussed in Section 3.6, was determined based on a several factors, most importantly the pressure drop across the pipe for various flow conditions. Variables mu (μ_l)



```
"D_pipe=1"
T_air=20
P_air=101.25
L_pipe=1
e=0.0000015 "(m) http://www.engineeringtoolbox.com/surface-roughness-ventilation-ducts-d\_209.html"
"V_dot_pipe=30" "CFM"

mu=Viscosity(Air_ha,T=T_air,P=P_air)
rho=Density(Air_ha,T=T_air,P=P_air)
D_pipe_ft=D_pipe/12
Area_pipe=pi*(D_pipe_ft)^2/4

Velocity= V_dot_pipe/Area_pipe "ft/min"
Velocity_SI=0.00508*Velocity
D_SI=D_pipe_ft/3.28
Re_pipe=rho*Velocity_SI*D_SI/mu
"f=0.145" "friction factor for laminar flow 64/Re"
"f=0.145 approximation from moody chart and roughness of 0.0025"
f=0.25/(log10(e/(3.7*D_SI)+5.74/(Re_pipe^0.9)))^2 "swamee-jain equation from http://piping-designer.com/Friction\_Factor"

Pressure_loss=f*(L_pipe/D_SI)*rho*(Velocity_SI^2)/2 "Pa"
Pressure_loss_inchH2O=0.00401325981*Pressure_loss
```

X Line: 26 Char: 1 Wrap: On Insert Caps Lock: Off SI C kl

Figure 31: Feed-Air Pipe Pressure Drop EES Code

	1	2	3	4	5
1.3	D_{pipe}	\dot{V}_{pipe}	Velocity _{SI}	Re_{pipe}	Pressure _{loss,inc}
Run 1	0.5	10	37.26	31284	6.204
Run 2	1	10	9.314	15642	0.2277
Run 3	1.5	10	4.14	10428	0.03332

Figure 32: Feed-Air Pipe Pressure Drop EES Results

APPENDIX D

WA 251 OPERATION SPECIFICATIONS

The performance characteristics of the intermediate compressor are included in Figure 33; these were useful for determining the compressor's pumping capabilities and power consumption.

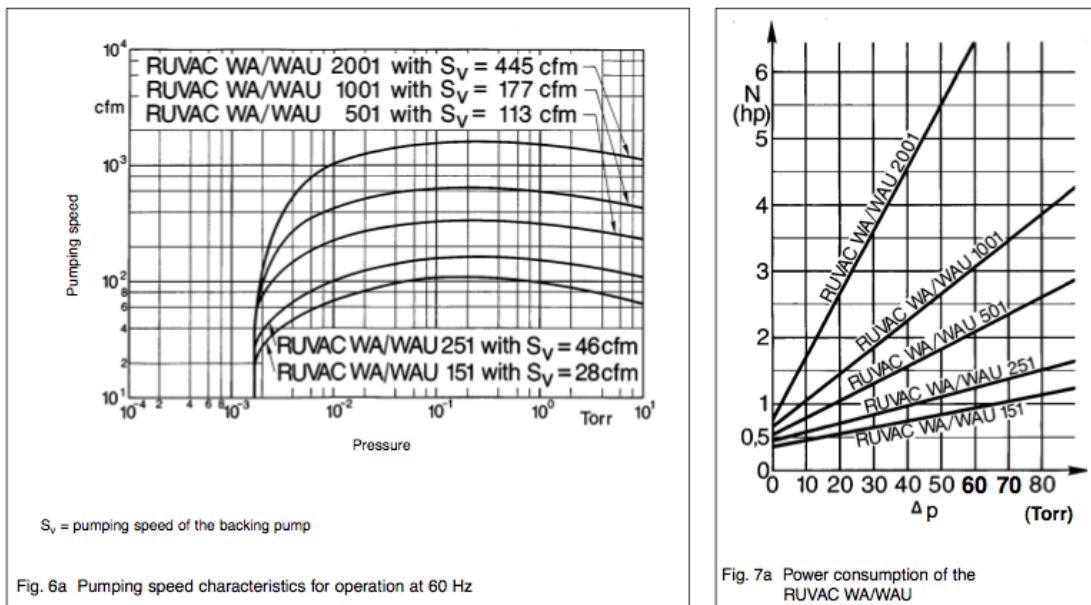


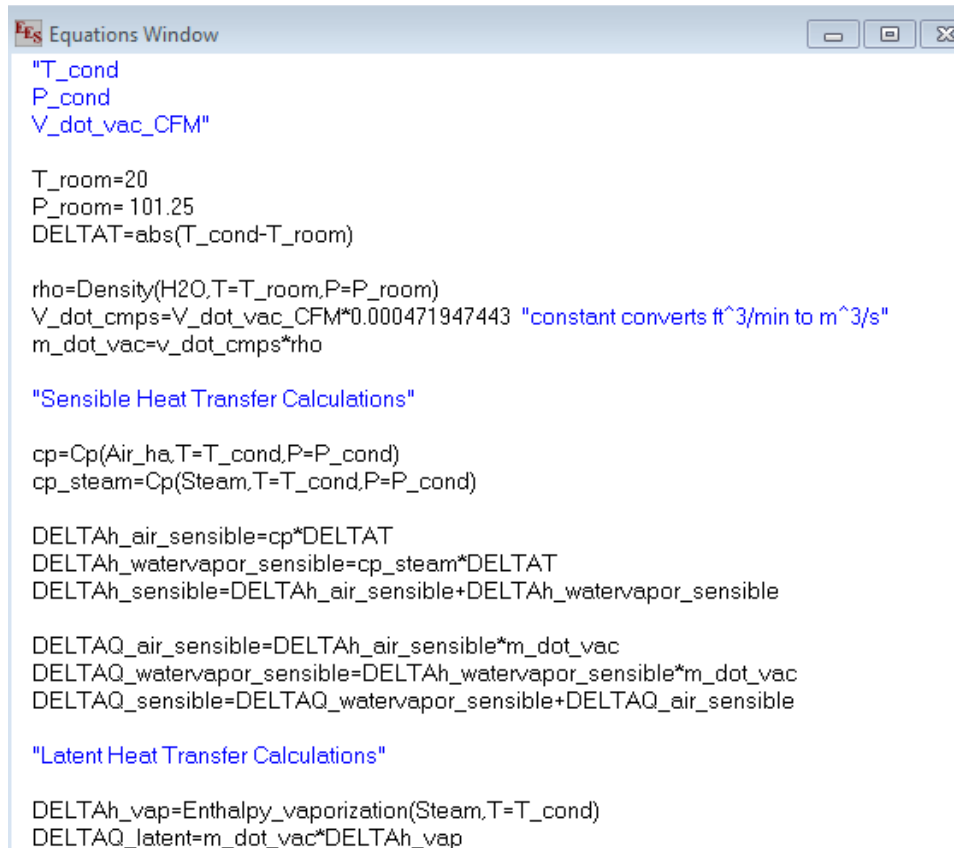
Figure 33: WA 251 Roots Blower Characteristics [29]

It is important to note that the WA 251 roots blower's performance is affected by the backing pump performance; therefore, the pumping speed of the WA 251 could change significantly depending on how significantly the backing pump performance is adjusted.

APPENDIX E

HEAT TRANSFER CALCULATIONS

EES was used to calculate realistic sensible and latent cooling/heating loads for a fixed room temperature environment, similar to the environment surrounding the test apparatus. The EES file is shown in Figure 34.



```
Equations Window
"T_cond
P_cond
V_dot_vac_CFM"

T_room=20
P_room= 101.25
DELTAT=abs(T_cond-T_room)

rho=Density(H2O,T=T_room,P=P_room)
V_dot_cmps=V_dot_vac_CFM*0.000471947443 "constant converts ft^3/min to m^3/s"
m_dot_vac=v_dot_cmps*rho

"Sensible Heat Transfer Calculations"

cp=Cp(Air_ha,T=T_cond,P=P_cond)
cp_steam=Cp(Steam,T=T_cond,P=P_cond)

DELTah_air_sensible=cp*DELTAT
DELTah_watervapor_sensible=cp_steam*DELTAT
DELTah_sensible=DELTah_air_sensible+DELTah_watervapor_sensible

DELTAQ_air_sensible=DELTah_air_sensible*m_dot_vac
DELTAQ_watervapor_sensible=DELTah_watervapor_sensible*m_dot_vac
DELTAQ_sensible=DELTAQ_watervapor_sensible+DELTAQ_air_sensible

"Latent Heat Transfer Calculations"

DELTah_vap=Enthalpy_vaporization(Steam,T=T_cond)
DELTAQ_latent=m_dot_vac*DELTah_vap
```

Figure 34: Sensible and Latent Load Comparison Calculations EES Code

The EES file uses the condenser temperature (T_{cond}), condenser pressure (P_{cond}), and the volumetric flow rate (at STP conditions) entering the vacuum system ($V_{\text{dot_vac_CFM}}$) to calculate the sensible and latent cooling loads required by the condenser. The other variables used throughout this EES code are defined in Table 31.

Table 31: EES Code Variable Information

EES VARIABLE	VARIABLE DEFINITION
T_room	Room temperature
P_room	Atmospheric pressure
DELTAT	Absolute value of the temperature difference between the room and the condenser
Rho	Water vapor density
V_dot_cmps	Volumetric flow rate entering the vacuum system converted into the units specified in the code
m_dot_vac	Mass flow rate of the water vapor entering the vacuum system
cp	Specific heat of air
Cp	Specific heat of water vapor
DELTAh_air_sensible	Sensible specific enthalpy cooling load due to air
DELTAh_watervapor_sensible	Sensible specific enthalpy cooling load due to water vapor
DELTAh_sensible	Total sensible specific enthalpy cooling load
DELTAQ_air_sensible	Sensible cooling load due to air
DELTAQ_watervapor_sensible	Sensible cooling load due to water vapor
DELTAQ_sensible	Total sensible cooling load
DELTAh_vap	Specific enthalpy of vaporization
DELTAQ_vap	Latent cooling load

The EES calculated results for a constant volumetric flow rate entering the vacuum system at different condenser temperatures and pressures are shown in Figure 35.

The screenshot shows a window titled "EES Parametric Table" containing a table with 6 rows and 6 columns. The columns are labeled: 1 (Run), 2 (T_{cond}), 3 (P_{cond}), 4 (V_{vac,CFM}), 5 (ΔQ_{latent}), and 6 (ΔQ_{sensible}). The data for each run is as follows:

Run	T _{cond}	P _{cond}	V _{vac,CFM}	ΔQ _{latent}	ΔQ _{sensible}
Run 1	10	1.4	1	0.8749	0.01834
Run 2	15	1.9	1	0.8707	0.009163
Run 3	20	2.5	1	0.8665	0
Run 4	25	3.4	1	0.8624	0.009163
Run 5	30	4.4	1	0.8582	0.01833
Run 6	35	5.8	1	0.854	0.02749

Figure 35: Sensible and Latent Load Comparison Calculations EES Results

The results for several of these iterations of calculations performed in EES and pasted into Microsoft Excel are shown in Figure 36.

T_cond (C)	P_cond (kPa)	V_vac scfr	Q_lat (kW)	Q_sensible (kW)	Tolerable Heat Transfer (W)
10	1.4	1	0.8749	0.01479	43.745
15	1.9	1	0.8707	0.007389	43.535
20	2.5	1	0.8665	0	43.325
25	3.4	1	0.8624	0.007388	43.12
30	4.4	1	0.8582	0.01478	42.91
35	5.8	1	0.854	0.02216	42.7
T_cond (C)	P_cond (kPa)	V_vac scfr	Q_lat (kW)	Q_sensible (kW)	Tolerable Heat Transfer (W)
10	1.4	0.3	0.2625	0.004438	13.125
15	1.9	0.3	0.2612	0.002217	13.06
20	2.5	0.3	0.26	0	13
25	3.4	0.3	0.2587	0.002216	12.935
30	4.4	0.3	0.2575	0.004433	12.875
35	5.8	0.3	0.2562	0.006649	12.81
T_cond (C)	P_cond (kPa)	V_vac scfr	Q_lat (kW)	Q_sensible (kW)	Tolerable Heat Transfer (W)
10	1.4	0.03	0.02625	0.0004438	1.3125
15	1.9	0.03	0.02612	0.0002217	1.306
20	2.5	0.03	0.026	0	1.3
25	3.4	0.03	0.02587	0.0002216	1.2935
30	4.4	0.03	0.02575	0.0004433	1.2875
35	5.8	0.03	0.02562	0.0006649	1.281
T_cond (C)	P_cond (kPa)	V_vac scfr	Q_lat (kW)	Q_sensible (kW)	Tolerable Heat Transfer (W)
10	1.4	0.01	0.008749	0.0001479	0.43745
15	1.9	0.01	0.008707	0.00007389	0.43535
20	2.5	0.01	0.008665	0	0.43325
25	3.4	0.01	0.008624	0.00007388	0.4312
30	4.4	0.01	0.008582	0.0001478	0.4291
35	5.8	0.01	0.00854	0.0002216	0.427

Figure 36: Sensible and Latent Condenser Loads for Various Conditions

APPENDIX F

CONDENSER CALCULATIONS

The condenser heat transfer coefficient calculations discussed in Chapter 4 are shown in Figure 37 below, along with the variable values used for the calculations.

The screenshot shows two windows from the EES software. The top window, titled "Equations Window", contains the following code:

```
P_cond=5 "kPa"  
g= 9.81 "m^s^2"  
T_cond= 30 "C"  
L=0.3  
rho_v=Density(Steam,T=T_cond,P=4)  
rho_l=Density(Water,T=T_cond,P=P_cond)  
mu=Viscosity(Water,T=T_cond,P=P_cond)  
k=Conductivity(Water,T=T_cond,P=P_cond)  
  
T_sat=T_sat(Steam,P=P_cond)  
DELTAh_vap=Enthalpy_vaporization(Steam,T=T_sat)  
  
h_l=0.943*((g*rho_l*(rho_l-rho_v)*k^3*DELTAh_vap)/(mu*(T_sat-T_cond)*L))^(1/4)
```

The bottom window, titled "Solution", shows the following results:

Unit Settings: SI C kPa kJ mass deg

$\Delta h_{vap} = 2423$	$g = 9.81$	$h_l = 1560$	$k = 0.6029$	$L = 0.3$
$\mu = 0.0007977$	$P_{cond} = 5$	$\rho_l = 995.6$	$\rho_v = 0.02864$	$T_{cond} = 30$
$T_{sat} = 32.88$				

6 potential unit problems were detected.

Calculation time = .0 sec.

Figure 37: Condenser Load Calculations in EES

APPENDIX G

CONDENSER AREA CALCULATIONS

The condenser sizing analysis, discussed in Section 4.6, involved calculating an average heat transfer coefficient, a log mean temperature difference, and the required cooling load in order to define the condenser area. Once the heat transfer coefficient and the required cooling load were determined, several potential log mean temperature differences were compared for considering the required condenser area, though the condenser area was sized for the worst-case log mean temperature difference test scenario. The results for this comparison are included in Figure 38 below.

Q [W]	dT [K] (LMTD)	U [W/m ² -K]	A [m ²]
235.6	1	200	1.178
235.6	2	200	0.589
235.6	3	200	0.392667
235.6	4	200	0.2945
235.6	5	200	0.2356
235.6	6	200	0.196333
235.6	7	200	0.168286
235.6	8	200	0.14725

Figure 38: Condenser Areas for Various LMTDs

APPENDIX H

FLOW METER SPECIFICATIONS

Flow meters were used in both the vacuum system and the feed air system to quantify the air permeation and feed air flow rates, respectively. The specifications regarding the flow meters used in these various systems are included below.

Air Permeation Flow Meter Specifications

Omega Flo-Sensor
Sensor Type: Turbine Flow Meter
Model #: FLR1006-D
Serial Number: 2113
Maximum Allowable Error (calibration): $\pm 3\%$ F.S.
Calibrated Flow Range: 1L/min-5L/min

Feed Air Flow Meter Specifications

Omega Flo-Sensor
Sensor Type: Turbine Flow Meter
Model #: FLR1203
Serial Number: 8520
Maximum Allowable Error (calibration): $\pm 3\%$ F.S.
Calibrated Flow Range: 10 L/min-50 L/min

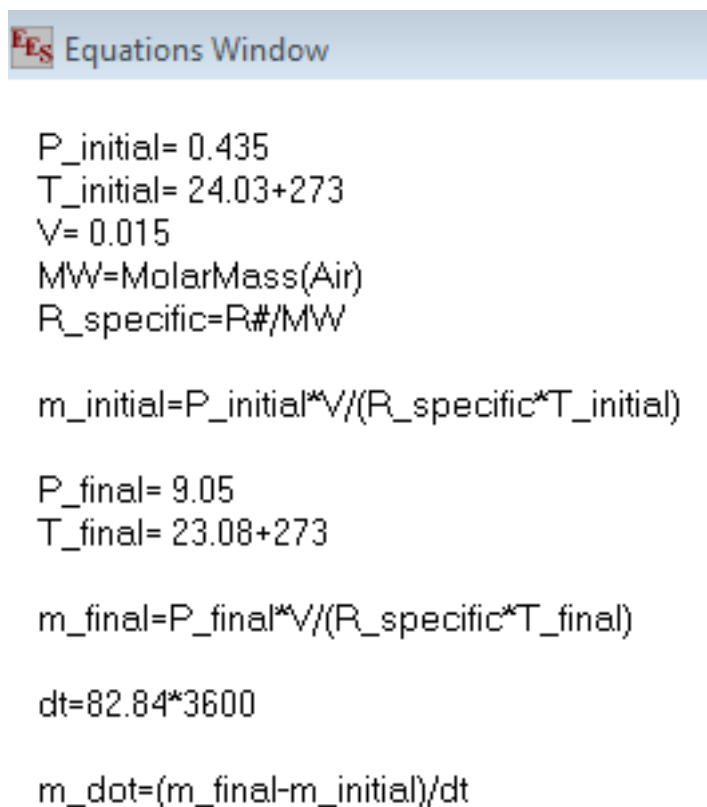
ARPA-E Test Condition Flow Meter Specifications

Omega Flo-Sensor
Sensor Type: Turbine Flow Meter
Model #: FLR1002
Serial Number: 8791
Maximum Allowable Error (calibration): $\pm 3\%$ F.S.
Calibrated Flow Range: 40mL/min-200mL/min

APPENDIX I

LEAKAGE UNCERTAINTY

The air leakage through the vacuum system was an important variable to quantify in order to ensure that the system leakage would have a negligible contribution to the vacuum pump exhaust air measurements. The data and calculations for the leak test process used to quantify the system leakage, explained in Section 4.11, are included in Figure 39.



```
EES Equations Window

P_initial= 0.435
T_initial= 24.03+273
V= 0.015
MW=MolarMass(Air)
R_specific=R#/MW

m_initial=P_initial*V/(R_specific*T_initial)

P_final= 9.05
T_final= 23.08+273

m_final=P_final*V/(R_specific*T_final)

dt=82.84*3600

m_dot=(m_final-m_initial)/dt
```

Figure 39: System Air Leakage Data and Calculations

The EES code uses the initial pressure (P_{initial}), the final pressure (P_{final}), the initial temperature (T_{initial}), the final temperature (T_{final}), the system volume (V), the

molar mass of air (MW), the specific gas constant (R_specific), and the elapsed time (dt) to calculate the initial system mass (m_initial), the final system mass (m_final), and the change in system mass over time (m_dot). This EES software is then able to calculate the partial derivatives of each variable and the percent contribution of each variable on the total uncertainty propagation, which is shown in Figure 40.

Unit Settings: SI C kPa kJ mass deg

Variable±Uncertainty	Partial derivative	% of uncertainty
$\dot{m} = 5.100\text{E-}09 \pm 3.415\text{E-}10$		
dt = 298224±0.001	$\partial \dot{m} / \partial dt = -1.710\text{E-}14$	0.00 %
MW = 28.97±0.0001	$\partial \dot{m} / \partial MW = 1.761\text{E-}10$	0.00 %
P_final = 9.05±0.04525	$\partial \dot{m} / \partial P_{\text{final}} = 5.919\text{E-}10$	0.61 %
P_initial = 0.435±0.002175	$\partial \dot{m} / \partial P_{\text{initial}} = -5.900\text{E-}10$	0.00 %
T_final = 296.1±1	$\partial \dot{m} / \partial T_{\text{final}} = -1.809\text{E-}11$	0.28 %
T_initial = 297±1	$\partial \dot{m} / \partial T_{\text{initial}} = 8.640\text{E-}13$	0.00 %
V = 0.015±0.001	$\partial \dot{m} / \partial V = 3.400\text{E-}07$	99.10 %

Figure 40: Air Leakage Uncertainty Propagation

APPENDIX J

TEST RESULTS

The water vapor permeance was plotted with respect to multiple variables, including the inlet humidity ratio, feed-air flow rate, permeate pressure, outlet temperature, inlet temperature, and temperature difference across the membrane module. The plots of the water vapor permeance with respect to all of the aforementioned variables are included in the figures below (Figure 41 through Figure 46).

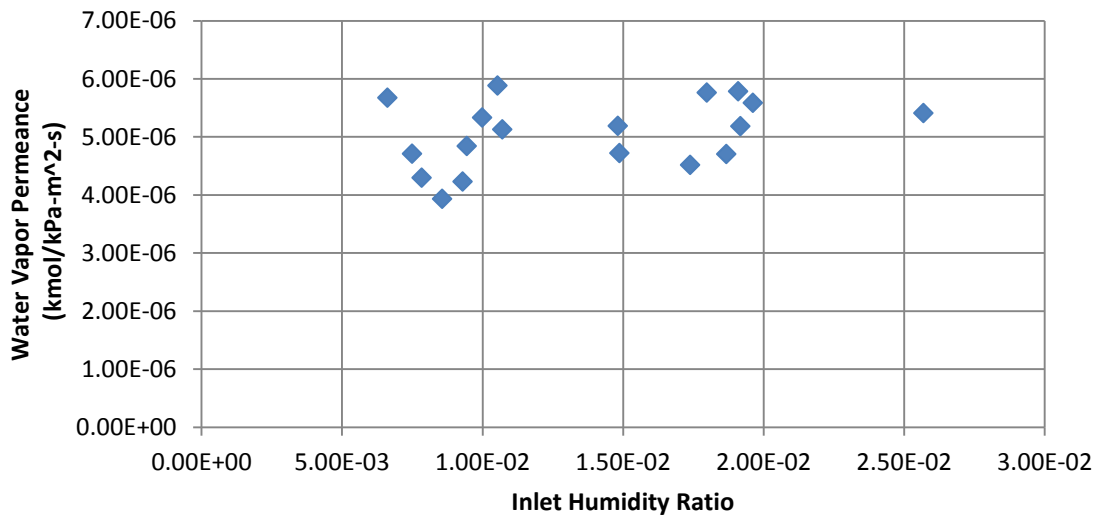


Figure 41: Water Vapor Permeance for Various Inlet Humidity Ratio

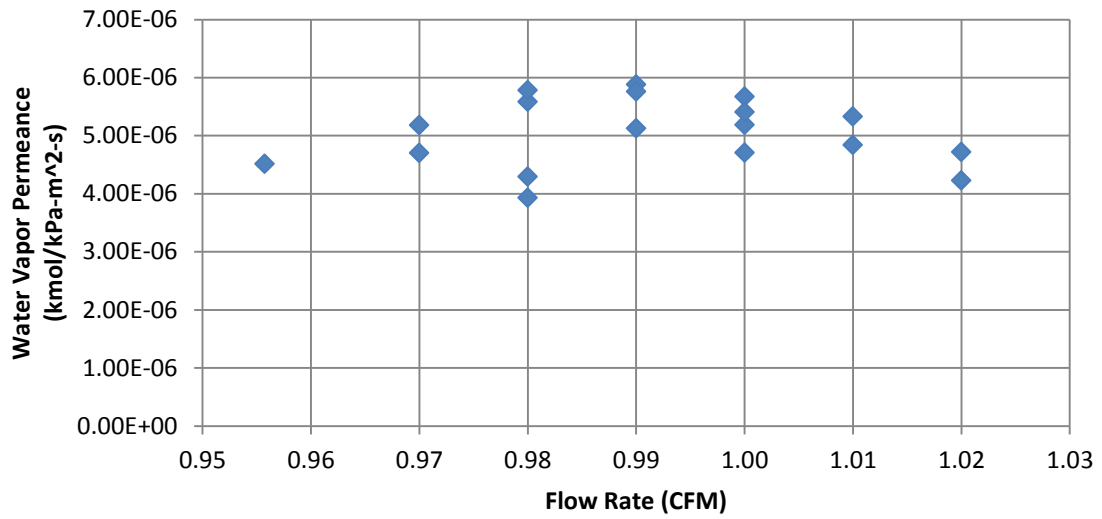


Figure 42: Water Vapor Permeance for Various Flow Rate

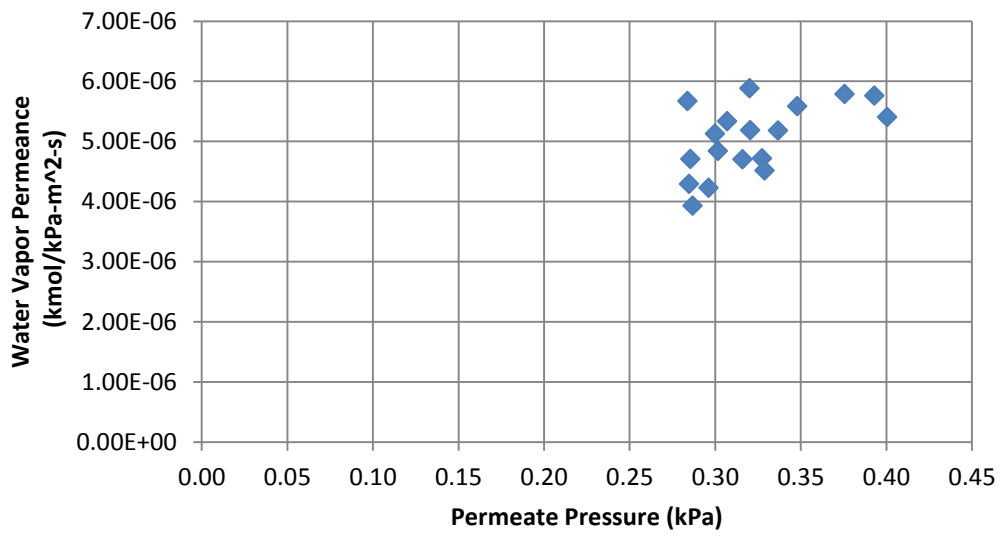


Figure 43: Water Vapor Permeance for Various Permeate Pressure

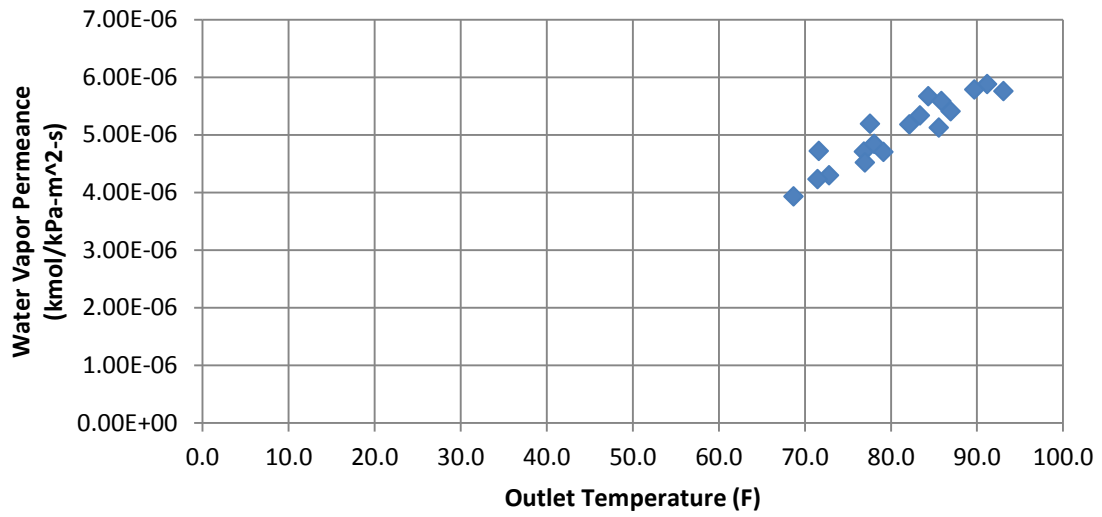


Figure 44: Water Vapor Permeance for Membrane Outlet Temperature

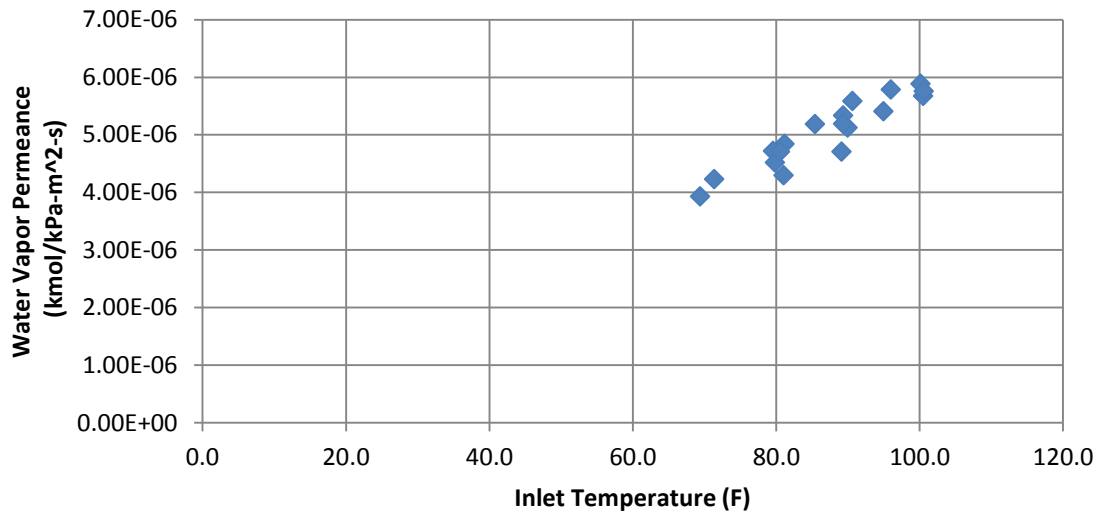


Figure 45: Water Vapor Permeance for Membrane Inlet Temperature

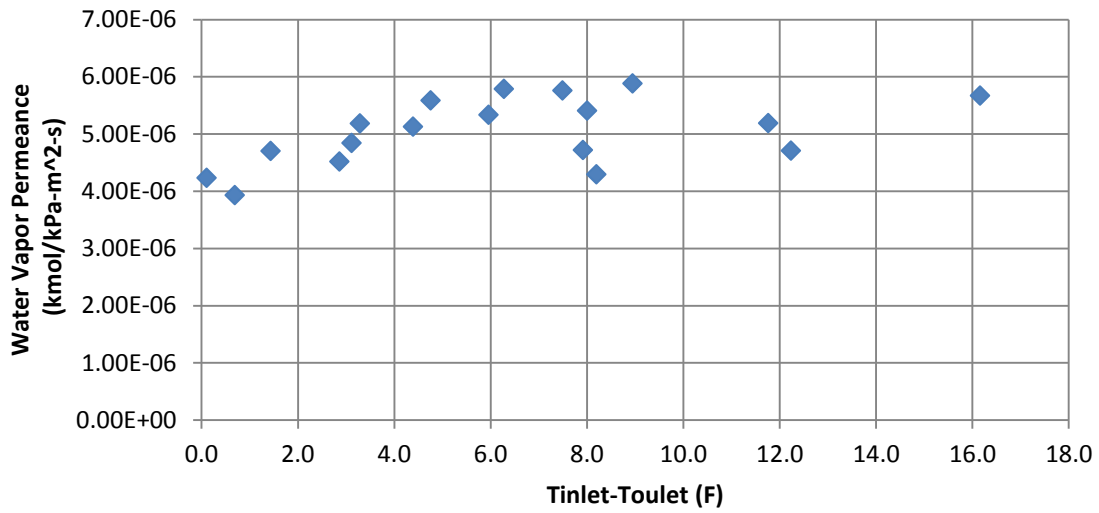


Figure 46: Temperature Gradients Effect on Water Vapor Permeance

Thermal gradients across the membrane module, indicated by the membrane module feed air inlet and outlet temperature measurements, were also observed. However, the dependence of these membrane module thermal gradients showed the strongest correlation to the temperature difference between the membrane inlet air and the room air; this relationship is shown in Figure 47.

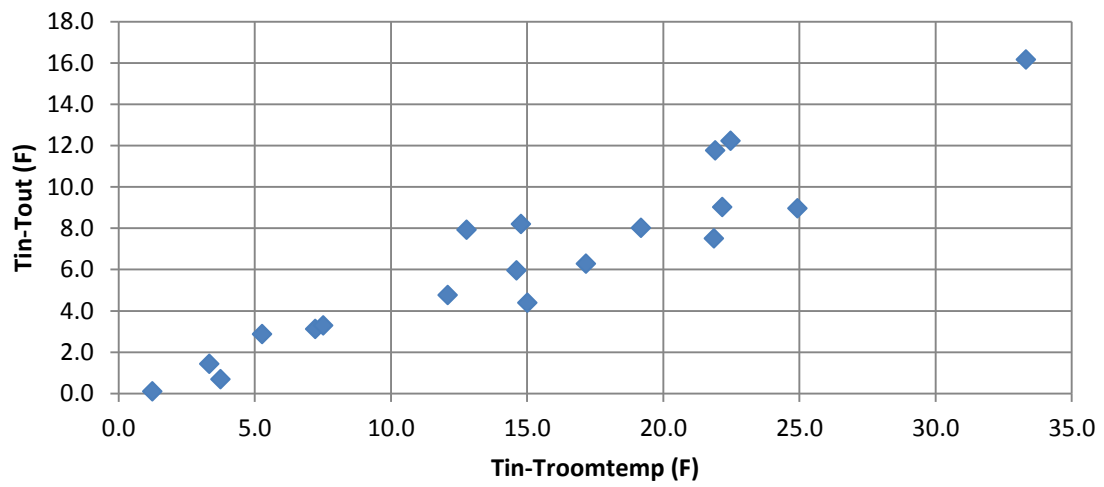


Figure 47: Feed Air Temperature Drop Dependence on Room Air

APPENDIX K

TABULATED RESULTS

The test data discussed in the membrane module evaluation section of Chapter 5 is included in Table 32.

Table 32: Measured Test Data Conditions

Room Temperature [F]	Membrane Inlet Temperature [F]	Membrane Outlet Temperature [F]	Feed Air Inlet [CFM]	Exhaust Air Flow [CFM]	RH _{in} %	Rh _{out} %	T _{dbin} [C]	T _{dbout} [C]	Permeate Pressure [kPa]	Room Temperature [C]
65.6	69.4	68.7	0.98	9.10E-04	56.24	41.43	20.72	19.83	0.35	18.69
66.3	81.0	72.8	0.98	9.09E-04	36.46	32.34	26.45	22.07	0.35	19.03
66.6	89.1	76.9	1.00	9.11E-04	27.51	26.73	30.56	24.18	0.35	19.24
67.2	100.5	84.4	1.00	9.11E-04	16.66	17.81	37.34	28.08	0.35	19.56
72.6	71.4	71.5	1.02	8.88E-04	58.54	39.40	21.37	21.60	0.35	22.57
74.0	81.2	78.1	1.01	8.83E-04	48.51	31.07	24.74	24.87	0.35	23.31
74.7	89.3	83.4	1.01	8.81E-04	34.21	26.46	31.70	27.74	0.35	23.74
74.9	90.0	85.6	0.99	8.88E-04	42.73	26.23	29.01	29.01	0.34	23.86
75.2	100.1	91.2	0.99	8.80E-04	23.66	20.74	39.34	31.90	0.36	24.00
66.8	79.6	71.6	1.02	8.98E-04	67.57	58.93	26.67	21.41	0.36	19.33
67.4	89.3	77.6	1.00	8.87E-04	50.17	46.22	31.76	24.45	0.35	19.69
77.2	80.6	79.1	0.97	8.85E-04	84.25	53.30	26.69	25.96	0.34	25.13
77.9	85.4	82.1	0.97	8.88E-04	71.29	47.45	30.01	27.60	0.36	25.51
78.5	90.6	85.9	0.98	8.79E-04	51.01	41.75	36.37	29.60	0.37	25.86
78.8	96.0	89.7	0.98	8.81E-04	33.89	36.68	43.55	31.24	0.40	26.01
78.7	100.6	93.1	0.99	8.67E-04	21.83	31.75	51.09	33.10	0.42	25.95
75.8	95.0	87.0	1.00	8.71E-04	65.24	57.75	36.63	28.98	0.42	24.32
76.8	99.0	90.0	1.01	8.67E-04	52.25	51.31	40.98	30.80	0.44	24.89

The temperature difference between the humidity sensor and RTD was due to the placement of the sensor. The humidity sensor was placed after the heater, but before the RTD. The humidity sensor was used to calculate the humidity ratio, but the RTD temperatures were used to determine the inlet and outlet temperature of the air as it entered and exited the membrane module, respectively.

Table 33 below indicates the membrane module performance parameter results that were calculated using EES.

Table 33: EES Calculated Results

Water Vapor Permeance [kmol/kPa-m ² -s]	Inlet Humidity Ratio	Outlet Humidity Ratio	Wet Bulb Temp. Inlet [C]	Wet Bulb Temp. Outlet [C]	Permeate Pressure [kPa]	Pin [kPa]	Pout [kPa]	Pressure Difference [kPa]	Air Permeation Rate [kmol/s]	Water Vapor Permeation Rate [kmol/s]
3.93E-06	8.57E-03	5.95E-03	15.3	12.4	0.29	1.38	0.96	0.86	1.79E-08	8.14E-08
4.29E-06	7.83E-03	5.32E-03	16.7	12.7	0.28	1.26	0.86	0.76	1.79E-08	7.80E-08
4.71E-06	7.50E-03	5.00E-03	17.8	13.2	0.29	1.21	0.81	0.70	1.79E-08	7.93E-08
5.67E-06	6.62E-03	4.19E-03	19.3	14.0	0.28	1.07	0.68	0.57	1.79E-08	7.69E-08
4.23E-06	9.29E-03	6.31E-03	16.1	13.5	0.30	1.49	1.02	0.94	1.73E-08	9.51E-08
4.84E-06	9.44E-03	6.06E-03	17.4	14.5	0.30	1.51	0.98	0.92	1.71E-08	1.07E-07
5.33E-06	9.99E-03	6.12E-03	20.1	15.6	0.31	1.60	0.99	0.95	1.71E-08	1.22E-07
5.13E-06	1.07E-02	6.53E-03	19.8	16.5	0.30	1.71	1.05	1.05	1.72E-08	1.29E-07
5.88E-06	1.05E-02	6.09E-03	22.8	17.1	0.32	1.69	0.98	0.97	1.70E-08	1.37E-07
4.72E-06	1.49E-02	9.38E-03	22.1	16.2	0.33	2.36	1.50	1.57	1.77E-08	1.77E-07
5.19E-06	1.48E-02	8.83E-03	23.5	16.8	0.32	2.36	1.42	1.52	1.74E-08	1.89E-07
4.70E-06	1.87E-02	1.12E-02	24.6	19.2	0.32	2.95	1.79	2.00	1.71E-08	2.25E-07
5.18E-06	1.92E-02	1.10E-02	25.7	19.6	0.34	3.03	1.75	1.99	1.71E-08	2.47E-07
5.58E-06	1.96E-02	1.08E-02	27.5	20.1	0.35	3.10	1.73	1.99	1.69E-08	2.66E-07
5.79E-06	1.91E-02	1.04E-02	28.8	20.3	0.38	3.02	1.67	1.89	1.69E-08	2.62E-07
5.76E-06	1.80E-02	1.00E-02	29.9	20.6	0.39	2.84	1.61	1.76	1.67E-08	2.43E-07
5.41E-06	2.57E-02	1.45E-02	30.6	22.5	0.40	4.02	2.31	2.67	1.68E-08	3.47E-07
5.75E-06	2.60E-02	1.43E-02	31.7	22.9	0.42	4.06	2.28	2.65	1.67E-08	3.66E-07

APPENDIX L

EES CALCULATION FILE AND UNCERTAINTY PROPAGATION

The results discussed in Chapter 5 involved calculating membrane performance parameters such as the separation factor and water vapor permeance. These parameters were calculated using EES, and the code used In EES is included in the text below.

```
"Required inputs: V_dot_feed, V_dot_vac, phi_in, phi_out, T_db_in, T_db_out,  
P_permeate_total, T_roomtemp"
```

```
P_b=101.25
```

```
rho_in=Density(Air_ha,T=T_roomtemp,P=P_b) "uses room temperature to determine  
density of the air going through the flow meters"
```

```
Amembrane=0.024 "m^2"
```

```
FeedAirMassFlowRate=V_dot_feed*0.0283168/60*rho_in*1000 "0.028.../60 converts  
ft^3 to m^3 and min to s & 1000 converts kg to g"
```

```
PermeatedAirMassFlowRate=V_dot_vac*0.0283168/60*rho_in*1000 "0.028.../60  
converts ft^3 to m^3 and min to s & 1000 converts kg to g"
```

```
Mwatervapor=MolarMass(Steam)
```

```
Mair=MolarMass(Air_ha)
```

```
Nratio=Mwatervapor/Mair
```


$P_{\text{satin}} = P_{\text{sat}}(\text{Steam}, T = T_{\text{db_in}})$ "determines saturation pressure of the inlet air"

$P_{\text{in}} = P_{\text{satin}} * \phi_{\text{in}} / 100$ "uses the saturation pressure and %RH to determine the partial pressure of water vapor at the inlet"

$T_{\text{wb_in}} = \text{WetBulb}(\text{AirH}_2\text{O}, T = T_{\text{db_in}}, r = \phi_{\text{in}} / 100, P = 101.25)$ "determines the wet bulb temperature at given dry bulb and %RH conditions"

$\omega_{\text{in}} = P_{\text{in}} * N_{\text{ratio}} / (P_{\text{b}} - P_{\text{in}})$ "uses ideal gas law to determine the ratio of mass using the molar ratio"

$P_{\text{satout}} = P_{\text{sat}}(\text{Steam}, T = T_{\text{db_out}})$

$P_{\text{out}} = P_{\text{satout}} * \phi_{\text{out}} / 100$

$T_{\text{wb_out}} = \text{WetBulb}(\text{AirH}_2\text{O}, T = T_{\text{db_out}}, r = \phi_{\text{out}} / 100, P = 101.25)$

$\omega_{\text{out}} = P_{\text{out}} * N_{\text{ratio}} / (P_{\text{b}} - P_{\text{out}})$

$M_{\text{waterpermeationrate}} = \text{FeedAirMassFlowRate} * \omega_{\text{in}} - (\text{FeedAirMassFlowRate} - \text{PermeatedAirMassFlowRate}) * \omega_{\text{out}}$ "g/s"

"FeedAirMassFlowRate - PermeatedAirMassFlowRate accounts for the loss of air through the membrane"

$M_{\text{dot_permeation_wv}} = M_{\text{waterpermeationrate}} / (1000 * M_{\text{watervapor}})$ "kmol/s"

$M_{\text{dot_permeation_air}} = \text{PermeatedAirMassFlowRate} / (1000 * M_{\text{air}})$ "kmol/s"

$P_{\text{permeate_wv}} = P_{\text{permeate_total}} * M_{\text{dot_permeation_wv}} / (M_{\text{dot_permeation_wv}} + M_{\text{dot_permeation_air}})$ "uses ideal gas law to determine partial pressure"

$P_{\text{permeate_air}} = P_{\text{permeate_total}} * M_{\text{dot_permeation_air}} / (M_{\text{dot_permeation_wv}} + M_{\text{dot_permeation_air}})$ "uses ideal gas law to determine partial pressure"

$LMPD = (P_{\text{in}} - P_{\text{out}}) / \ln(\text{abs}(P_{\text{in}} - P_{\text{permeate_wv}}) / \text{abs}(P_{\text{out}} - P_{\text{permeate_wv}}))$

$\text{Permeance_wv} = M_{\text{dot_permeation_wv}} / (LMPD * A_{\text{membrane}})$

APPENDIX M

POWER MEASUREMENT

Section 5.3 discussed the power consumption of various system components. The power consumption measurement outputs for the three-phase equipment included the individual line loads and power factors, which were useful for isolating the real power from the apparent power. The power consumption breakdown for both the Fuji compressor and the intermediate compressor are included in Table 34 and Table 35 below.

Table 34: Fuji Compressor (Fan) Power Consumption Details

	FAN						
	Vrms	Vpeak	Arms	Apeak	W	VA	PF
L1	122.2	172.1	0.59	2.66	17	71	0.25
L2	122.7	172.3	0.94	3.96	40	124	0.33
L3	214	306	0.98	3.72	100	230	0.43

Table 35: Intermediate Compressor Power Consumption Details

	INTERMEDIATE COMPRESSOR				
	Vrms	Arms	W	VA	PF
L1	144.9	3.86	308	559	0.56
L2	143.3	3.46	277	498	0.55
L3	137.3	3.64	282	502	0.56